ABSTRACT

Title of dissertation: BACK-ACTION EVADING
MEASUREMENTS OF
NANOMECHANICAL MOTION
APPROACHING QUANTUM LIMITS

Jared B. Hertzberg
Doctor of Philosophy, 2009

Dissertation committee chair: Professor Christopher Monroe

The application of quantum mechanics to macroscopic motion suggests many counterintuitive phenomena. While the quantum nature of the motion of individual atoms and molecules has long been successfully studied, an equivalent demonstration of the motion of a near-macroscopic structure remains a challenge in experimental physics. A nanomechanical resonator is an excellent system for such a study. It typically contains $> 10^{10}$ atoms, and it may be modeled in terms of macroscopic parameters such as bulk density and elasticity. Yet it behaves like a simple harmonic oscillator, with mass low enough and resonant frequency high enough for its quantum zero-point motion and single energy quanta to be experimentally accessible.

In pursuit of quantum phenomena in a mechanical oscillator, two important goals are to prepare the oscillator in its quantum ground state, and to measure its position with a precision limited by the Heisenberg uncertainty principle $\Delta x \Delta p \geq \frac{\hbar}{2}$. In this work we have demonstrated techniques that advance towards both of these

goals. Our system comprises a 30 micron × 170 nm, 2.2 pg, 5.57 MHz nanomechanical resonator capacitively coupled to a 5 GHz superconducting microwave resonator. The microwave resonator and nanomechanical resonator are fabricated together onto a single silicon chip and measured in a dilution refrigerator at temperatures below 150 mK. At these temperatures the coupling of the motion to the thermal environment is very small, resulting in a very high mechanical Q, approaching $\sim 10^6$.

By driving with a microwave pump signal, we observed sidebands generated by the mechanical motion and used these to measure the thermal motion of the resonator. Applying a pump tone red-detuned from the microwave resonance, we used the microwave field to damp the mechanical resonator, extracting energy and "cooling" the motion in a manner similar to optical cooling of trapped atoms. Starting from a mode temperature of $\sim$150 mK, we reached $\sim$40 mK by this "backaction cooling" technique, corresponding to an occupation factor only $\sim$ 150 times above the ground state of motion.

We also determined the precision of our device in measurement of position. Quantum mechanics dictates that, in a continuous position measurement, the precision may be no better than the zero-point motion of the resonator. Increasing the coupling of the resonator to detector will eventually result in back-action driving of the motion, adding imprecision and enforcing this limit. We demonstrated that our system is capable of precisions approaching this limit, and identified the primary experimental factors preventing us from reaching it: noise added to the measurement by our amplifier, and excess dissipation appearing in our microwave resonator at high pump powers.

Furthermore, by applying both red- and blue-detuned phase-coherent microwave pump signals, we demonstrated back-action evading (BAE) measurement sensitive to only a single quadrature of the motion. By avoiding the back-action driving in the measured quadrature, such a technique has the potential for precisions surpassing the limit of the zero-point motion. With this method, we achieved a measurement precision of $\sim$100 fm, or 4 times the quantum zero-point motion of the mechanical resonator. We found that the measured quadrature is insensitive to back-action driving by at least a factor of 82 relative to the unmeasured quadrature. We also identified a mechanical parametric amplification effect which arises during the BAE measurement. This effect sets limits on the BAE performance but also mechanically preamplifies the motion, resulting in a position resolution 1.3 times the zero-point motion.

We discuss how to overcome the experimental limits set by amplifier noise, pump power and parametric amplification. These results serve to define the path forward for demonstrating truly quantum-limited measurement and non-classical states of motion in a nearly-macroscopic object.

BACK-ACTION EVADING MEASUREMENTS OF NANOMECHANICAL MOTION APPROACHING QUANTUM LIMITS

by

Jared Barney Hertzberg

Dissertation submitted to the Faculty of the Graduate School of the
University of Maryland, College Park in partial fulfillment
of the requirements for the degree of
Doctor of Philosophy
2009

Advisory Committee:
Professor Christopher Monroe, Chair
Professor Keith C. Schwab (California Institute of Technology), Advisor
Professor Richard L. Greene
Professor Luis A. Orozco
Professor John Melngailis, Dean's Representative

© Copyright by
Jared B. Hertzberg
2009

Dedication

To my parents, Fran and George Hertzberg, who have always encouraged me in my education, and who did everything they could to give me the best opportunities.

To my late great-uncle Sam Ballen, friend and admirer of physicists.

Acknowledgments

I have received funding during my Ph.D. from the Laboratory for Physical Sciences (2003-07), and from FQXi (2007-09). The work appearing in this dissertation was accomplished mostly in the the last two years, but was the culmination of many more years of effort, and reflects the aid and encouragement of many people.

I must thank the members of my examining committee: Prof. Christopher Monroe, Prof. Keith Schwab, Prof. Richard Greene, Prof. Luis Orozco and Prof. John Melngailis. I'm especially grateful to Prof. Monroe as chair of the committee for helping me to resolve some administrative issues at the last minute.

The administration and staff of the UMD Physics department have been very helpful to me over the years, especially during the past two years when I left College Park to continue my research work at Cornell. The department very graciously arranged to cover my tuition and waive my student fees during this time. Prof. Greg Sullivan and Prof. Nick Chant deserve my thanks in this, and Jane Hessing has been a tireless help. Without her I could never have navigated the un-ending paperwork.

I must also thank the UMD physics department for their support and advocacy in 2005-07 when the nanomechanics group faced difficulties imposed by LPS management. Prof. Drew Baden and Prof. Jordan Goodman, in addition to Prof. Sullivan and Prof. Chant, were a great help.

In my time at Cornell I have had the great fortune to work closely with two talented graduate students, Tristan Rocheleau and Tchefor Ndukum. By the time

I arrived here in summer 2007, they had already put in nearly a year of hard effort making the lab ready for measurements. I have learned a great deal from both of them, and enjoyed it, too. I feel like this work is as much theirs as it is mine. Tristan did much of the lab setup and wiring, all of the LabView programming, and many of the measurements. His creativity, curiousity and positive spirit were invaluable to this work. Tchefor did much of the lab setup, most of the clean room fabrication, and many measurements and calculations. His thoroughness, determination and careful reading of the literature make him a formidable researcher. I feel that both Tristan and Tchefor are destined for great careers in science.

Many other members of the Schwab group at Cornell have helped with the experiment in practical ways, and just by their presence made my time here enjoyable: Chris Macklin, Peter Hauck, Madeleine Corbert, Sara Brin Rothenthal, Adil Gangat, Peter Swift, Darren Southworth and Dr. Matt Shaw. Manolis Savva's design and assembly of the microwave filter cavities was essential to our results.

I should thank many others at Cornell. I shared many enjoyable conversations with my fellow denizens of "H corridor," Dr. Andrew Fefferman, Dr. Kiran Thadani, Sufei Shi and Dr. Ethan Bernard. Our group did all of our micro- and nanofabrication at the NSF-sponsored Cornell Nanoscale Facility, where I am grateful to Dr. Rob Ilic and Meredith Metzler for invaluable fabrication advice. Our group borrowed key pieces of equipment from the CCMR facilities. Stan Carpenter, Jeff Koski, Chris Cowulich, Nate Ellis and others at the Cornell physics shop made critical components of high precision and quality. Dr. Eric Smith has dispensed helium along with his encyclopedic knowledge of low-temperature systems and techniques.

If you ask his advice, he'll never simply tell you to "read my book."

I am indebted to several people beyond Cornell for enlarging my understanding of quantum phenomena in mechanical motion. Prof. Miles Blencowe and Prof. Roberto Onofrio looked over our draft paper and offered valuable suggestions. Prof. Blencowe also generously read and offered comments on a partial draft of this dissertation. In writing our paper, Prof. Aashish Clerk was patient with my questions and tireless in his careful reading and analysis of our many manuscripts. Several of his unpublished theoretical calculations are incorporated into this dissertation. I also had many valuable discussions with Dr. John Lawall. Prof. Britton Plourde generously contributed his resources to our early fabrication efforts. I must also thank Dr. Markus Aspelmeyer and his group at the IQOQI in Vienna, Dr. Sylvain Gigan, Dr. Hannes Böhm, and Simon Gröblacher, for welcoming me into their group as a collaborator. I learned much from their quantum optics perspective on their work, which is so similar in concept to ours, and enjoyed immensely my time working with them fabricating optomechanical devices.

From our four years together at LPS, and many meetings and conversations afterward, I am indebted to the "old guard" of the Schwab group, now scattered to the four corners of the globe but still together in spirit: Emrah Altunkaya, Dr. Harish Bhaskaran, Dr. Benedetta Camarota, Dr. Akshay Naik, Dr. Matt LaHaye, Dr. Alex Hutchinson, Dr. Olivier Buu and Dr. Patrick Truitt. Benedetta taught me nanofabrication, Akshay taught me how to run a dilution fridge, and Patrick and Emrah shared many long nights in the lab with me. Benedetta also read parts of this dissertation in draft form and suggested helpful corrections.

Many LPS and UMD staff made my time at LPS more enjoyable and productive: Les Lorenz, J.B. Dotellis, Dr. Ben Palmer, Dr. Barry Barker, Mike Khbeis, Dr. Bruce Kane, Russell Frizzell, Toby Olver, Butch Bilger and Prof. Bob Anderson. The student and postdoc cohort, Dr. Kevin Eng, Dr. Dan Sullivan, Dr. Luyan Sun, Dr. Hui Wang, Dr. Jonghee Lee, Dr. Kenton Brown and Robert McFarland were all sources of valuable conversation and advice whether over lunch or in the clean room.

Through six years of grad school, I have relied on many old friends to keep up good cheer and diversion from my studies: Cristy Maldonado, Dr. Rudy Magyar, Mariana Osorio, Juan Burwell, Lisa Winter, Angi Arya, Dr. Kani Ilangovan, Cliff Lardin and Heather Miller Lardin, Dr. Jeremy Perlman, Umaa Rebbapragada, Jessica Schattschneider and Ryan Senser, some of whom are still slogging through their own graduate work. I should also thank the friends I made at UMD, including Bijan Afsari, Dr. Doug Kelley and Andrew Tunnell. Thanks to Eran Goudes and Gwen's friends on U Street for letting me stay at their home when I did my defense.

I must thank Prof. Larry Hunter and the Amherst College physics department for the inspiration, encouragement, and early training in physics that led me to this point.

To my family, especially my parents, George and Fran Hertzberg, I owe a debt I can never fully repay, not only for my earlier education that paved the way for my graduate work, but also for their support, patience, advice, encouragement, and a ready ear to listen to me during the past six years. My grandmother, Judy Levine, has given her quiet strong support. My late grandfathers, Irving Harelick and Milton Levine, were always keenly interested in how I was coming along with my Ph.D., and insistent that I do my very best academically. I wish they could be here to see it completed.

These acknowledgements would be incomplete without a word about my advisor, Prof. Keith Schwab. It has been a privilege to work for and with Keith these past six years. I have learned that in experimental physics the most precious commodity is not money or supplies or equipment but *good ideas*, good not just in their novelty but in their ability to be practically realized, and for the level of interest they will generate in the scientific community. The work in this dissertation is the fruit of Keith's good ideas. I am indebted to Keith for his leadership, for his advice and guidance, for his willingness to introduce me to other key researchers, for providing ample resources, and for his friendship. In the past half-dozen years I have watched quantum nanomechanics emerge as a growing sub-field of physics, largely due to his vision and efforts.

Lastly, I must thank my dear partner Gwen Glazer, for her patience and love as this Ph.D. grew inevitably in its final stages into my singular obsession. She has been unflappable, offering me limitless support, good cheer, patience, keen instincts, a willingness to listen to me at any time, and on many occasions even feeding me or bringing me coffee in the morning. If this document is relatively free of bad wording, misspellings and bad grammar, thank Gwen and her professional editor's eye. I am glad to share my life with her.

Table of Contents

List of Tables

List of Figures

List of Abbreviations and Symbols

SMR	Superconducting Microwave Resonator
NR	Nanomechanical Resonator
CPW	Coplanar waveguide
SiN	Silicon nitride

C	Effective capacitance of SMR
C_κ	Capacitance coupling each end of SMR to external circuitry
C_g	"Gate" capacitance coupling SMR to NR
Γ_{NR}	Linewidth of NR due to coupling to thermal bath
Γ_{opt}	Additional dissipation of NR due to coupling to microwave field
Γ_{tot}	Total measured NR linewidth
	(Note, all symbols ω, κ and Γ are in units of angular frequency.)
$gain$	Total gain of apparatus from SMR to measurement point
$\hbar$	Reduced Planck constant
κ_{int}	Linewidth of SMR due to internal dissipation
κ_{ext}	Linewidth of SMR due to coupling to external circuitry
κ	Total linewidth of SMR ($\kappa = \kappa_{ext} + \kappa_{int}$)
k	Spring constant of NR
k_B	Boltzmann's constant

$loss$	Loss in signal lines from apparatus input to SMR
m	Effective mass of NR
$\bar{n}_{SMR}$	Occupation of pump photons in SMR
$\bar{n}_{SMR}^{T}$	Thermal occupation of SMR
$\bar{n}_{NR}^{T}$	Thermal occupation of NR when coupled only to thermal bath
$\bar{n}_{NR}^{opt}$	Effective occupation of energy bath formed by microwave field
$\bar{n}_{NR}^{eff}$	Apparent occupation of NR as directly measured
$\bar{n}_{NR}$	Equilibrium occupation of NR
ω_{SMR}	Resonant frequency of SMR
ω_{NR}	Resonant frequency of SMR
$\Delta\omega$	Difference of frequency from ω_{SMR}
P_{in}	Input pump power to apparatus
P_{out}	Output pump power transmitted by apparatus
P_{sideb}	Power of sideband signal generated by NR motion
S_x	Position noise spectral density
R_L	Load resistance of external circuitry (typically 50 ohms)
T_{NR}	Mode temperature of NR motion
T	Fridge or “thermal bath” temperature

X_1	Quadrature of NR motion detected by BAE measurement
X_2	Quadrature of NR motion perturbed by BAE measurement
x	Instantaneous amplitude of mechanical motion
$\langle x^2 \rangle$	Mean-squared amplitude of mechanical motion
Δx	Position uncertainty
Δx_{ZP}	Zero-point motion
Z_0'	Characteristic impedance of transmission line
Z_0	Characteristic impedance lumped-element SMR model

Chapter 1

Introduction

Quantum mechanics is a remarkably successful set of physical theories. In principle there should be no limits on the size or scale of systems or their parameters to which it may apply. There is no fundamental reason why the behavior of everyday objects, for instance the motion of a baseball or the vibrations of a bridge, should not be describable in terms of quantum mechanics. Yet until very recently, experimental demonstration of physical systems that are described entirely in terms of quantum mechanics was confined to the atomic scale.

The development of such systems as Bose-Einstein condensates and superconducting qubits has brought the first opportunities to truly engineer devices in which quantum-mechanical behavior of some variable is coherent across the entirety of a macroscopic or near-macroscopic structure. In solid-state systems, it is appealing to move beyond electrical degrees of freedom such as voltage or charge and try to apply quantum mechanics to the center-of-mass position of a large mechanical structure. While the quantum nature of the motion of individual atoms and molecules has been successfully shown over macroscopic distances, the equivalent for the motion of an actual macroscopic structure has not. In pursuit of such a demonstration, an excellent system to work with is a harmonic oscillator. The quantum harmonic oscillator is a textbook case in every introductory quantum-mechanics class, and real mechanical harmonic oscillators are easy to make in the laboratory at a wide range of sizes and mass scales. The goal then is to take a real mechanical harmonic oscillator and make it behave quantum-mechanically. Most promising is to work with mechanical resonators on the micron scale, which typically contain $> 10^{10}$ atoms and which are usually described entirely in terms of macroscopic parameters such as bulk density and elasticity, but which are yet small and light enough to seem promising for quantum-mechanical experiments.

Quantum mechanics describes a wide number of non-classical behaviors that are inherently counterintuitive when applied to macroscopic scales. The possibilities of manifesting these in the motion of a large structure are intriguing: for instance, a superposition state of position states would place our mechanical oscillator simultaneously in two different locations. Micro- and nanomechanical resonators are the focus of a number of proposals to create macroscopic Schrödinger's-cat states, and use them to perform fundamental tests of quantum mechanics and the nature of decoherence. [1]

There is increasing interest by many researchers in demonstrating quantum-limited measurement of mechanical motion [2]. Heisenberg's uncertainty principle dictates limits for the precision of measurement of mechanical motion, which have yet to be reached. In practice, the limits on measurement are readily conceived of in terms of noise, either noise added to the measurement or noise that drives the mechanical resonator. The latter is how the uncertainty principle is "enforced": when the measurement is made more strongly, i.e. with closer and closer precision, the measurement will begin to perturb the motion, degrading the precision of subsequent measurements. Here we come upon the concept of "measurement backaction". In general this term has a very broad meaning, and can refer to any kind of effect that the measurement has on the device being measured. By making the measurement in different ways, the backaction can be made to damp the motion or to drive it to higher amplitudes. The most interesting and relevant type of backaction, however, is quantum backaction, in which the shot noise of the electromagnetic field that is used to make the measurement has the effect of perturbing the motion. It is shot noise that ultimately enforces the uncertainty principle. Shot-noise backaction on mechanical motion has been demonstrated in a few instances, but full exploration of this behavior remains elusive. [3]

The experimental study of these issues is nowadays a very rapidly-expanding field, as manifested by the rising number of publications and active research groups. All researchers in this field share a common set of goals: to put a mechanical resonator into its quantum ground state, to demonstrate quantum limited position detection, and to generate non-classical states of motion such as "squeezed states." The results presented in this dissertation represent a contribution towards these goals. The work is as much the product of a whole research group as it is my own. Building on earlier investigations by our group [4] [3], it represents a new type of experiment and promising new type of measurement device - the measurement of the motion of a nanomechanical resonator by exploiting its coupling to a superconducting microwave resonator. While I did not in this work attain any of the goals of quantum measurement, I thoroughly investigate this device, explore a wide range measurement techniques, identify the experimental challenges and present a path forward to reaching all of the key goals in the field. In particular, I address the prospect of using our new type of device to perform backaction-evading and quantum-nondemolition measurements of the motion, which in certain circumstances can surpass quantum limits on position measurement. While all my results are in the classical realm, I will describe them interchangeably in quantum-mechanical terms as much as possible.

I expect the work presented in this dissertation to be merely the start of a series of experiments carried on by the members of the research group. This dissertation was designed to serve as baseline and reference for those further investigations. The material is presented as follows: In chapter 2 I describe a model of our device based on simple electrical circuit theory, and derive analytical expressions for the signal amplitude representing the motion of the nanomechanical resonator. In chapter 3 I survey the ways in which measurement backaction can be made to perturb the motion of the mechanical resonator, and review some of the theory and experimental work performed by others in this field. In chapter 4 I describe our measurement apparatus and device fabrication. Chapter 5 describes the ways in which we characterize our device and our apparatus to enable us to properly understand the more critical measurements. Chapter 6 details those measurements, in which we explored the various effects described in chapter 3. Chapter 7 offers some brief concluding remarks.

Chapter 2

Superconducting Microwave Resonator (SMR) Coupled to Nanomechanical Resonator (NR)

In this chapter we intoduce the system that we will use to study mechanical motion near the quantum limit, consisting of a superconducting microwave resonator (SMR) coupled capacitively to a nanomechanical resonator (NR). We present a simple lumped-element LRC circuit model for the SMR and use this to describe the voltages, currents, power and stored energy in the SMR for a given input signal. By modeling the NR as an additional capacitance whose value changes with position, we derive analytical expressions for signal levels measured in this work.

2.1 Transmission line resonator

Microwave resonators made of microfabricated superconducting transmission line have been adopted widely in recent years for sensitive detection and measurement applications. [5] By exploiting their similarity in principle to optical cavities, researchers have adapted techniques developed in atomic physics and quantum optics to the study of nano-fabricated electrical devices. [6] [7]

2.1.1 Transmission line

We base our analysis of the SMR on the well-known solutions for voltages and currents flowing in a transmission line, often referred to as "transmission line theory" and appearing in many textbooks [8] [9] [10]. Here we summarize the relevant points:

Consider a transmission line consisting of a centerline and ground line or groundplane, having capacitance C' per unit length between centerline and ground, and inductance L' per unit length along the centerline. The phase velocity of waves traveling on the transmission line is $v_{ph} = \frac{1}{\sqrt{L'C'}}$ and the *characteristic impedance* of the transmission line is defined as

$$Z_0' = \sqrt{\frac{L'}{C'}} \tag{2.1}$$

The transmission line may also include some ohmic loss represented by a resistance R' per unit length. R' may be thought of as a combination of a resistance R'_{series} in series with the inductance and a shunt conductance G'_{shunt} in parallel with the capacitance: $R' = R'_{series} + G'_{shunt}(Z_0')^2$. Using Kirchoff's equations, with the impedances per unit length in the transmission line, we can solve for the voltages and currents on the line. We find that at frequency ω, the transmission line supports waves traveling in the $+x$ direction ($V^+(x)$ and $I^+(x)$) along with those traveling in the $-x$ direction ($V^-(x)$ and $I^-(x)$):

$$V^{\pm}(x) = V_0^{\pm} e^{i\omega t \mp ix(\omega/v_{ph}) \mp (R'/2Z_0')x} \tag{2.2}$$

$$I^{\pm}(x) = \pm \frac{V_0^{\pm}}{Z_0'} e^{i\omega t \mp ix(\omega/v_{ph}) \mp (R'/2Z_0')x} \tag{2.3}$$

Here we assume that the wavelength is short enough that reactive voltage drops dominate over ohmic ones: $R' \ll \omega Z_0'/v_{ph}$ ("low loss" cable approximation). The time-averaged power traveling down the cable may be calculated using $P(x) = \mathrm{Re}(V(x)I^*(x))$, where by convention power flowing in the + direction has positive sign and power flowing in the − direction has negative sign.

If the transmission line is *terminated* with a (possibly complex) impedance Z_L connecting centerline to ground at position $x = 0$, this sets a boundary condition $Z_L = \frac{V^+(0)+V^-(0)}{I^+(0)+I^-(0)}$, which we may use to solve for the amplitudes $V_0^{\pm}$ of the waves propagating in each direction. For a transmission line that extends in the − direction from $x = 0$, the − traveling wave $V^-(x)$ will be a partial or total *reflection* of the incoming + traveling wave, $V^+(x)$: $V_0^- = \Gamma V_0^+$ (where both V_0^- and V_0^+ are referenced to $x = 0$, the reflection point). The *reflection coefficient* is $\Gamma = \frac{Z_L - Z_0'}{Z_L + Z_0'}$. The voltage and current at point x (where in this geometry $x < 0$) are then

$$V(x) = V_0^+ e^{i\omega t}(e^{-ix(\omega/v_{ph})-(R'/2Z_0')x} + \Gamma e^{ix(\omega/v_{ph})+(R'/2Z_0')x}) \tag{2.4}$$

$$I(x) = \frac{V_0^+}{Z_0'} e^{i\omega t}(e^{-ix(\omega/v_{ph})-(R'/2Z_0')x} - \Gamma e^{ix(\omega/v_{ph})+(R'/2Z_0')x}) \tag{2.5}$$

Due to ohmic loss in the line, the forward-traveling power $P^+(x)$ diminishes as it approaches the load, while the negative-traveling power $P^-(x)$ diminishes as it recedes from the reflection point. These are found to be

$$P^+(x) = \frac{|V_0^+|^2}{2Z_0'} e^{-(R'/2Z_0')x} \tag{2.6}$$

$$P^-(x) = -|\Gamma|^2 \frac{|V_0^+|^2}{2Z_0'} e^{(R'/2Z_0')x} \tag{2.7}$$

We can also define the *input impedance* $Z_{in}(x)$ at point x, i.e. the terminated length of transmission line, of length $|x|$, treated as a single load impedance:

$$Z_{in}(x) = Z_0' \frac{Z_L + Z_0' \tanh\left(i\frac{\omega}{v_{ph}}|x| + \frac{R'}{2Z_0'}|x|\right)}{Z_0' + Z_L \tanh\left(i\frac{\omega}{v_{ph}}|x| + \frac{R'}{2Z_0'}|x|\right)} \tag{2.8}$$

2.1.2 Circuit model of transmission line resonator

From equations (2.4) and (2.5) it is evident that the fields on the terminated transmission line are a combination of traveling waves and standing waves of wavelength $\lambda = 2\pi v_{ph}/\omega$, and that for particular terminations (e.g. $\Gamma = \pm 1$) only standing waves will result. Then if terminated properly at two ends, a transmission line of length l becomes a resonant cavity with resonant frequency defined by the boundary conditions: A short ($Z_L = 0$) at one end and open ($Z_L \sim \infty$) at the other becomes resonant for $l = \frac{\lambda}{4} + n\frac{\lambda}{2}$, i.e. $\omega = \frac{\pi v_{ph}}{l}(n + \frac{1}{2})$, with $n = 0, 1, 2, \ldots$ ("quarter wave" resonator and harmonics). An open termination at both ends becomes resonant for $l = n\frac{\lambda}{2}$, i.e. $\omega = n\frac{\pi v_{ph}}{l}$, with $n = 1, 2, \ldots$ ("half wave" resonator and harmonics). Of course, the open ends are not completely isolated; some energy leaks in and out, which is how the cavity is energized and probed. Consider a resonator with open terminations at both ends, with microwave power applied at one end. We can think about the resonance this way: The field inside is in phase with the field entering at the "input end". Inside the cavity, the microwaves circulate, i.e. bounce back and forth between the two ends, forming a standing wave. In a single round-trip, the microwaves lose an amount of power due to ohmic losses and the power emitted at the opposite end of the cavity. From equations (2.6) and (2.7), we can see that this should be a fraction $1 - |\Gamma|^2 e^{-(R'/Z_0')l}$ of the power circulating within the cavity. In steady state, the power injected at the “input end” must balance the amount lost in the round-trip.

In our experiments, we will refer to the half-wave transmission-line resonator of length l as the “superconducting microwave resonator” (SMR). For frequencies around a resonant frequency $\omega_{SMR} = n\frac{\pi v_{ph}}{l}$ it is convenient to model the SMR as an equivalent LRC circuit. We start by setting $Z_L = \infty$ in equation (2.8), leaving $Z_{in} = \frac{Z_0'}{\tanh(i\omega l/v_{ph}+R'l/2Z_0')}$. We then substitute $\omega = \omega_{SMR} + \Delta\omega$ and perform a taylor expansion on the denominator:

$$Z_{in} = \frac{Z_0'}{\tanh(in\pi + i\Delta\omega l/v_{ph} + R'l/2Z_0')} \tag{2.9}$$

$$\simeq \frac{Z_0'}{i\Delta\omega l/v_{ph} + R'l/2Z_0'} \tag{2.10}$$

For a parallel LRC circuit (figure 2.2 b), the total impedance Z is found from $\frac{1}{Z} = \frac{1}{R} + \frac{1}{i\omega L} + i\omega C$. Considering frequencies $\omega = \omega_0 + \Delta\omega$ around resonant frequency $\omega_0 = \frac{1}{\sqrt{LC}}$ (assuming $\frac{\Delta\omega}{\omega_0} \ll 1$ and employing $Z_0 = \sqrt{L/C}$) we have

$$Z = \frac{iRZ_0(1+\Delta\omega/\omega_0)}{R + iZ_0(1+\Delta\omega/\omega_0) - R(1+\Delta\omega/\omega_0)^2}$$

Dividing numerator and denominator by $iRZ_0(1+\Delta\omega/\omega_0)$ and approximating one term in the denominator using $(1+\Delta\omega/\omega_0)^{-1} \simeq (1-\Delta\omega/\omega_0)$ yields

$$Z = \frac{R}{1 + 2i\frac{R}{Z_0}\frac{\Delta\omega}{\omega_0}} \tag{2.11}$$

Comparing to equation (2.10) and setting $\omega_{SMR} = \omega_0$ we can see that the lumped-element LRC circuit models the SMR well. For the SMR of length l, with resistance, capacitance and inductance per unit length R', C' and L' , and

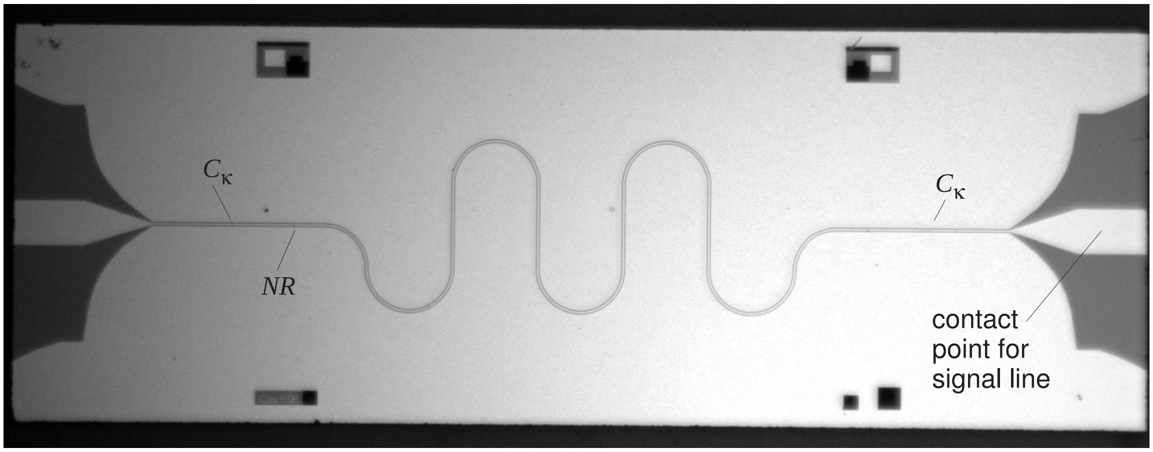

Figure 2.1: Microphotograph of 3.5mm × 10mm chip. The meandered line is coplanar waveguide. Barely distinguishable at this resolution are the centerline and gaps separating it from the groundplane. At the two ends of the chip the waveguide geometry gradually changes to an approximate microstrip ending in a bond-pad wide enough to accommodate wirebonds. The coupling capacitors C_κ define a length of CPW forming a 5.00684 GHz SMR having a measured $\kappa = 2\pi \cdot 494$kHz and coupled to 5.5717 MHz nanomechanical resonator (NR). Labels indicate positions of NR and coupling capacitors.

transmission-line characteristic impedance $Z_0' = \sqrt{L'/C'}$, for resonance of order n we can assign lumped-element equivalent circuit values

$$R = \frac{2Z_0'}{lR'} Z_0' \tag{2.12}$$

$$C = \frac{lC'}{2} \tag{2.13}$$

$$L = \frac{2}{(n\pi)^2} lL' \tag{2.14}$$

$$Z_0 = \sqrt{\frac{L}{C}} = \frac{2}{n\pi} Z_0' \tag{2.15}$$

$$\omega_{SMR} = n\frac{\pi v_{ph}}{l} = \frac{1}{\sqrt{LC}} \tag{2.16}$$

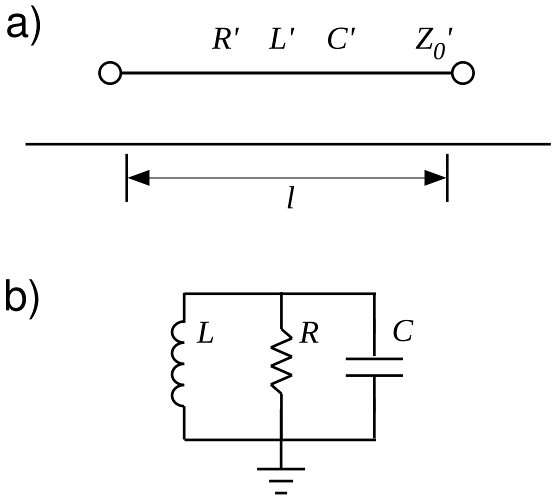

Figure 2.2: **a)** Half-wave resonator: transmission line of length l, characteristic impedance Z_0' and inductance, capacitance and resistance L', C' and R' per unit length. **b)** Lumped-element model of the resonator.

2.2 Model of driven SMR

A schematic of a typical measurement circuit appears in figure 2.3 a. The applied microwave drive signal is carried by signal lines having real characteristic impedance R_L, attenuated in power by an amount $loss$ before entering the SMR through coupling capacitor C_κ. The signal emitted by the SMR at the other end through another coupling capacitor is amplified by an amplifier having input impedance R_L matched to the signal lines. Typically, $R_L = 50\Omega$. The amplifier has power gain $gain$.

We model this in a lumped-element fashion in figure 2.3 b. The voltage V_0 equals the voltage V_{in} applied by the microwave source, attenuated by an amount $\sqrt{loss}$ in its travel down the input line. In the lumped-element model the voltage is

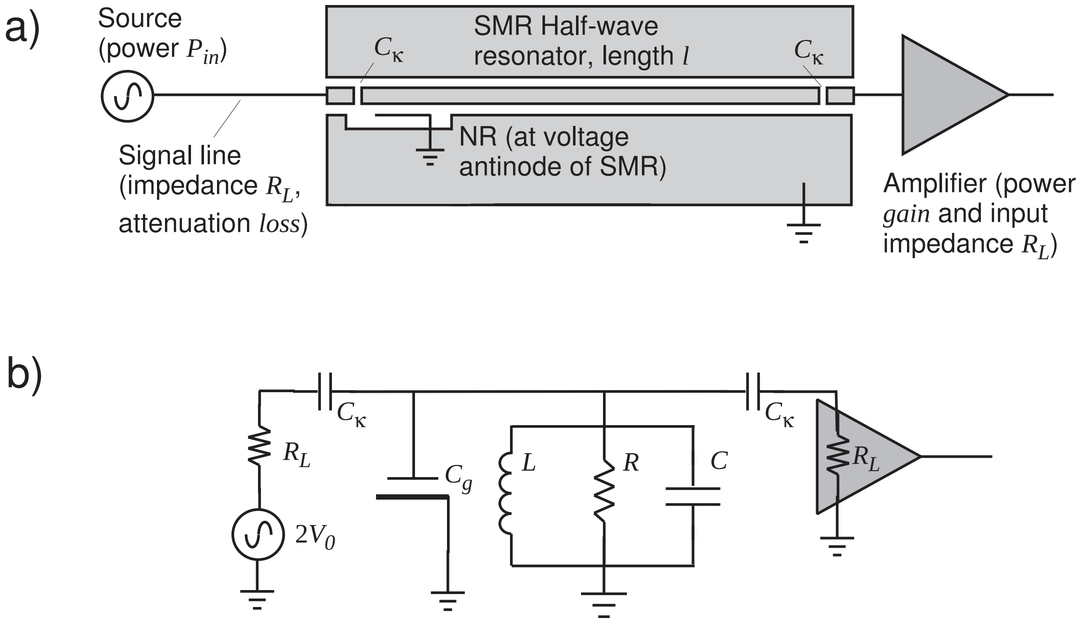

Figure 2.3: **a)** Physical circuit: half-wavelength of CPW transmission-line forming superconducting microwave resonator (SMR), driven by microwave source, and detected with microwave amplifier. The SMR is coupled capacitively to nanomechanical resonator (NR) by capacitance C_g. **b)** Lumped-element model.

$2V_0$ in series with a source resistance R_L. In this way the load (in this case the SMR plus input capacitance) sees a voltage matching that of a load on a transmission line of characteristic impedance R_L, i.e. $V_{load} = V_0 \frac{2Z_L}{Z_L+R_L} = V_0(1+\Gamma)$ (cf. equation (2.4) at $x = 0$).

Using this model we would like to find the voltage V_{SMR} within the SMR and the voltage V_{amp} emerging from it. For the time being we neglect the NR and the capacitance C_g coupling it to the SMR. We treat the LRC circuit and the C_κ-and-R_L network at the amplifier end as a combined load impedance, and apply a Norton-equivalent-circuit model to it. [11] Norton's theorem holds that if a load is driven by a source voltage in series with a source impedance, we may replace the source voltage and series impedance by a source *current* equal to the source voltage divided by source impedance, in *parallel* with the same source impedance. In our model the source voltage is $2V_0$, and source impedance is $R_L + \frac{1}{i\omega C_\kappa}$. Hence the equivalent source current is $I_{0,eq} = \frac{2V_0}{R_L+\frac{1}{i\omega C_\kappa}}$. Norton's theorem assumes that all circuit elements are linear, which our circuit model satisfies.

The model is further clarified by replacing the impedance at each end of the SMR by an *equivalent* resistance $R_{L,eq} = \frac{1+(\omega C_\kappa R_L)^2}{R_L(\omega C_\kappa)^2}$ and capacitance $C_{\kappa,eq} = \frac{C_\kappa}{1+(\omega C_\kappa R_L)^2}$ which when combined in *parallel* have a total impedance equaling $R_L + \frac{1}{i\omega C_\kappa}$. The Norton equivalent circuit with this further modification appears in figure 2.4. We can make a simplifying approximation by noting that in our system,

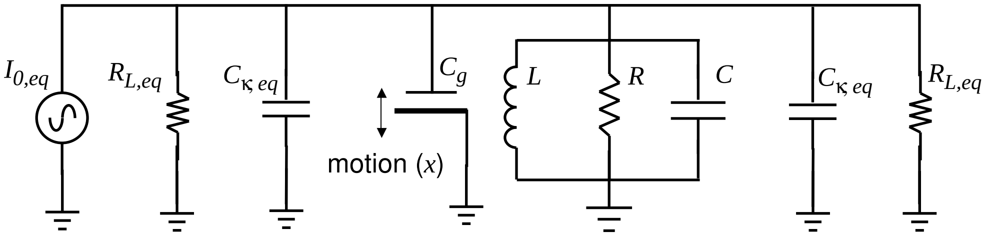

Figure 2.4: SMR model with Norton equivalent drive current $I_{0,eq}$. The Norton equivalent parallel impedance and the load impedance at the amplifier end (C_κ and R_L in series, see figure 2.3 b) have each been replaced with equivalent parallel $R_{L,eq}$ and $C_{\kappa,eq}$ network.

$\omega \simeq 2\pi \cdot 5$ GHz, $R_L \simeq 50\Omega$, and $C_\kappa \lesssim 10$ fF. Therefore $\omega C_\kappa R_L \lesssim 0.1$ and

$$I_{0,eq} \simeq 2V_0 \cdot i\omega C_\kappa \tag{2.17}$$

$$R_{L,eq} \simeq \frac{1}{R_L(\omega C_\kappa)^2} \tag{2.18}$$

$$C_{\kappa,eq} \simeq C_\kappa \tag{2.19}$$

2.2.1 Loading of resonator

These equivalent parallel impedances allow us to clarify the loading of the SMR by the external circuitry. The total capacitance becomes $C_{tot} = C + 2C_\kappa + C_g$, and the total resistance is likewise the parallel combination of R with $R_{L,eq}/2$. Because in our system, $C_g \ll C_\kappa \ll C$, we will neglect the shift in Z_0 and ω_{SMR} due to C_κ, and everywhere approximate $C_{tot} = C$. For the time being we will also neglect the behavior of the NR, and the effect of C_g on Z_0 and ω_{SMR}. However, we must consider the effect of the loading resistance $R_{L,eq}$. Here we can use the definition of quality factor for a parallel LRC circuit, $Q = R/Z_0$. Seeing that $\frac{1}{Q} = Z_0(\frac{1}{R} + \frac{2}{R_{L,eq}})$, we can restate this as $\frac{1}{Q} = \frac{1}{Q_{int}} + \frac{1}{Q_{ext}}$, thereby defining

$$Q_{int} = \frac{R}{Z_0} \tag{2.20}$$

$$Q_{ext} = \frac{R_{L,eq}}{2Z_0} \tag{2.21}$$

We can further introduce the angular-frequency linewidth $\kappa = \omega_{SMR}/Q$.

$$\kappa = \kappa_{int} + \kappa_{ext} \tag{2.22}$$

$$\begin{aligned}\kappa_{int} &= \omega_{SMR}\frac{Z_0}{R} \qquad (2.23)\\ &= \frac{1}{RC}\\ \kappa_{ext} &= \omega_{SMR}\frac{2Z_0}{R_{L,eq}}\\ &= 2R_L(\omega C_\kappa)^2\frac{1}{C} \qquad (2.24)\\ &= 4R_L(\omega C_\kappa)^2 Z_0'\frac{\omega_{SMR}}{n\pi} \qquad (2.25)\end{aligned}$$

2.2.2 Internal and output voltage of the SMR

Using the equivalent current and equivalent impedances, we can readily determine the voltage V_{SMR}.

$$\begin{aligned}V_{SMR} =& I_{0,eq}\left(i\omega C + \frac{1}{i\omega L} + \frac{1}{R} + \frac{2}{R_{L,eq}}\right)^{-1}\\ =& I_{0,eq}\left(i\frac{\omega}{\omega_{SMR}Z_0} - i\frac{\omega_{SMR}}{\omega Z_0} + \frac{\kappa_{int}}{\omega_{SMR}Z_0} + \frac{\kappa_{ext}}{\omega_{SMR}Z_0}\right)^{-1}\\ =& 2V_0 \cdot i\omega C_\kappa \cdot \frac{\omega_{SMR}Z_0}{\kappa + i(\omega - \frac{\omega_{SMR}^2}{\omega})}\\ =& 2iV_0\sqrt{\frac{\kappa_{ext}}{2R_LC}} \cdot \frac{1}{\kappa + i(\omega - \omega_{SMR})(1 + \frac{\omega_{SMR}}{\omega})}\end{aligned}$$

If $\kappa \ll \omega_{SMR}$ and we are working with frequencies within only a few linewidths of ω_{SMR}, we can further approximate $\omega_{SMR}/\omega \simeq 1$. Then we have

$$V_{SMR} = 2iV_0\sqrt{\frac{\kappa_{ext}}{2R_LC}} \cdot \frac{1}{\kappa + 2i(\omega - \omega_{SMR})} \tag{2.26}$$

We will see below in section 2.2.3 that this voltage is identical to the voltage amplitude of the standing wave within the transmission line in the SMR.

The voltage V_{amp} at the amplifier is the SMR voltage V_{SMR}, reduced by C_κ and R_L acting as a voltage divider:

$$\begin{aligned} V_{amp} =& \frac{R_L}{R_L + 1/i\omega C_\kappa} V_{SMR} \\ =& -V_0 \frac{\kappa_{ext}}{1 + i\omega R_L C_\kappa} \cdot \frac{1}{\kappa + 2i(\omega - \omega_{SMR})} \\ \simeq& -V_0 \frac{\kappa_{ext}}{\kappa + 2i\Delta\omega} \end{aligned} \tag{2.27}$$

Here we define $\Delta\omega = \omega - \omega_{SMR}$. In the last step above we assume that $\omega C_\kappa R_L \ll 1$, which is reasonable for our devices. Note that *on resonance* ($\omega = \omega_{SMR}$) we have

$$V_{amp} = -\frac{\kappa_{ext}}{\kappa} V_0 \tag{2.28}$$

$$Q_{int} = \frac{1}{1 - |\frac{V_{amp}}{V_0}|} Q \tag{2.29}$$

This is a useful expression. Since Q_{int} is often not known a priori but Q is easy to measure, we can determine the internal losses in the SMR if we can measure $\frac{V_{amp}}{V_0}$. In practice, however, this usually means knowing *loss* and *gain* to high precision.

2.2.3 Energy, power and current in the SMR

We can calculate the energy stored in the driven SMR using the expressions for energy in reactive components: $E = \frac{1}{2}CV^2 + \frac{1}{2}LI^2$, where V and I are RMS time-averaged quantities. In our model we will treat V_{SMR} as a *voltage amplitude*, for consistency with the transmisison-line voltage amplitudes in equation (2.4). Therefore $V_{SMR,rms} = \frac{1}{\sqrt{2}} V_{SMR}$. Assuming $\frac{\Delta\omega}{\omega_{SMR}} \ll 1$ we can approximate $I_{SMR} = \frac{V_{SMR}}{Z_0}$ and therefore

$$E_{SMR} = \frac{1}{2} C |V_{SMR}|^2 \tag{2.30}$$

Using equation (2.26) we can state

$$E_{SMR} = V_0^2 \frac{\kappa_{ext}}{R_L} \cdot \frac{1}{\kappa^2 + 4\Delta\omega^2}$$

Using equation (2.27) we can state

$$E_{SMR} = \frac{1}{R_L} \frac{1}{\kappa_{ext}} |V_{amp}|^2$$

The characteristic impedance of the lines leading to the SMR is R_L. Then by comparison with equation (2.6) we have $P_{in} \cdot loss = \frac{V_0^2}{2R_L}$ and $P_{out} = \frac{V_{amp}^2}{2R_L} \cdot gain$. Therefore

$$E_{SMR} = P_{in} \cdot loss \cdot \frac{2}{\kappa_{ext}} \cdot \frac{\kappa_{ext}^2}{\kappa^2 + 4\Delta\omega^2} \tag{2.31}$$

$$E_{SMR} = \frac{2}{\kappa_{ext}} \frac{P_{out}}{gain} \tag{2.32}$$

Equation (2.32) agrees with what we expect for a Lorentzian resonance. A resonator with (angular-frequency) linewidth κ dissipates its stored energy at a rate proportional to the energy times κ. Equation (2.22) shows the different dissipation rates that make up κ. The SMR emits a power $\left(\frac{\kappa_{ext}}{2} \cdot E_{SMR}\right)$ out of each end, and dissipates a power $(\kappa_{int} \cdot E_{SMR})$ internally.

From equations (2.31) and (2.32), we can also express the energy stored in the SMR as an average number $\bar{n}_{SMR}$ of photons of energy $\hbar\omega$ at the drive (i.e. pump) frequency ω:

$$\bar{n}_{SMR} = \frac{1}{\hbar\omega} P_{in} \cdot loss \cdot \frac{2}{\kappa_{ext}} \cdot \frac{\kappa_{ext}^2}{\kappa^2 + 4\Delta\omega^2} \tag{2.33}$$

$$\bar{n}_{SMR} = \frac{1}{\hbar\omega} \frac{2}{\kappa_{ext}} \frac{P_{out}}{gain} \tag{2.34}$$

In practice, in most measurements $\omega \gg \Delta\omega$ and so when it is convenient we may replace $\hbar\omega$ with $\hbar\omega_{SMR}$ in equations (2.33) and (2.34).

It is also useful to square the magnitude of both sides of equation (2.27) in order to express the power transmitted by the SMR. Considering also loss in signal lines and gain of amplifier we have

$$P_{out} = P_{in} \cdot loss \cdot \frac{\kappa_{ext}^2}{\kappa^2 + 4\Delta\omega^2} \cdot gain \tag{2.35}$$

The standing wave within the SMR consists of a wave traveling back and forth in phase, losing a fraction of power at each end and in the internal ohmic losses, balanced by the microwaves admitted at the drive end. To determine this circulating power, consider microwaves within the SMR, of power P_{SMR} impinging on the "load impedance" formed of C_κ and R_L at the amplifier end. From equations (2.6) and (2.7) it is clear that the power deposited into the load will be $P_{SMR} \cdot (1 - |\Gamma^2|)$. This power should be equal to the measured power $P_{amp} = P_{out}/gain$. For $Z_L = \frac{1}{i\omega C} + R_L$ and $\Gamma = \frac{Z_L - Z_0'}{Z_L + Z_0'}$ we have

$$\Gamma = \frac{1 + i\omega C(R_L - Z_0')}{1 + i\omega C_\kappa (R_L + Z_0')}$$

Taking $|\Gamma|^2$, Taylor-expanding the denominator, multiplying through and retaining the lowest order terms yields

$$|\Gamma|^2 = 1 - 4\omega^2 C_\kappa^2 R_L Z_0'$$

Comparing to equations (2.25) and (2.20) we find

$$P_{amp} = \frac{n\pi}{Q_{ext}} P_{SMR}$$

Therefore the circulating power in the SMR is

$$P_{SMR} = \frac{Q_{ext}}{n\pi} \cdot \frac{P_{out}}{gain} \tag{2.36}$$

$$= \frac{Q_{ext}}{n\pi} P_{in} \cdot loss \cdot \frac{\kappa_{ext}^2}{\kappa^2 + 4\Delta\omega^2} \tag{2.37}$$

where n is the order of the resonance; typically we will work with the lowest-order (half-wave) resonance, so that $n = 1$.

From equation (2.37) we can also determine the amplitude $|V_{SMR}^+|$ of the traveling wave within the SMR. Using $|V_{SMR}^+| = \sqrt{2Z_0' P_{SMR}}$ and $P_0 = P_{in} \cdot loss = \frac{V_0^2}{2R_L}$, we have

$$|V_{SMR}^+| = \sqrt{\frac{Q_{ext}}{n\pi} \frac{Z_0'}{R_L}} \cdot \frac{\kappa_{ext}}{\sqrt{\kappa^2 + 4\Delta\omega^2}} \cdot V_0 \tag{2.38}$$

Because $\Gamma \simeq 1$, at the voltage antinode at the ends of the SMR (where we place our NR) the local voltage will be $2|V_{SMR}^+|$. This is the amplitude of the standing wave voltage in the SMR. By using equation (2.15) to substitute for Z_0' and using the definitions of Q_{ext} and Z_0, we can see that $2|V_{SMR}^+|$ is identical to V_{SMR} as defined in equation (2.26).

The current of the traveling wave in the SMR can be seen from equation (2.5) to be

$$|I_{SMR}^+| = \frac{|V_{SMR}^+|}{Z_0'} \tag{2.39}$$

As with the standing wave voltage, the amplitude of the standing wave current in the SMR is equal to $2|I_{SMR}^+|$.

2.3 Design of coplanar waveguide

Coplanar waveguide (CPW) is a very convenient type of transmission line to form the SMR because it is two-dimensional, can be microfabricated easily in a single lithographic layer, concentrates most of the RF electric field in a very small region between the centerline and groundplane, and isolates the RF region extremely well via the groundplane. This isolation permits, for instance, forming tight curves and meanders of the CPW with only minimal effect on the behavior. [12] CPW is thus preferable in comparison to other structures such as microstrip and stripline.

CPW supports quasi-TEM electromagnetic waves. Approximate analytical solutions for Z_0', C' and L' in CPW may be found in books such as references [13] and [14]. As these involve elliptical integrals their presentation here will not shed much useful light on CPW design, and we instead offer a few rules of thumb:

A photograph of microfabricated CPW appears in figure 2.5. In designing CPW, the critical dimensions are the width of the centerline w_{CPW} and the gap between centerline and groundplane d_{CPW}. In particular the waveguide parameters Z_0', C' and L' scale with the ratio $\frac{w_{CPW}}{w_{CPW}+2d_{CPW}}$, so the CPW may be shrunk or enlarged yet have the same electrical behavior. The thickness of the conductor is typically much smaller than the other dimensions and has negligible effect. If both w_{CPW} and d_{CPW} are much smaller than the substrate thickness then the latter can be considered infinite and neglected. As a general rule of thumb for design, decreasing $\frac{w_{CPW}}{w_{CPW}+2d_{CPW}}$ lowers C' and increases Z_0'. In practice $Z_0' < 100\Omega$ is easily achievable but to achieve larger Z_0' approaching 200Ω, d_{CPW} must be made so wide or w_{CPW} so narrow that the CPW loses its favorable characteristics in comparison to microstrip. The phase velocity is well approximated by

$$v_{ph} = \frac{c}{\sqrt{(\epsilon_r + 1)/2}}$$

where c is the speed of light and ϵ_r is the relative dielectric constant of the substrate. In silicon ϵ_r is about 12.

As can be seen in figure 2.1, we design the chip to have at each end a bond pad for wire-bonding the CPW to the microstrip transmission line on the sample box. To avoid step-changes in Z'_0 we progressively transition the geometry from CPW to microstrip over a 1 mm distance.

The ohmic dissipation R' of the waveguide is minimized by using a superconducting metal on a low-loss substrate. Dissipation in superconducting CPW should be limited by dielectric losses, the fraction of normal-state conductors in the superconductor, and other loss mechanisms such as the motion of trapped magnetic flux vortices. These mechanisms have been the subject of many recent studies such as [11], [15], [12] and [16].

2.4 Nanomechanical resonator coupled to SMR

In this dissertation, we employ the SMR as a detector of mechanical motion and explore the backaction of the measurement on the motion. We would like to identify a measured signal that is directly related to the amplitude of the nanomechanical resonator's oscillation. Here we present a classical derivation based on the circuit model of section 2.2. Although this derivation does not explicitly incorpo-

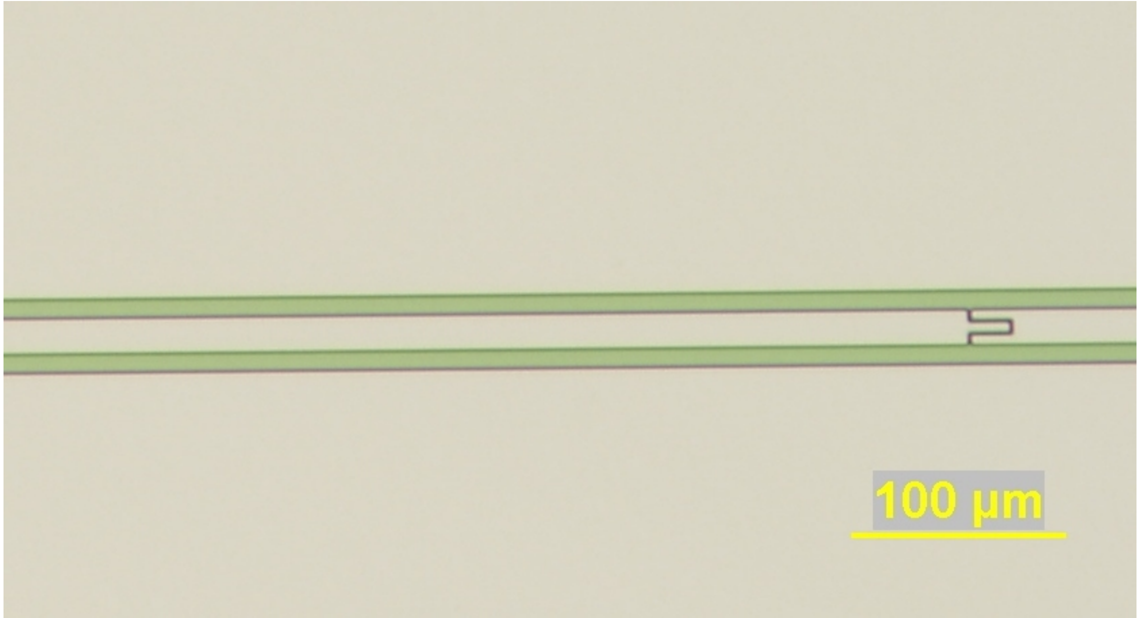

Figure 2.5: Microphotograph of coplanar waveguide. Centerline (width w_{CPW}) and centerline-to-groundplane gap (d_{CPW}) are clearly distinguishable. Also visible is the interdigitated capacitor comprising C_κ.

rate backaction effects, it is useful in being completely comprehensible in terms of simple circuit theory, and it gives a precise value for measurable signal amplitude in terms of the NR oscillation amplitude. If backaction is present, the expressions for signal amplitude remain accurate as long as the backaction effects are independently incorporated into the NR behavior.

We return to the derivation presented in section 2.2.2 for the voltage in the SMR, and introduce the motion of the NR. The capacitance C_g is a function $C_g(x)$ of the nanoresonator position x. We take the NR to be oscillating at its resonant frequency ω_{NR} with an amplitude x_0 that is much smaller than the gap d between the NR and the opposing gate electrode. Thus we can approximate C_g as

$$C_g = C_g(0) + \frac{\partial C_g}{\partial x} x_0 \cos(\omega_{NR} t + \phi_{NR})$$

Given $C_{tot} = C + 2C_\kappa + C_g$ and $\omega_{SMR} = \frac{1}{\sqrt{LC_{tot}}}$, we can expect the resonant frequency of the SMR to oscillate at frequency ω_{NR}. For small x_0 amplitude we can use a Taylor-expansion to approximate the oscillating $\omega_{SMR}(t)$. We take the partial derivative

$$\frac{\partial \omega_{SMR}}{\partial x} = -\omega_{SMR} \frac{1}{2C} \frac{\partial C_g}{\partial x} \tag{2.40}$$

where here ω_{SMR} represents the value of the SMR frequency for $x_0 = 0$, and for simplicity the equilibrium value of C_{tot} is approximated as C. Then to first order, the oscillating $\omega_{SMR}(t)$ is:

$$\omega_{SMR}(t) = \omega_{SMR} \left(1 - \frac{1}{2C} \frac{\partial C_g}{\partial x} x_0 \cos(\omega_{NR} t + \phi_{NR})\right) \tag{2.41}$$

This suggests one way to measure the motion of the NR, by measuring the oscillation frequency of the SMR. If the SMR is driven on resonance, and if the oscillation amplitude of $\omega_{SMR}(t)$ is $\ll \kappa$, the instantaneous phase of the response should follow the instantaneous value of $\omega_{SMR}(t)$ and therefore the instantaneous amplitude of the NR. This method was pursued by Regal et al. [17] in a system very similar to ours and using a homodyne detection scheme. They fed the response of their SMR+NR system into a phase-discriminating ("I-Q") microwave mixer, with a the pump signal used as a reference. The portion of the response that was out-of-phase with the reference was a direct measure of the phase of the system response and therefore of the time-varying SMR frequency. This time-varying phase output could also be examined on a spectrum analyzer to distinguish the noise spectrum of thermally-driven mechanical motion. These researchers reported that this detection scheme was susceptible to material-dependent noise in the frequency of the SMR ("phase noise") due to small fluctuations in the dielectric constant of the substrate. However, the $\omega_{NR} \ll \kappa$ of their device did make it particularly suited for a time-domain measurement. For devices having $\omega_{NR} \gg \kappa$ such as the one we have used, the situation is somewhat different. The time constant of the SMR is $\frac{1}{\kappa}$, whereas the NR oscillates with period $\frac{2\pi}{\omega_{NR}}$ which is $< \frac{1}{\kappa}$. The microwave resonator is too "slow" to respond instantaneously to the NR motion, and the phase of the driven SMR response does not accurately represent the instantaneous amplitude of the NR.

2.4.1 Differential equation for sideband voltage

Instead of observing the NR motion in the time domain, we may observe it in the frequency domain. From equation (2.41) and equation (2.27) it is evident that the system response oscillates at ω_{NR} while the drive oscillates at pump frequency ω_p and thus the emitted voltage will contain terms $\sim cos(\omega_{NR}t)cos(\omega_p t)$, which decompose into terms oscillating at $\omega_p \pm \omega_{NR}$. To calculate the expected signal we must solve for the voltage within the SMR. As discussed in section 2.2 and depicted in figure 2.4, the microwave pump signal can be expressed as an equivalent current, which we will take here to be oscillating at frequency ω_p with amplitude $I_{0,eq}$. Thus the pump signal is $I_{0,eq}\cos(\omega_p t)$. This current must equal the sum of the currents through all of the parallel components. Thus

$$I_{0,eq}\cos(\omega_p t) = \frac{\partial}{\partial t}(C_{tot}V) + \frac{1}{R_{tot}}V + \frac{1}{L}\int V dt$$

where $\frac{1}{R_{tot}} = \frac{1}{R} + \frac{2}{R_{L,eq}}$. We wish to solve for the voltage $V(t)$ within the SMR. Differentiating once and plugging in our expression for C_g we have the differential equation

$$\begin{aligned}-I_{0,eq}\omega_p \sin(\omega_p t) = {} & V\left(\frac{1}{L} - \omega_{NR}^2 \frac{\partial C_g}{\partial x} x_0 \cos(\omega_{NR}t + \phi_{NR})\right) \\ & + \dot{V}\left(\frac{1}{R_{tot}} - 2\omega_{NR}\frac{\partial C_g}{\partial x} x_0 \sin(\omega_{NR}t + \phi_{NR})\right) \\ & + \ddot{V}\left(C_{tot} + \frac{\partial C_g}{\partial x} x_0 \cos(\omega_{NR}t + \phi_{NR})\right)\end{aligned}$$

Rearranging and substituting definitions of Z_0, C, κ and ω_{SMR} yields

$$\begin{aligned}-I_{0,eq}Z_0\omega_p \sin(\omega_p t) = {} & \omega_{SMR}V\left(1 - \left(\frac{\omega_{NR}}{\omega_{SMR}}\right)^2 \frac{1}{C}\frac{\partial C_g}{\partial x} x_0 \cos(\omega_{NR}t + \phi_{NR})\right) \\ & + \frac{\kappa}{\omega_{SMR}}\dot{V}\left(1 - 2\frac{\omega_{NR}}{\kappa}\frac{1}{C}\frac{\partial C_g}{\partial x} x_0 \sin(\omega_{NR}t + \phi_{NR})\right) \\ & + \frac{1}{\omega_{SMR}}\ddot{V}\left(1 + \frac{1}{C}\frac{\partial C_g}{\partial x} x_0 \cos(\omega_{NR}t + \phi_{NR})\right) \qquad (2.42)\end{aligned}$$

The second term in each parentheses is necessarily small, because $C_g \ll C$ and therefore $\frac{1}{C}\frac{\partial C_g}{\partial x}x_0 \ll 1$. Note that if we ignore all of these small-valued terms, i.e. we set $x_0 = 0$, we can substitute the definitions of $I_{0,eq}$, Z_0, κ_{ext}, and ω_{SMR}, to readily find the voltage oscillating at ω_p. The result is identical in magnitude and phase to the previous solution, equation (2.26). Thus the NR motion should make only a negligible change in the voltage amplitude at ω_p, but we would like to find the voltages oscillating at the *sum* frequency $\omega_s = \omega_p + \omega_{NR}$ and the *difference* frequency $\omega_d = \omega_p - \omega_{NR}$. We thus expect the solution to have the form

$$V(t) = V_p cos(\omega_p t + \phi_p) + V_s cos(\omega_s t + \phi_s) + V_d cos(\omega_d t + \phi_d) \tag{2.43}$$

2.4.2 Solution for sideband voltage

By solving the differential equation, we can find the amplitude and phase of the sidebands. Conceptually we can think of the SMR-NR system as amplitude-modulating the transmitted pump signal. The SMR resonance further affects the amplitude of the sidebands generated this way.

We take $\dot{V}$ and $\ddot{V}$ of trial solution (2.43) and plug into (2.42). We collect terms and consider only the terms oscillating at ω_d or ω_s. Neglecting terms oscillating at all other frequencies and neglecting as well any terms of order $\left(\frac{\omega_{NR}}{\omega_{SMR}}\right)^2$, we have

$$\begin{aligned}
0 = {} & \omega_{SMR}\left(V_s\cos(\omega_s t+\phi_s)+V_d\cos(\omega_d t+\phi_d)\right)\\
& -\frac{\kappa}{\omega_{SMR}}\left(\omega_s V_s\sin(\omega_s t+\phi_s)+\omega_d V_d\sin(\omega_d t+\phi_d)\right)\\
& -\frac{1}{\omega_{SMR}}\left(\omega_s^2 V_s\cos(\omega_s t+\phi_s)+\omega_d^2 V_d\cos(\omega_d t+\phi_d)\right)\\
& -\frac{\omega_p}{\omega_{SMR}}\omega_p V_p\frac{1}{C}\frac{\partial C_g}{\partial x}x_0\cos(\omega_p t+\phi_p)\cos(\omega_m t+\phi_m)\\
& +2\frac{\omega_{NR}}{\omega_{SMR}}\omega_p V_p\frac{1}{C}\frac{\partial C_g}{\partial x}x_0\sin(\omega_p t+\phi_p)\sin(\omega_m t+\phi_m)
\end{aligned}$$

Applying the trigonometric identities $\cos\theta_1\cos\theta_2=\frac{1}{2}\left(cos(\theta_1-\theta_2)+cos(\theta_1+\theta_2)\right)$ and $\sin\theta_1\sin\theta_2=\frac{1}{2}\left(cos(\theta_1-\theta_2)-cos(\theta_1+\theta_2)\right)$, we find that we can further neglect terms of order $\frac{\omega_{NR}}{\omega_{SMR}}$. We approximate $(\omega_{SMR}-\frac{\omega_s}{\omega_{SMR}}\omega_s)$ as $2(\omega_{SMR}-\omega_s)$ and $(\omega_{SMR}-\frac{\omega_d}{\omega_{SMR}}\omega_d)$ as $2(\omega_{SMR}-\omega_d)$, and separate into two equations oscillating at ω_s and ω_d:

$$\begin{aligned}
& V_s\left(2(\omega_{SMR}-\omega_s)\cos(\omega_s t+\phi_s)-\kappa\frac{\omega_s}{\omega_{SMR}}\sin(\omega_s t+\phi_s)\right)\\
& \qquad =\frac{1}{2}\frac{\omega_p}{\omega_{SMR}}\omega_p V_p\frac{1}{C}\frac{\partial C_g}{\partial x}x_0\cos(\omega_s t+\phi_p+\phi_m)\\
& V_d\left(2(\omega_{SMR}-\omega_d)\cos(\omega_d t+\phi_d)-\kappa\frac{\omega_d}{\omega_{SMR}}\sin(\omega_d t+\phi_d)\right)\\
& \qquad =\frac{1}{2}\frac{\omega_p}{\omega_{SMR}}\omega_p V_p\frac{1}{C}\frac{\partial C_g}{\partial x}x_0\cos(\omega_d t+\phi_p-\phi_m)
\end{aligned}$$

To proceed, we approximate $\frac{\omega_p}{\omega_{SMR}}=1$, $\frac{\omega_s}{\omega_{SMR}}=1$ and $\frac{\omega_d}{\omega_{SMR}}=1$. We denote $\Delta\omega_d=(\omega_d-\omega_{SMR})$, $\Delta\omega_s=(\omega_s-\omega_{SMR})$ and $\Delta\omega_p=(\omega_p-\omega_{SMR})$. From equation (2.26), V_p and ϕ_p are known: $V_p=I_{0,eq}Z_0\omega_p\frac{1}{\sqrt{\kappa^2+4\Delta\omega_p^2}}$ and $\tan\phi_p=-2\Delta\omega_p/\kappa$. We then have solutions for the amplitude and phase of the upper and lower sideband voltages produced by the mechanical motion. Approximating $\omega_p\simeq\omega_{SMR}$ and using the definitions of $I_{0,eq}$ and Z_0 we find the sideband voltages within the SMR:

$$V_s = -\frac{1}{C}\frac{\partial C_g}{\partial x}x_0 \cdot \sqrt{\frac{\kappa_{ext}}{2R_L C}} \cdot \frac{\omega_{SMR}}{\sqrt{\kappa^2 + 4\Delta\omega_s^2}} \cdot \frac{1}{\sqrt{\kappa^2 + 4\Delta\omega_p^2}} \cdot V_{p,0} \tag{2.44}$$

$$\phi_s = \arctan\left(\frac{\kappa}{2\Delta\omega_s}\right) - \arctan\left(\frac{2\Delta\omega_p}{\kappa}\right) + \phi_m \tag{2.45}$$

$$V_d = -\frac{1}{C}\frac{\partial C_g}{\partial x}x_0 \cdot \sqrt{\frac{\kappa_{ext}}{2R_L C}} \cdot \frac{\omega_{SMR}}{\sqrt{\kappa^2 + 4\Delta\omega_d^2}} \cdot \frac{1}{\sqrt{\kappa^2 + 4\Delta\omega_p^2}} \cdot V_{p,0} \tag{2.46}$$

$$\phi_d = \arctan\left(\frac{\kappa}{2\Delta\omega_d}\right) - \arctan\left(\frac{2\Delta\omega_p}{\kappa}\right) - \phi_m \tag{2.47}$$

where $V_{p,0}$ is the pump voltage at the input of the SMR (equivalent to V_0 in figure 2.3 b and equation (2.26)). Note that the phase of mechanical motion appears with opposite sign in the upper and lower sideband signals.

As in section 2.2.2 we can further determine the voltages of the sidebands emitted by the SMR, and appearing at the input of the amplifier. Here we also use (2.40) to replace $\frac{1}{2C}\frac{\partial C_g}{\partial x}$ with $\frac{-1}{\omega_{SMR}}\frac{\partial \omega_{SMR}}{\partial x}$.

$$V_{s,amp} = \frac{-1}{\omega_{SMR}}\frac{\partial \omega_{SMR}}{\partial x}x_0 \cdot \frac{\omega_{SMR}}{\sqrt{\kappa^2 + 4\Delta\omega_s^2}} \cdot \frac{\kappa_{ext}}{\sqrt{\kappa^2 + 4\Delta\omega_p^2}} \cdot V_{p,0} \tag{2.48}$$

$$V_{d,amp} = \frac{-1}{\omega_{SMR}}\frac{\partial \omega_{SMR}}{\partial x}x_0 \cdot \frac{\omega_{SMR}}{\sqrt{\kappa^2 + 4\Delta\omega_d^2}} \cdot \frac{\kappa_{ext}}{\sqrt{\kappa^2 + 4\Delta\omega_p^2}} \cdot V_{p,0} \tag{2.49}$$

The output *power* of each sideband can be determined as in equation 2.35. Note that the mechanical amplitude x_0 in equations (2.48) and (2.49) is the *peak* amplitude of the NR oscillation. When describing power, it is more convenient to work in terms of the RMS mechanical oscillation $x_{RMS} = \sqrt{\langle x^2 \rangle} = \frac{1}{\sqrt{2}}x_0$. In this way the measured sideband power can be directly related to the energy $k\langle x^2 \rangle$ in the mechanical oscillation, where $k = m_{NR}\omega_{NR}^2$ is the spring constant of the mechanical oscillator.

$$P_{s,out} = P_{p,in} \cdot loss(\omega_p) \cdot \left(\frac{1}{\omega_{SMR}} \frac{\partial \omega_{SMR}}{\partial x} \right)^2 \cdot 2\langle x^2 \rangle \cdot \frac{\omega_{SMR}^2}{\kappa^2 + 4\Delta\omega_s^2} \cdot \frac{\kappa_{ext}^2}{\kappa^2 + 4\Delta\omega_p^2} \cdot gain(\omega_s) \tag{2.50}$$

$$P_{d,out} = P_{p,in} \cdot loss(\omega_p) \cdot \left(\frac{1}{\omega_{SMR}} \frac{\partial \omega_{SMR}}{\partial x} \right)^2 \cdot 2\langle x^2 \rangle \cdot \frac{\omega_{SMR}^2}{\kappa^2 + 4\Delta\omega_d^2} \cdot \frac{\kappa_{ext}^2}{\kappa^2 + 4\Delta\omega_p^2} \cdot gain(\omega_d) \tag{2.51}$$

Since in general *gain* and *loss* may be frequency-dependent, we have explicitly indicated the frequencies. This can be relevant in analyzing measured data.

2.4.3 Solutions if sideband frequency equals ω_{SMR}

In most of the measurements in this work, we use $\omega_p = \omega_{SMR} \pm \omega_{NR}$, i.e. $\Delta\omega_p = \pm\omega_{NR}$. This places one sideband at ω_{SMR} and the other at $\omega_{SMR} \pm 2\omega_{NR}$. The sideband at ω_{SMR} will be enhanced by the resonance of the SMR and in the "good cavity" or "sideband resolved" limit of $\omega_{NR} > \kappa$, the other sideband will be suppressed. The suppression of the second sideband is crucial to both backaction cooling and backaction-evading measurement. In most cases we will be interested in the sideband appearing at ω_{SMR} and will neglect the suppressed sideband. As we will see in chapter 3, the optimum frequency for backaction cooling is $\Delta\omega_p = -\omega_{NR}$.

For the specific case of $\Delta\omega_p = -\omega_{NR}$, then the upper ("sum") sideband falls at the SMR resonant frequency, i.e. $\omega_s = \omega_{SMR}$. This configuration appears in figure

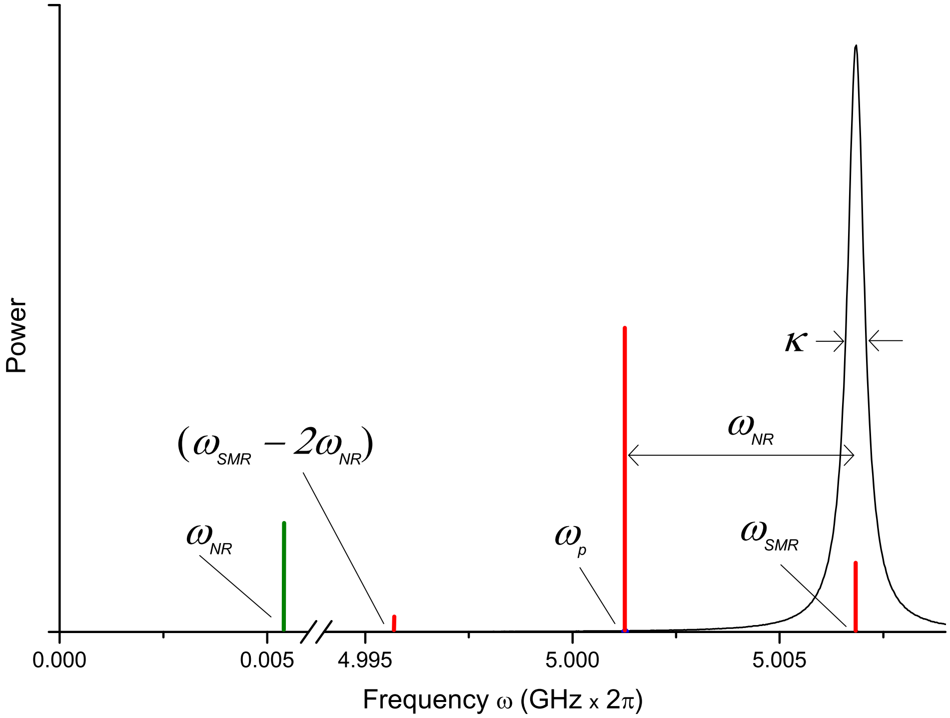

Figure 2.6: Diagram of NR, pump and sideband frequencies if $\Delta\omega_p = -\omega_{NR}$. Narrow black line is measured S21, i.e. $P_{p,out}/P_{p,in}$ of device depicted in figure 2.1, showing Lorentzian lineshape of SMR response as in equation (2.35). Horizontal axis is to scale; note the break in the axis. Vertical heights of pump and sidebands are not to scale; the size of the suppressed sideband at $\omega_{SMR} - 2\omega_{NR}$ is greatly exaggerated.

2.6. We can state the sideband voltage and power in this case:

$$V_{s,amp} = \frac{-1}{\kappa}\frac{\partial\omega_{SMR}}{\partial x}x_0 \cdot \frac{\kappa_{ext}}{\sqrt{\kappa^2 + 4\Delta\omega_p^2}} \cdot V_{p,0} \tag{2.52}$$

$$P_{s,out} = P_{p,in} \cdot loss(\omega_p) \cdot \left(\frac{1}{\kappa}\frac{\partial\omega_{SMR}}{\partial x}\right)^2 \cdot 2\langle x^2\rangle \cdot \frac{\kappa_{ext}^2}{\kappa^2 + 4\Delta\omega_p^2} \cdot gain(\omega_{SMR}) \tag{2.53}$$

If instead $\Delta\omega_p = +\omega_{NR}$, then the “difference” frequency ω_d equals ω_{SMR}. The upper sideband is suppressed, and the voltage and power in the lower sideband will be identical to equations (2.52) and (2.53).

Equations (2.48) through (2.53) offer us a set of expressions to precisely relate measured signal levels directly to mechanical motion of the NR. We derived these expressions classically, so they do not include quantum effects nor do they explicitly include the effects of measurement backaction on the mechanical motion. All of the measurements in this work are in the classical limit, and in many of our measurements, the backaction is negligible. In the case where backaction is strong, these expressions remain valid if we incorporate the effects of backaction independently into the values of ω_{NR} and $\langle x^2\rangle$.

Chapter 3

Theory and Literature Review: Backaction and Related Effects

Although a classical framework serves for the majority of the analyses and derivations in this dissertation, it is worthwhile to present the hamiltonian of our parametrically coupled SMR-NR system: [18], [19], [20]

$$\hat{H} = \hbar\left(\omega_{SMR} + g\hat{x} - \frac{\lambda}{2}\hat{x}^2\right)\left(\hat{b}^\dagger\hat{b} + \frac{1}{2}\right) + \hbar\omega_{NR}\left(\hat{a}^\dagger\hat{a} + \frac{1}{2}\right) + \hat{H}_{pump} + \hat{H}_\kappa + \hat{H}_\Gamma \tag{3.1}$$

Where

$g = \frac{\partial\omega_{SMR}}{\partial x}$ is the 1st-order coupling of SMR to NR.

$\lambda = \frac{\omega_{SMR}}{2C}\frac{\partial^2 C_g}{\partial x^2}$ is the 2nd-order coupling.

$\hat{x} = \Delta x_{ZP}(\hat{a}^\dagger + \hat{a})$ is the amplitude of NR motion.

$\hat{b}$ ($\hat{b}^\dagger$) are the lowering (raising) operators of the SMR.

$\hat{a}$ ($\hat{a}^\dagger$) are the lowering (raising) operators of the NR.

$\hat{H}_{pump}$ represents the microwave pump.

$\hat{H}_\kappa$ represents SMR damping.

$\hat{H}_\Gamma$ represents NR damping.

The term $\hbar g\hat{x} \cdot \hat{b}^\dagger\hat{b}$ shows the parametric coupling (also commonly described as a "ponderomotive" or Kerr-type coupling) of the SMR frequency to the mechanical motion, discussed classically in section 2.4. This interaction becomes critical to backaction damping and cooling of the NR motion, discussed below in section 3.1.3. The term $\hbar\lambda\hat{x}^2 \cdot \hat{b}^\dagger\hat{b}$ on the other hand results from the shifting of the NR frequency due to energy in the SMR. Under the right conditions, this will lead to parametric amplification of the NR, as described below in section 3.5. This behavior will ultimately place a limitation on the potential of our system for backaction evading measurement.

3.1 Backaction damping and cooling

Preparing a mechanical oscillator of frequency ω_m in its quantum ground state remains an experimental challenge. The average mechanical energy $k\langle x^2\rangle$ must be suppressed below a single quantum $\hbar\omega_m$. However, one must overcome the harmonic oscillator's coupling to its thermal environment, or "thermal bath", of temperature T. As a single mode with equal-spaced energy levels, we expect the oscillator to follow Bose-Einstein statistics, having average thermal occupation $\bar{n}_{th} = (e^{\hbar\omega_m/k_BT} - 1)^{-1}$. At temperatures $T \gg \frac{\hbar\omega_m}{k_B}$, we can approximate the thermal energy as $k\langle x^2\rangle = k_BT = \bar{n}_{th}\hbar\omega_m$, but to reach the regime of the ground state, the temperature must be made $< \frac{\hbar\omega_m}{k_B}$, and this defines the experimental difficulty. For instance, for $\omega_m = 2\pi \cdot 1\text{MHz}$, this temperature is equivalent to $\frac{\hbar\omega_m}{k_B} = 0.05$ mK. The "brute force" approach is to cool the environment itself by techniques such as dilution refrigeration. To date the best achieved by this method was to cool a 21.8 MHz nanomechanical resonator to $\sim$ 26mK, or $\bar{n}_{th} \simeq 25$ [3]. Alternatively, if the mode's mechanical quality factor is large, then its coupling to the thermal bath is weak. The mode can then be cooled below the thermal bath temperature by bringing it *out of equilibrium* with the environment. By coupling it strongly to another system which extracts energy from it, the *average energy of the mode* is suppressed while the mechanical structure itself remains at the bath temperature.

Historically, backaction cooling of the motion of a single mechanical mode to its ground state was first demonstrated for the motion of a single ion trapped in a harmonic potential. [21] [22]. The harmonic motion of trapped charges in an electromagnetic trap, and the coupling of the motion to the thermal environment, was a well-studied phenomenon [23] [24]. To reduce the energy of the ions to the ground state, researchers led by D. Wineland adopted the doppler-cooling technique previously developed for neutral atoms [25]. In an electromagnetic trap, the harmonic motion of the ion at frequency ω_v doppler-shifts the frequencies of its atomic transitions. The spectral line of an atomic transition at frequency ω_0 acquires sidebands at frequencies $\omega_0 \pm \omega_v$, very similarly to our SMR-NR system discussed in section 2.4. By exciting the transition at $\omega_0 - \omega_v$ with an applied laser, while permitting the ion to emit at ω_0, the ion is made to lose an energy $\hbar\omega_v$ with each transition. For successful cooling, it was found to be critical that the system be in the "resolved sideband" limit, where the linewidth κ of the atomic transition is $\ll \omega_v$. The quantum number of the ion's motion can then reach a theoretical limit $\bar{n} \simeq (\kappa/2\omega_v)^2$. Using either stimulated Raman transitions or single-photon transitions, researchers in references [21] and [22] were able to cool a $\omega_v = 3$ to 30 MHz mechanical mode to a quantum occupation $\bar{n} < 0.1$. Such well-controlled state-preparation of trapped ions has become instrumental in quantum measurements of trapped ions and in designs for using trapped ions as qubits. [26]

3.1.1 Classical analysis

Schemes for using the backaction of a radiation field to damp and cool the motion of a micromechanical or nanomechanical oscillator adapt this concept to much larger mass and size scales. [27] Rather than an atomic transition, the resonance of an optical or RF cavity is employed to extract energy from the mechanical motion. The concept is seen most readily if we consider an optical cavity one end of which is a mirror fixed to a mechanical resonator. [28] Light circulating within the cavity exerts a "ponderomotive" force on the mirror due to radiation pressure. As each photon of frequency ω bounces off of the mirror, its momentum changes by $2\hbar\omega/c$, and therefore for a power P circulating in the cavity, the mirror experiences a force $F_{rad} = 2P/c$. A harmonic oscillator subject to this force and to thermal forces F_{therm} has an equation of motion $m\ddot{x} + m\Gamma\dot{x} + kx = F_{therm} + F_{rad}$. If the mirror is oscillating at frequency ω_m, the resonant frequency of the cavity ω_c oscillates along with it. A fixed-frequency off-resonance optical drive ("pump signal") ω_{pump} is therefore brought slightly closer and slightly farther away from resonance each cycle. This means that the amount of power admitted to the cavity and therefore a portion of F_{rad} will oscillate at ω_m. Yet the ring-up time κ of the cavity ensures that the oscillating radiation-pressure force lags the motion slightly. If the oscillating motion of the mirror is $x = x_0\cos(\omega_m t)$, then the oscillating radiation-pressure force will have components both in-phase and out-of-phase with x. The in-phase component will appear as an extra contribution to the restoring-force (kx) term in the equation of motion, leading to a shift in the mechanical resonance frequency ("optical spring" effect). The out-of-phase component on the other hand will appear as an extra contribution to the $m\Gamma\dot{x}$ damping term ("optical damping" effect). The optical spring and optical damping can be either positive or negative: for a red-detuned pump ($\omega_{pump} < \omega_c$), the phase lag leads to total work per cycle $\oint F_{rad} dx < 0$, meaning the radiation-pressure force does negative work on the mechanical resonator, i.e. positive damping. For a blue-detuned pump ($\omega_{pump} > \omega_c$), the opposite is true: the radiation-pressure force does positive work, amplifying the mechanical motion, i.e. negative damping. (A good illustration of this may be seen in figure 1 of Ref. [29].)

The lag in the response of the force is the key to the damping effect. While in a later discussion we describe quantum analyses ([19] [30] [31] [32]), here we summarize some results of classical theory. In general any delay mechanism may produce similar damping behavior. One demonstration of optical damping has employed the photothermal force due to differential thermal expansion of a gold film on a silicon micromechanical resonator. [33] The energy extraction, i.e. cooling, due to such damping mechanisms will be limited by the power absorbed as heat into the mechanical resonator. Only damping derived from non-dissipative interactions with the electromagnetic field, i.e. radiation pressure or electromagnetic forces, can offer the prospect of cooling the mechanical mode into its quantum ground state. Xue et al. [34] have analyzed a coupled NR-SMR system nearly identical to ours. By introducing a delay $1 - e^{-\kappa t/2}$ into the electrostatic force on the NR due to the voltage on the SMR, they find behavior identical to that of radiation pressure acting on a moving mirror in an optical cavity. Damping increases the mechanical linewidth Γ_{NR} to Γ_{NR}^{eff}, and shifts the frequency ω_{NR} to ω_{NR}^{eff}. If the un-damped mechanical resonator has a temperature T_0, and defining the mechanical mode temperature $T_{NR} = \frac{k\langle x^2\rangle}{k_B}$, they find the spectral density S_x of position noise (note that we use throughout this work a convention of single-sided spectral densities)

$$S_x = \frac{4k_BT}{k}\frac{\omega_{NR}^2\Gamma_{NR}}{(\omega^2 - (\omega_{NR}^{eff})^2)^2 + (\Gamma_{NR}^{eff}\omega)^2}$$

Integrating to find $\langle x^2\rangle = \int_0^\infty S_x \frac{d\omega}{2\pi}$ and therefore to find T_{NR}, they conclude that

$$T_{NR} \simeq T_0\frac{\Gamma_{NR}}{\Gamma_{NR}^{eff}} \tag{3.2}$$

In this analysis, the authors assume that $\omega_{NR} \sim \kappa$, and in fact conclude that the optimum cooling occurs for detuning $\Delta\omega = \omega_{NR}/2$, and $\Delta\omega = \kappa/4$. These conditions hold for the so-called "bad cavity" regime, in which $\kappa \gtrsim \omega_m$. A full quantum analysis of this regime has also been done by Paternostro et al., for the case of the moving mirror at one end of an optical cavity. [35] Cooling in the "bad cavity" regime, however, will start to break down as the mechanical energy approaches one quantum. As will be discussed below, the "resolved sideband" or "good cavity" regime, $\omega_{NR} > \kappa$, offers the prospect of cooling the mechanical motion well below its quantum ground state.

3.1.2 Recent work in the field

Early implementations of backaction cooling were developed more than a decade ago to improve the sensitivity of resonant-bar gravitational-wave antennas by suppressing their Brownian motion. Blair et al. [36] studied ~700 kHz mechanical modes of a 1300 kg niobium bar with a 10 GHz superconducting RF cavity attached to one end so that vibrations of the bar modulated the resonant frequency of the cavity. By driving the cavity off-resonance with RF power up to -12 dBm, they were able to suppress the mechanical amplitude from an ambient temperature of 5 K to a mode temperature of 2 mK. They found that further cooling was limited by an undesired backaction driving effect due to amplitude noise in their microwave source. (Similar effects are discussed below in section 3.3.) A more recent demonstration of backaction cooling of a macroscopic mechanical resonator was done by Brown et al. [37], who demonstrated RF backaction cooling in the non-sideband-resolved regime, using a 1 mm-long mechanical resonator of frequency 7 kHz, coupled to a 100 MHz resonant RF cavity having $\kappa \simeq 2\pi \times 430$ kHz.

For micro or nanomechanical resonators, active interest in backaction cooling began earlier this decade, and initial demonstrations used non-sideband-resolved devices. Gigan et al. [38] [39] cooled a 280 kHz mechanical resonator from room temperature to 8K, while Arcizet et al. [40] cooled a 814 kHz microresonator to about 10K. A related technique was reported by Naik et al. [41] [3] who used the backaction of shot-noise in charge motion through a superconducting single-electron transistor to cool the 21.9 MHz fundamental mode of a nanomechanical resonator from a starting temperature of 550 mK to a final mode temperature of 300 mK.

In more recent work, most researchers have improved their devices to operate in the sideband-resolved regime. Gröblacher et al. have used the most "conventional" geometry for their cooling experiments, i.e. a free-space optical cavity of linear geometry, with a mechanically-resonant mirror at one end. With this system they cooled the 945 kHz fundamental mechanical mode of a 100-micron-long resonator having a high-reflectance mirror attached to it. Starting from a cryostat temperature of 5.3 K, they achieved a backaction-cooled mode temperature of 1.5 mK, or ~ 32 mechanical quanta. [42]

Schliesser et al. [43] have reported optical backaction cooling on the motion of a radial breathing mode of a silica microtoroid that also functions as a whispering-gallery-mode optical cavity. Laser power is coupled into the optical resonator by the evanescent mode of an optical fiber, and radiation pressure acts radially on the structure as the light circulates. Initial measurements cooled the 58 MHz mechanical mode from room temperature to 11 K, or ~ 400 quanta. Later measurements extended this system into the sideband-resolved regime, and achieve higher cooling powers, broadening the mechanical linewidth of a 74.5 MHz mechanical mode up to 1.5 MHz. [44] This work was later improved by performing it in a 1.6 K cryostat. This lower starting temperature enabled a 65 MHz mechanical mode to be cooled to an occupation of ~ 63 quanta. [45] Park and Wang [46] recently demonstrated a similar interaction between mechanical modes and whispering-gallery optical modes of a silica microsphere. By making the sphere slightly prolate, they were able to excite its optical modes by evanescent coupling to a free-space laser beam. The optical resonance of a 26.5 micron sphere had $\kappa = 2\pi \cdot 29.7$ kHz and permitted cooling of its 118.6 MHz mechanical mode by a factor of 6.6 starting from 1.4K, achieving an occupation of ~ 37 mechanical quanta.

Thompson et al. [47] have demonstrated yet another technique in which a partially-reflecting membrane resonator is placed within a high-finesse optical cavity. Radiation pressure then acts on the mechanical resonator from both sides. They were able to backaction-cool the 134 kHz mechanical mode to a temperature of 6.8 mK, or $\sim$ 1080 quanta. This technique also has the advantage that the membrane may be positioned in the cavity standing wave so that the emitted power is directly sensitive to the mean squared amplitude $\langle x^2 \rangle$ of the motion. This may ultimately permit a "quantum non-demolition" measurement of the total energy (see sections 3.4.1 and 3.4.2).

Teufel et al. [48] [49] used a coupled SMR-NR system very similar to our own, except that the SMR comprised a quarter-wave resonant length of CPW transmission line. This system operated in the sideband-resolved regime and used backaction of the microwave field to damp and cool a 1.52 MHz nanomechanical resonator from the refrigerator temperature of 50 mK to $\sim$ 10 mK, or an occupation of 140 quanta.

3.1.3 Summary of quantum analysis

Quantum analyses of backaction cooling of a mechanical mode coupled to an optical cavity have been presented in references [19], [30] and [31], focusing specifically on the sideband-resolved or "good cavity" regime $\omega_m \gg \kappa$. Another valuable quantum analysis appears in Ref. [32], dealing with an SMR coupled to NR motion via the current in a SQUID embedded in the SMR. Such a system obeys the same form of hamiltonian as ours does in equation (3.1), with the g coupling in the $\hbar g \hat{x} \cdot \hat{b}^\dagger \hat{b}$ term deriving from the magnetic flux and current in the SQUID. It therefore can be analyzed in a similar way to the optical systems, with the same results regarding backaction cooling. We will describe here the general concepts of

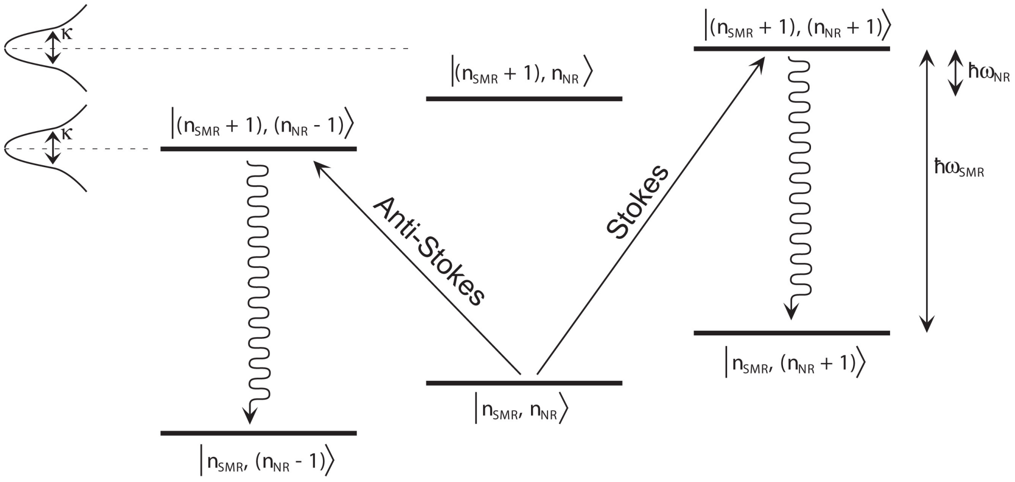

Figure 3.1: Schematic energy level diagram for optical backaction cooling or heating processes. Adapted from Ref. [44].

such analyses and summarize their results.

Figure 3.1 shows a schematic energy level diagram for NR-SMR interactions. Backaction cooling or heating of the NR may be understood in terms of the Stokes and anti-Stokes scattering processes familiar from atomic and molecular physics. Pumping the SMR mode with a photon of energy $\hbar(\omega_{SMR}-\omega_{NR})$ ("red detuning", anti-Stokes process) or energy $\hbar(\omega_{SMR}+\omega_{NR})$ ("blue detuning", Stokes process) excites the coupled SMR-NR system to raise the SMR occupation one quantum while lowering (raising) the NR occupation one quantum. The excited SMR mode then decays, with the large density of states at the SMR resonance favoring decay by an amount $\hbar\omega_{SMR}$. The SMR returns to its initial state but the NR is left with one less (more) quantum than before. Repetition of the anti-Stokes (Stokes) process cools (heats) the NR. Intuitively, we expect the repetition rate, and thus the cooling or heating rate, to scale with the number of incident scattering photons, i.e. the total number of photons in the cavity.

Anti-Stokes

$$\Big|n_{SMR}, n_{NR}\Big\rangle \longrightarrow \Big|(n_{SMR}+1), (n_{NR}-1)\Big\rangle \qquad \text{(excitation)}$$

$$\Big|(n_{SMR}+1), (n_{NR}-1)\Big\rangle \longrightarrow \Big|n_{SMR}, (n_{NR}-1)\Big\rangle \qquad \text{(decay)}$$

Stokes

$$\Big|n_{SMR}, n_{NR}\Big\rangle \longrightarrow \Big|(n_{SMR}+1), (n_{NR}+1)\Big\rangle \qquad \text{(excitation)}$$

$$\Big|(n_{SMR}+1), (n_{NR}+1)\Big\rangle \longrightarrow \Big|n_{SMR}, (n_{NR}+1)\Big\rangle \qquad \text{(decay)}$$

Figure 3.1 also illustrates the advantage of working in the sideband-resolved regime $\omega_{NR} \gg \kappa$. SMR linewidth κ represents broadening of the energy levels; if $\omega_{NR} \ll \kappa$ then the $\Big|(n_{SMR}+1), (n_{NR}-1)\Big\rangle$ and $\Big|(n_{SMR}+1), (n_{NR}+1)\Big\rangle$ levels overlap; there becomes a sizable probability that an excitation to the former state will nonetheless decay to $\Big|n_{SMR}, (n_{NR}+1)\Big\rangle$. This also makes sense in terms of the energy-time uncertainty relationship $\Delta t \Delta E \sim \hbar$, familiar from time-dependent perturbation theory, considering the decay time of the SMR to be $\frac{1}{\kappa}$. [50] The decay to $\Big|n_{SMR}, (n_{NR}+1)\Big\rangle$ will compete with the anti-Stokes-type cooling process and diminish the cooling rate. The importance of suppressing this heating behavior becomes more evident as the mechanical mode approaches its quantum ground state $n_{NR} = \frac{1}{2}$. As there is no lower energy state of the NR, the anti-Stokes process cannot extract further energy from the NR, but the competing heating process is unchanged.

We can think of the optical-cooling of the harmonic-oscillator mode of the NR in terms of a rate equation for energy transfer to and from the mode. A similar analysis was presented by Naik et al. in regard to backaction cooling of a NR mode using the shot noise of charge moving through a single-electron transistor. [3] The thermal environment, or thermal "bath", at temperature T, emits energy to the NR at rate $\Gamma_{NR} \cdot k_B T$, where Γ_{NR} is the natural, or thermal, linewidth of the NR. On the other hand the NR mode having total energy $\hbar\omega_{NR}\bar{n}_{NR}$ emits energy to its environment at a rate equal to $\Gamma_{tot} \cdot \hbar\omega_{NR}\bar{n}_{NR}$, where Γ_{tot} is the total decay rate due to thermal and all other causes. If the NR mode is in equilibrium with the thermal bath, then $\Gamma_{tot} = \Gamma_{NR}$ and $\bar{n}_{NR} = \bar{n}^T_{NR} = \frac{k_B T}{\hbar\omega_{NR}}$. Now introduce another, "optical" temperature bath $k_B T_{opt} = \hbar\omega_{NR}\bar{n}^{opt}_{NR}$ and damping rate Γ_{opt}. Thus $\Gamma_{tot} = \Gamma_{NR} + \Gamma_{opt}$. Then in steady state the emissions to and from the NR mode balance and we have $\Gamma_{tot} \cdot \bar{n}_{NR} = \Gamma_{NR} \cdot \bar{n}^T_{NR} + \Gamma_{opt} \cdot \bar{n}^{opt}_{NR}$, or

$$\bar{n}_{NR} = \frac{\Gamma_{opt}\bar{n}^{opt}_{NR} + \Gamma_{NR}\bar{n}^T_{NR}}{\Gamma_{opt} + \Gamma_{NR}} \tag{3.3}$$

This *detailed balance equation* balances the emission and absorption processes in the NR mode. This balance is illustrated in figure 3.2. For the interaction of the NR with the microwave mode in the SMR, we must determine $\bar{n}^{opt}_{NR}$ and Γ_{opt}. The NR coupled in this way to the microwave mode will then achieve a mode temperature $T_{NR} = \frac{\hbar\omega_{NR}}{k_B}\bar{n}_{NR}$ (assuming that $\bar{n}_{NR} >> 1$ so that we may neglect Bose-Einstein statistics for the NR mode occupation).

Marquardt et al. [19] have used a quantum noise analysis to find $\bar{n}^{opt}_{NR}$ and Γ_{opt} in the case of a mechanically-resonant mirror coupled to an optical cavity mode by radiation pressure. Their results are readily generalized to the SMR-NR system. Wilson-Rae et al. [30] and Genes et al. [31] have found similar results using a variety of approaches.

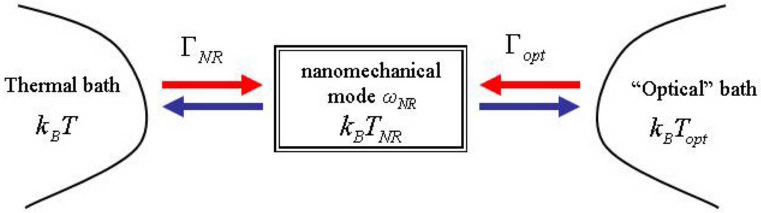

Figure 3.2: Conceptual illustration of cooling process, showing balance of energy emission and absorption rates that result in NR mode temperature T_{NR}. The NR is coupled to thermal bath of average energy $k_BT = \hbar\omega_{NR} \cdot \bar{n}^T_{NR}$ at rate Γ_{NR}. In addition, the mechanical mode is coupled to "optical" bath $k_BT_{opt} = \hbar\omega_{NR} \cdot \bar{n}^{opt}_{NR}$, at rate Γ_{opt}.

The "optical" bath $T_{opt} = \hbar\omega_{NR}\bar{n}^{opt}_{NR}$ may be thought of as an effective temperature for backaction heating of the NR by the microwave energy in the SMR [19]. This quantifies the effect of the lower-probability decay processes described above in reference to figure 3.1. $\bar{n}^{opt}_{NR}$ is the ratio of the rate of transitions that add energy to the NR mode, to the total optical damping rate. [29] Marquardt et al. find

$$\bar{n}^{opt}_{NR} = -\frac{(\omega_{NR} + \Delta\omega)^2 + (\kappa/2)^2}{4\omega_{NR}\Delta\omega} \tag{3.4}$$

where $\Delta\omega = \omega_{SMR} - \omega_{pump}$. For the optimal heating and cooling pump frequencies $\omega_{RED} = \omega_{SMR} - \omega_{NR}$ and $\omega_{BLUE} = \omega_{SMR} + \omega_{NR}$, i.e. for $\Delta\omega = \mp\omega_{NR}$, the optical damping is given by

$$\Gamma_{opt} = \pm 4\left(\Delta x_{ZP}\frac{\partial\omega_{SMR}}{\partial x}\right)^2 \frac{1}{\kappa}\bar{n}_{SMR} \cdot \frac{1}{1 + (\kappa/4\omega_{NR})^2} \tag{3.5}$$

where $\bar{n}_{SMR}$ is the number of photons in the SMR due to the coherent pump signal. This is consistent with our discussion of transition rates above, which suggested that the cooling rate should scale with the total number of microwave photons in the cavity. In equation (3.5), blue pumping yields negative optical damping, and red pumping yields positive damping. In the sideband resolved limit, equation (3.5) reduces to approximately

$$\Gamma_{opt} = \pm 4 \left(\Delta x_{ZP} \frac{\partial \omega_{SMR}}{\partial x} \right)^2 \frac{1}{\kappa} \bar{n}_{SMR} \tag{3.6}$$

In this regime we can also consider $\bar{n}_{NR}^{opt}$. From equation 3.4 we see that for $\Delta\omega = +\omega_{NR}$ we have $\bar{n}_{NR}^{opt} \simeq -1$ and for $\Delta\omega = -\omega_{NR}$ we have

$$\bar{n}_{NR}^{opt} = \left(\frac{\kappa}{4\omega_{NR}} \right)^2 \tag{3.7}$$

This dependence on the square of the ratio $\frac{\kappa}{\omega_{NR}}$ appears also in the limiting occupation number determined for laser backaction cooling of trapped ions [25]. (In fact, an exact calculation [29] finds this value of $\bar{n}_{NR}^{opt}$ in equation (3.7) only for frequency $\Delta\omega = -\omega_{NR}\sqrt{1 + (\frac{\kappa}{2\omega_{NR}})^2}$, but for $\omega_{NR} >> \kappa$ the difference is small enough to neglect. Also, such a small difference in pump frequency has negligible effect on the damping rate Γ_{opt} and therefore would not be experimentally relevant until an experiment is in a position to achieve $\bar{n}_{NR} < 1$.)

Considering the detailed balance equation, Eq. (3.3), we see that in the limit $\Gamma_{opt} \to \infty$, $\bar{n}_{NR}^{opt}$ sets a lower limit on the temperature to which the NR mode may be cooled. This confirms our expectation that sideband-resolved cooling enables attainment of the lowest occupations. For blue pumping, on the other hand, $\bar{n}_{NR}$ diverges rapidly as Γ_{opt} approaches $-\Gamma_{NR}$, and leads to self-oscillation of the NR when $\Gamma_{tot} = \Gamma_{opt} + \Gamma_{NR}$ falls below zero. In nearly all cases experimentally, then, we will have $\Gamma_{NR}\bar{n}_{NR}^{T} \gg \Gamma_{opt}\bar{n}_{NR}^{opt}$, so we may neglect the first term in the numerator of equation (3.3). The detailed balance equation reduces to

$$\bar{n}_{NR} = \frac{\Gamma_{NR}\bar{n}_{NR}^{T}}{\Gamma_{tot}} \tag{3.8}$$

This closely resembles the classical result, Eq. (3.2). The more exact quantum solution, however, predicts maximum cooling for the sideband-resolved regime and for $\Delta\omega = -\omega_{NR}$, in contrast to the classical analysis which finds maximum cooling for $\kappa \sim \omega_{NR}$. We do note that Eq. (3.7) predicts a minimum possible cooled $\bar{n}_{NR}$ of $\frac{1}{4}$ even for the non-sideband-resolved condition of $\kappa = 2\omega_{NR}$. [19]

We can also gain further insights by plugging the expression for $\bar{n}_{SMR}$ (Eq. (2.33)) into Eq. (3.6):

$$\Gamma_{opt} = 4\left(\Delta x_{ZP}\frac{\partial\omega_{SMR}}{\partial x}\right)^2 \frac{1}{\kappa}\frac{1}{\hbar\omega_{SMR}}P_{in}\cdot loss\cdot\frac{2}{\kappa_{ext}}\cdot\frac{\kappa_{ext}^2}{\kappa^2+4\Delta\omega^2} \tag{3.9}$$

By equating $k\langle x^2\rangle = \bar{n}_{NR}\hbar\omega_{NR}$ we can express

$$\langle x^2\rangle = 2\bar{n}_{NR}(\Delta x_{ZP})^2 \tag{3.10}$$

Comparing to Eq. (2.53) we see that

$$P_{sideb} = \Gamma_{opt}\bar{n}_{NR}\cdot\hbar\omega_{SMR}\cdot\frac{\kappa_{ext}/2}{\kappa}\cdot gain(\omega_{SMR}) \tag{3.11}$$

This is exactly what we would expect. The power seen in the sideband equals the rate $\Gamma_{opt}\cdot\bar{n}_{NR}$ at which photons are upconverted by the scattering process, times the energy $\hbar\omega_{SMR}$ per upconverted photon, times the fraction $\frac{\kappa_{ext}/2}{\kappa}$ which emerges from the SMR into the amplifier.

3.1.4 Experimental tradeoffs

In the device used for backaction cooling in this dissertation, we had $\omega_{NR} \simeq 11\kappa$, meaning that the theoretical lower limit to which we could cool would be $\bar{n}_{NR} \simeq 5 \cdot 10^{-4}$. Of course we didn't get anywhere near this due to other limitations. In this light it's worth examining equations (3.6) and (3.8) to see what experimental adjustments will maximize the cooling power and minimize the NR occupation. We can further approximate equation (3.8) in the limit $\Gamma_{opt} \gg \Gamma_{NR}$ as

$$\bar{n}_{NR} \simeq \frac{\Gamma_{NR}}{\Gamma_{opt}} \bar{n}^{T}_{NR} \tag{3.12}$$

Plugging in the definition of Δx_{ZP} and of $\frac{\partial \omega_{SMR}}{\partial x}$ (equation (2.40)) to Eq. (3.6) we have

$$\Gamma_{opt} = \frac{\hbar}{2} \frac{1}{m\omega_{NR}} \left(\frac{\partial C_g}{\partial x}\right)^2 \left(\frac{\omega_{SMR}}{C}\right)^2 \frac{1}{\kappa} \bar{n}_{SMR} \tag{3.13}$$

We can further plug in Eq. (2.33) for $\bar{n}_{SMR}$. Assuming $\Delta\omega = -\omega_{NR}$, and that $\omega_{NR} \gg \kappa$, we have

$$\Gamma_{opt} \simeq \frac{\hbar}{m\omega_{NR}} \left(\frac{\partial C_g}{\partial x}\right)^2 \left(\frac{\omega_{SMR}}{C}\right)^2 \frac{\kappa_{ext}}{\kappa} \cdot \frac{1}{4\omega_{NR}^2} \frac{P_{in} \cdot loss}{\hbar\omega_{SMR}} \tag{3.14}$$

The first thing to note is that there are distinct benefits in increasing the SMR resonance frequency ω_{SMR}, lowering its capacitance C and diminishing its internal losses, so that $\kappa_{ext} \simeq \kappa$. In practice, lowering the SMR capacitance C can be done by lowering the line impedance Z_0' of the transmission line resonator, or by switching to a different design in which the SMR is a lumped-element oscillator whose C may be adjusted more freely. Concerning $loss$, while losses in the signal lines will generally be greater at greater frequencies, this probably won't offset the benefit of increasing

ω_{SMR}. Decreasing the mass of the NR is beneficial if this can be done without adversely affecting $\frac{\partial C_g}{\partial x}$ or ω_{NR}. Increasing $\frac{\partial C_g}{\partial x}$ is a challenge in engineering the NR, as will be seen in the discussion of fabrication, section 4.3. For our NR design, it can be increased by reducing the gap between the NR and gate electrode across from it, which both increases C_g and its derivative, or by lengthening the NR to increase C_g. Lengthening the NR however decreases ω_{NR} proportionally. It would appear from Eq. (3.14) that reducing ω_{NR} would be very beneficial, as long as we maintain $\omega_{NR} > \kappa$, but this is not necessarily so. Comparing with Eq. (3.12) it is evident that in terms of occupation number, because the thermal bath *temperature* rather than $\bar{n}_{NR}^T$ is fixed by the environment, one factor of ω_{NR} will be canceled by the factor in $\bar{n}_{NR}^T = \frac{k_B T}{\hbar\omega_{NR}}$. The other two factors of ω_{NR} appearing in Eq. (3.14) serve only to increase $\bar{n}_{SMR}$ by placing the pump frequency closer to the SMR resonance. However, in practice, unfavorable side effects such as absorption heating of the NR by microwaves will tend to increase with $\bar{n}_{SMR}$, so it is often wise to minimize the $\bar{n}_{SMR}$ that will give a desired level of cooling.

Here Eq. (3.13) is a better guide. Diminishing κ improves the cooling efficiency for a given $\bar{n}_{SMR}$, but increases the pump power necessary to achieve that $\bar{n}_{SMR}$. A very important consideration in backaction cooling is the off-resonance noise emitted by commercial microwave sources. In contrast to lasers, microwave sources are not quantum-limited photon sources, and exhibit a large amount of phase noise and amplitude noise which will appear as white noise that falls off gradually at frequencies away from the carrier. For $\omega_{pump} = \omega_{SMR} - \omega_{NR}$, the noise at $\omega_{pump} + \omega_{NR}$ will excite the SMR resonance, leading to backaction driving of the NR that competes with the cooling process. (See section 3.3.) The noise level emitted by the source is lower at a larger amount ω_{NR} away from the carrier, but it also scales directly with pump power. Section 4.5 describes techniques we have developed to suppress this noise, up to certain levels of pump power.

It is also important to keep in mind that the expression for the cooling rate, Eq. (3.6), is based on an assumption of linear coupling between SMR and NR, which becomes invalid if pump power is increased too far. For instance, attempting to increase Γ_{opt} beyond κ has little benefit, because the system enters a nonlinear coupling regime, which limits the cooling rate. [19] At high powers, the resulting large shifts in SMR frequency due to SMR-NR coupling can also lead to nonlinear effects. While the measurements described here do not enter such a regime, future experiments probably will. It is possible to quantify these effects by finding expressions for Γ_{opt} that include higher-order coupling terms. [32] These considerations therefore emphasize the value of starting at a low thermal occupation $\bar{n}_{NR}^{T}$ of the resonator. Thus because many of these various parameters also present fabrication and testing challenges (for instance, whether or not a microwave source is available to operate at ω_{SMR}), the correct trade-offs are not always clear when designing a device.

3.2 Shift in NR frequency by optical spring effect

In addition to adding or subtracting damping from the NR mode, the electromagnetic field within the SMR also shifts the equilibrium position of the NR, and shifts its resonance frequency. As described classically in section 3.1.1 for the case of a mechanically-resonant mirror in an optical cavity, the force of the electromagnetic radiation on the NR will oscillate with the NR motion because it is varying the resonance frequency of the SMR. The force oscillating in phase with the NR adds effectively to the kx term in the equation of motion of the NR; this effective change in the spring constant k modifies the resonance frequency $\omega_{NR} = \sqrt{\frac{k}{m}}$.

To estimate this "optical-spring" effect, Marquardt et al. use a quantum noise analysis as for calculating the backaction cooling. [19] (Identical results have been found elsewhere, [31]) They find a shift $\Delta\omega_{NR}$ in the NR frequency ω_{NR} as a function of the detuning of the pump $\Delta\omega = \omega_{pump} - \omega_{SMR}$ from the cavity resonance:

$$\Delta\omega_{NR} = 8\left(\Delta x_{ZP}\frac{\partial\omega_{SMR}}{\partial x}\right)^2 \cdot \bar{n}_{SMR} \cdot \Delta\omega \frac{\kappa^2 + 4(\Delta\omega^2 - \omega_{NR}^2)}{(\kappa^2 + 4(\Delta\omega - \omega_{NR})^2) \cdot (\kappa^2 + 4(\Delta\omega + \omega_{NR})^2)} \tag{3.15}$$

We note that in the special case where $\Delta\omega = \pm\omega_{NR}\sqrt{1 + (\kappa/2\omega_{NR})^2}$, the optical-spring frequency shift $\Delta\omega_{NR}$ will be zero. For a sideband-resolved device, this condition occurs when $\Delta\omega \simeq \pm\omega_{NR}$.

The optical damping of the NR Γ_{opt} may also be expressed as a function of $\Delta\omega$. Marquardt et al. [19] find

$$\Gamma_{opt} = -8\left(\Delta x_{ZP}\frac{\partial\omega_{SMR}}{\partial x}\right)^2 \cdot \bar{n}_{SMR} \cdot \frac{8\Delta\omega \cdot \omega_{NR} \cdot \kappa}{(\kappa^2 + 4(\Delta\omega - \omega_{NR})^2) \cdot (\kappa^2 + 4(\Delta\omega + \omega_{NR})^2)} \tag{3.16}$$

In the case $\Delta\omega = \mp\omega_{NR}$, this reduces to equation (3.5). Marquardt et al. also express the optical damping and optical-spring frequency shift compactly in a convenient notation based on the response function of the optical cavity.

3.3 Backaction cooling while the SMR is thermally excited

Equation (3.3) allows us to consider two distinct cooling regimes. As described in section 3.1.3, when we consider that the SMR is excited only by a pump tone (and its associated shot noise), then for a sideband-resolved system $\bar{n}_{NR}^{opt} \ll 1$. In practice then we may neglect $\bar{n}_{NR}^{opt}$ altogether.

However, if the SMR is excited by a second source of broadband classical noise the situation is different. An SMR driven by photons of both energy $\hbar(\omega_{SMR} - \omega_{NR})$ and $\hbar\omega_{SMR}$ enables transitions that emit quanta at the difference energy, i.e. $\hbar\omega_{NR}$, thereby adding energy to the NR mode. This backaction heating process is distinct from the undesired transitions discussed in section 3.1.3, which set lower limits on $\bar{n}_{NR}^{opt}$ as indicated in Eq. (3.4). Here the rate of the heating process will be proportional to the photon flux at ω_{SMR}.

One process that introduces such photons is thermal excitation of the SMR above its ground state, i.e. Johnson noise within the SMR. In practice we may treat any process that drives the cavity with broadband noise at frequencies near ω_{SMR} as if the SMR were thermally excited. We let $\bar{n}_{SMR}^{T}$ represent the average thermal occupation of the SMR. The actual source may be Johnson noise originating in other components of the system, or phase noise of the microwave source, or RF noise deliberately introduced to the SMR as in the demonstration of backaction evasion: all will excite the SMR above its ground state to a level we will denote $\bar{n}_{SMR}^{T}$. Phase noise in the microwave pump source is of particular interest here. Recent theoretical work looking at the effects of pump phase noise [51] shows that as long as $\Gamma_{opt} << \kappa$ and $\omega_{NR} >> \kappa$, the effects of phase noise are indistinguishable from amplitude noise.

We can apply equations (2.31) and (2.32) to noise power densities $S_{N,in}$ and $S_{N,out}$ rather than single-frequency powers P_{in} and P_{out}, and consider $\hbar\omega_{SMR} \cdot \bar{n}^T_{SMR}$ to be the total energy in the cavity integrated over all frequencies. Then we can consider the thermal occupation of the SMR to be driven by a white noise (in units of W/angular frequency)

$$S_{N,in} = \frac{1}{loss} \cdot \hbar\omega_{SMR}\bar{n}^T_{SMR} \cdot \frac{\kappa}{\pi\kappa_{ext}} \tag{3.17}$$

The SMR excited to $\bar{n}^T_{SMR}$ will emit a noise spectrum (in units of W/angular frequency)

$$S_{N,out} = gain \cdot \hbar\omega_{SMR}\bar{n}^T_{SMR} \cdot \frac{\kappa}{\pi\kappa_{ext}} \cdot \frac{\kappa^2_{ext}}{\kappa^2 + 4\Delta\omega^2} \tag{3.18}$$

The thermal occupation of the SMR may be found from the measured noise spectral density $S_{N,out}(\omega_{SMR})$ (in units of W/angular frequency) at the SMR peak frequency:

$$\bar{n}^T_{SMR} = \frac{1}{\hbar\omega_{SMR}} \cdot \frac{\pi\kappa}{\kappa_{ext}} \cdot \frac{1}{gain} S_{N,out}(\omega_{SMR}) \tag{3.19}$$

If $S_{N,out}(\omega_{SMR})$ instead has units of W/Hz (which are the typical measurement units on a spectrum analyzer) then equation (3.19) should be divided by 2π.

A. Clerk has extended the theoretical calculation of Ref [19] to include the case where the SMR is excited to thermal occupation $\bar{n}^T_{SMR}$. [52]. He finds that the optical damping (equation (3.6)) and the detailed balance expression (equation (3.3)) remain valid to describe the cooling process, but that the effective backaction temperature is given by

$$\bar{n}_{NR}^{opt} = \left(\frac{\kappa}{4\omega_{NR}}\right)^2 + \bar{n}_{SMR}^{T}\left(1 + 2\left(\frac{\kappa}{4\omega_{NR}}\right)^2\right) \tag{3.20}$$

In the sideband resolved limit, we then have approximately $\bar{n}_{NR}^{opt} = \bar{n}_{SMR}^{T}$. Considering this in equation (3.3) it is important to note that the NR occupation $\bar{n}_{NR}$ can never be lower than $\bar{n}_{SMR}^{T}$.

When $\bar{n}_{SMR}^{T} > 0$, the resulting backaction driving of the NR will produce a sideband signal at ω_{SMR} that is coherent with but 180 degrees out of phase with the SMR noise at ω_{SMR}. (This will be discussed further in section 3.4.) The sideband signal due to backaction thus subtracts from the SMR noise at ω_{SMR} while the signal due to NR thermal noise adds to it incoherently, as illustrated in figure 3.3. This behavior resembles the "noise squashing" that has been seen in feedback cooling of some optomechanical systems. [53] The calculation in Ref. [52] finds the spectral solution $S_{N,out}(\delta)$ (in units of W/angular frequency) at measured frequencies $\omega_{SMR}+\delta$, where $\delta \ll \kappa$

$$S_{N,out}(\delta) = gain \cdot \hbar\omega_{SMR} \cdot \frac{\kappa_{ext}}{\pi\kappa}\left(\frac{\Gamma_{NR}\Gamma_{opt}}{4\delta^2 + \Gamma_{tot}^2}\bar{n}_{NR}^{T} + \left(1 - \frac{\Gamma_{opt}(\Gamma_{NR} + \Gamma_{tot})}{4\delta^2 + \Gamma_{tot}^2}\right)\bar{n}_{SMR}^{T}\right) \tag{3.21}$$

To find the total *measured* sideband power, we neglect the term in equation (3.21) equaling the background level at the SMR resonance frequency (see (3.19)) and integrate: $P_{sideb} = \int (S_{N,out}(\delta) - S_{bgd})\, d\delta$. Comparing the result to equation (3.11), we see that when $\bar{n}_{SMR}^{T} > 0$, what we actually measure is an *effective* mechanical occupation, $\bar{n}_{NR}^{eff}$, given by

$$\bar{n}_{NR}^{eff} = \frac{\Gamma_{NR}}{\Gamma_{opt} + \Gamma_{NR}}\bar{n}_{NR}^{T} - \left(1 + \frac{\Gamma_{NR}}{\Gamma_{opt} + \Gamma_{NR}}\right)\bar{n}_{SMR}^{T} \tag{3.22}$$

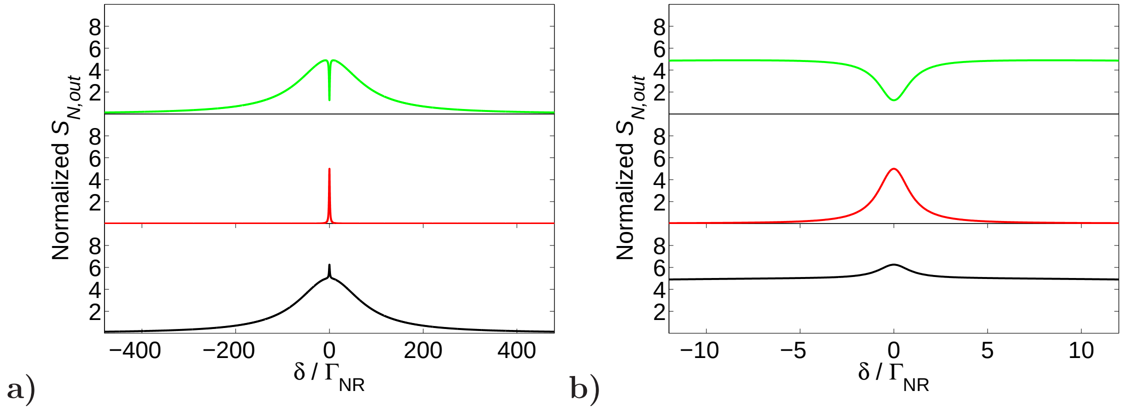

Figure 3.3: Noise spectrum of thermally-excited SMR and NR during backaction cooling, calculated from Eq. (3.21). Parameters are not experimental, only for illustration: $\Gamma_{opt} = \Gamma_{NR}$, $\kappa = 160\Gamma_{NR}$. Green curve: backaction only, $\bar{n}^T_{SMR} = 5$, $\bar{n}^T_{NR} = 0$. Red curve: thermal noise only, $\bar{n}^T_{SMR} = 0$, $\bar{n}^T_{NR} = 20$. Black curve: $\bar{n}^T_{SMR} = 5$, $\bar{n}^T_{NR} = 20$. Noise spectrum scaled by $gain \cdot \hbar\omega_{SMR} \cdot \frac{\kappa_{ext}}{\pi\kappa}$. **a)** Wide span showing full span of emitted SNR thermal noise. Here equation (3.18) has been combined with (3.21) to calculate the full SMR spectrum. **b)** Same calculation over a narrower span showing NR sideband only.

Here the term $\frac{\Gamma_{NR}}{\Gamma_{opt}+\Gamma_{NR}}\bar{n}_{NR}^{T}$ represents the NR thermal noise while the term $-\left(1+\frac{\Gamma_{NR}}{\Gamma_{opt}+\Gamma_{NR}}\right)\bar{n}_{SMR}^{T}$ represents the backaction signal subtracting coherently from the SMR noise. Note that for $\bar{n}_{SMR}^{T} = \bar{n}_{NR}^{T} \cdot \frac{\Gamma_{NR}}{\Gamma_{NR}+\Gamma_{tot}}$, no sideband at all will appear, and for $\bar{n}_{SMR}^{T} > \bar{n}_{NR}^{T} \cdot \frac{\Gamma_{NR}}{\Gamma_{NR}+\Gamma_{tot}}$ the sideband will appear as a "dip" in the SMR noise rather than a peak. We may use Eq. (3.22) along with equation (3.3) with $\bar{n}_{NR}^{opt} = \bar{n}_{SMR}^{T}$ to calculate the actual NR occupation $\bar{n}_{NR}$ during the combined backaction cooling and backaction excitation due to SMR excitation $\bar{n}_{SMR}^{T}$. In terms of the *measured* quantities $\bar{n}_{NR}^{eff}$ and $\bar{n}_{SMR}^{T}$ we find

$$\bar{n}_{NR} = \bar{n}_{NR}^{eff} + 2\bar{n}_{SMR}^{T} \tag{3.23}$$

3.4 Backaction-evading (BAE) single quadrature detector

In trying to measure any physical quantity with high precision, one eventually runs up against limitations imposed by quantum mechanics. Any observable quantity, represented by a quantum mechanical operator $\hat{A}$, will have a conjugate observable $\hat{B}$, for which the uncertainties in the two observables $\langle \Delta A^2 \rangle$ and $\langle \Delta B^2 \rangle$ must obey the uncertainty relation [50]

$$\langle \Delta A^2 \rangle \langle \Delta B^2 \rangle \geq \frac{1}{4} |\langle [\hat{A}, \hat{B}] \rangle|^2 \tag{3.24}$$

In principle there is no problem in measuring A to arbitrary precision, if you measure it only once. The complementary observable B absorbs the penalty in imprecision. But for any practical measurement, in particular in measuring mechanical motion, one wants to measure some quantity of the system *continuously*, or at least at regular intervals. We often think of measurements in quantum mechanics in terms of a process wherein you prepare an ensemble of identical systems in the same state, and then measure each one to establish the various outcomes and their probabilities. Here the situation is completely different, because *repeated* measurements on a *single system* are not in general *independent*. Each measurement of A adds uncertainty to B, and if B is coupled to A in any way then the imprecision of B will "contaminate" that of A. This is *quantum measurement backaction*.

3.4.1 Quantum non-demolition (QND) measurements: formalism

We would like to measure mechanical motion in a way that is immune from such measurement backaction. The trick, then, is to identify observables which are *decoupled* from their complementary observables, and figure out how to measure them. We want to do the measurement in such a way that one measurement does not add to the uncertainty of later measurements; the measured value is entirely predictable based on the result of earlier measurements. This is known as a *quantum non-demolition* (QND) *or back-action evading* (BAE) measurement. A good review of the quantum theory involved appears in the paper by Bocko and Onofrio. [54] Braginsky and Khalili [55] provide a similar discussion, and a further analysis of back-action-evading and quantum nondemolition measurements of mechanical oscillators appears in the review by Caves et al. [56].

Here it is valuable to employ the "Heisenberg picture" of quantum analysis. [50] As opposed to the Schrödinger picture in which the state kets evolve in time while an operator observable $\hat{A}$ does not, in the Heisenberg picture the operators evolve according to a unitary transformation $\hat{A}(t) = \hat{U}^\dagger \hat{A} \hat{U}$, where $\hat{U}$ is the time-evolution operator $\hat{U} = e^{-i\hat{H}t/\hbar}$ and $\hat{H}$ is the system hamiltonian. The state kets $|\alpha\rangle$ representing the state of the system, meanwhile, are time-independent while the base kets $|a\rangle$ (here the eigenstates of operator $\hat{A}(t)$) evolve in time via the conjugate of the time evolution operator: $|a(t)\rangle = \hat{U}^\dagger |a(0)\rangle$. The time evolution of the operator will follow the Heisenberg equation of motion

$$\frac{d}{dt}\hat{A}(t) = \frac{\partial}{\partial t}\hat{A}(t) + \frac{1}{i\hbar}[\hat{A}(t), \hat{H}] \tag{3.25}$$

To define the requirements for a QND measurement, consider a system described by hamiltonian $\hat{H}_0$. To measure observable $\hat{A}$ of this system we use a measurement apparatus described by hamiltonian $\hat{H}_M$. The interaction between the measurement apparatus and the system is defined by interaction hamiltonian $\hat{H}_I$, dependent on both $\hat{A}$ and on some observable $\hat{Q}$ of the measurement apparatus. Our first measurement at time t_0 using operator $\hat{A}(t_0)$ casts the system into an eigenstate $|a(t_0)\rangle$ of $\hat{A}(t_0)$. But because in the Heisenberg picture the state kets do not evolve, the system remains in this same state until our next measurement at time t_1. In order for the second measurement using operator $\hat{A}(t_1)$ (or subsequent measurements using $\hat{A}(t_n)$) to give predictable results, the system ought to remain in the same state after the measurement. That means $|a(t_0)\rangle$ should also be an eigenstate of $\hat{A}(t_1)$. This is satisfied if $\hat{A}(t_1)$ is just a function of $\hat{A}(t_0)$. That is, the different-time operators must commute. Thus for a QND observable, the "different-time commutator" must vanish:

$$[\hat{A}(t_m), \hat{A}(t_n)] = 0 \tag{3.26}$$

In general, Eq. (3.26) may be true only at specific discrete instances. In such case, $\hat{A}(t)$ is a "stroboscopic" QND observable. [54] A more rigorous condition is to require Eq. (3.26) to be true at all times, making $\hat{A}(t)$ a "continuous" QND observable. If $\hat{A}(t)$ does not change at all, i.e. if it is a *constant of the motion*, $\frac{d}{dt}\hat{A}(t) = 0$, then this condition is satisfied. To identify such an observable, we use the Heisenberg equation of motion (Eq. (3.25)), with $\hat{H}_0$ as the hamiltonian. If $\hat{A}(t)$ satisfies the condition

$$\frac{\partial}{\partial t}\hat{A}(t) + \frac{1}{i\hbar}[\hat{A}(t), \hat{H}_0] = 0$$

then it is a constant of the free evolution of the system. To measure it, we must find an interaction hamiltonian $\hat{H}_I$ that makes $\frac{d}{dt}\hat{A}(t) = 0$ still be true even if $\hat{H}_I$ is added to $\hat{H}_0$. This is satisfied if $\hat{A}(t)$ commutes with the interaction hamiltonian:

$$[\hat{A}(t), \hat{H}_I] = 0 \tag{3.27}$$

A convenient form for $\hat{H}_I$ is to be linearly dependent on both $\hat{A}$ and on measurement observable $\hat{Q}$, with some coupling constant $K(t)$: [54]

$$\hat{H}_I = K(t) \cdot \hat{A}(t) \cdot \hat{Q}$$

3.4.2 Harmonic oscillator quadratures as QND observables

To apply the formalism of QND observables to the harmonic oscillator, consider the hamiltonian of our SMR-NR system, Eq. (3.1). In terms of the notation used in section 3.4.1, the $\hbar\omega_{SMR}\left(\hat{b}^\dagger\hat{b} + \frac{1}{2}\right)$, $\hat{H}_{pump}$ and $\hat{H}_\kappa$ terms together comprise $\hat{H}_M$. The $\hbar\omega_{NR}\left(\hat{a}^\dagger\hat{a} + \frac{1}{2}\right)$ term meanwhile is $\hat{H}_0$. We will assume that we may neglect the NR dissipation term $\hat{H}_\Gamma$. In terms of the QND formalism, it is legitimate to do so as long as the measurement noise dominates over thermal noise, i.e. if the measurement exchanges a quantum of energy with the measured system in a time shorter than $\bar{n}^T_{NR}\Gamma_{NR}$. In practice, we will see that the backaction-evading nature of our measurement scheme is valid even if the NR is strongly driven by thermal noise.

We can go into some further detail on the operators

$$H_0 = \frac{1}{2m}\hat{p}^2 + \frac{m\omega_{NR}^2}{2}\hat{x}^2$$

$$\hat{x} = \Delta x_{ZP}(\hat{a}^\dagger + \hat{a})$$

$$\hat{p} = im\omega_{NR} \cdot \Delta x_{ZP}(\hat{a}^\dagger - \hat{a})$$

$$\hat{a} = \frac{1}{2\Delta x_{ZP}}\left(\hat{x} + i\frac{1}{m\omega_{NR}}\hat{p}\right)$$

$$\hat{a}^\dagger = \frac{1}{2\Delta x_{ZP}}\left(\hat{x} - i\frac{1}{m\omega_{NR}}\hat{p}\right)$$

The question is, what can we select as a QND observable, and what $\hat{H}_I$ to use to detect it? One readily appealing QND observable is the average energy in the NR, $E_{NR} = \hbar\omega_{NR}\bar{n}_{NR}$. Indeed this is the observable corresponding to the hamiltonian $\hat{H}_0$ itself, so it is thereby a constant of the motion. However, practical measurement of E_{NR} is very difficult. Classically, the average mechanical energy is proportional to the squared average position amplitude, $E_{NR} = k\langle x^2\rangle$, as described in section 2.4. However, as we will see later, the $\hbar\lambda\hat{x}^2\left(\hat{b}^\dagger\hat{b} + \frac{1}{2}\right)$ term in our system is too weak for easy measurement of $\langle x^2\rangle$. Other measurement schemes strongly sensitive to $\hat{x}^2$ have been demonstrated by e.g. Thompson et al. [47], but remain to be perfected.

We could consider position x as a QND observable. Taking the different-time commutator we find [54]

$$[\hat{x}(t_m), \hat{x}(t_n)] = \frac{i\hbar}{m\omega_{NR}} \sin(\omega_{NR}(t_n - t_m))$$

Evidently, the NR position serves as a QND observable only instantaneously at time intervals $(t_n - t_m) = \pi/\omega_{NR}$ and integer multiples thereof. The momentum p has similar behavior. [54] Thus the position or momentum of the NR can conceivably be measured in a "stroboscopic" QND fashion, making very brief measurements each half-cycle of NR motion. This is technically very challenging, and requires a very large coupling to achieve reasonable sensitivities in this very short duty cycle of measurement.

Instead, we can define the *quadrature amplitudes* $\hat{X}_1$ and $\hat{X}_1$ with explicit time-dependence [54] [55]

$$\left(\hat{x} + i\frac{1}{m\omega_{NR}}\hat{p}\right) = \left(\hat{X}_1 + i\hat{X}_2\right) e^{-i\omega_{NR}t}$$

Restating, we have

$$\begin{aligned} \hat{X}_1(t) &= \hat{x}\cos(\omega_{NR}t) - \frac{1}{m\omega_{NR}}\hat{p}\sin(\omega_{NR}t) \\ \hat{X}_2(t) &= \hat{x}\sin(\omega_{NR}t) - \frac{1}{m\omega_{NR}}\hat{p}\cos(\omega_{NR}t) \\ \hat{x} &= \hat{X}_1\cos(\omega_{NR}t) + \hat{X}_2\sin(\omega_{NR}t) \\ \hat{p} &= m\omega_{NR}\left(\hat{X}_2\cos(\omega_{NR}t) - \hat{X}_1\sin(\omega_{NR}t)\right) \end{aligned} \tag{3.28}$$

The raising and lowering operators may be restated in terms of $\hat{X}_1$ and $\hat{X}_2$.

$$\begin{aligned} \hat{a} &= \frac{1}{2\Delta x_{ZP}}\left(\hat{X}_1 + i\hat{X}_2\right) e^{-i\omega_{NR}t} \\ \hat{a}^\dagger &= \frac{1}{2\Delta x_{ZP}}\left(\hat{X}_1 - i\hat{X}_2\right) e^{i\omega_{NR}t} \end{aligned}$$

We can also find the commutator of $\hat{X}_1$ and $\hat{X}_2$.

$$[\hat{X}_1, \hat{X}_2] = i\frac{\hbar}{m\omega_{NR}}$$

From the commutator, and equation (3.24), we find the uncertainty relation of the two quadratures to be

$$\Delta X_1 \Delta X_2 \geq \frac{\hbar}{2m\omega_{NR}} \tag{3.29}$$

We can restate the hamiltonian $\hat{H}_0$ in terms of $\hat{X}_1$ and $\hat{X}_2$.

$$\hat{H}_0 = \frac{m\omega_{NR}^2}{2}\left(\hat{X}_1^2 + \hat{X}_2^2\right)$$

By determining the commutator of $\hat{H}_0$ with $\hat{X}_1$ and $\hat{X}_2$, and the partial time-derivatives of $\hat{X}_1$ and $\hat{X}_2$

$$[\hat{H}_0, \hat{X}_1] = -i\hbar\omega_{NR}\hat{X}_2$$

$$[\hat{H}_0, \hat{X}_2] = i\hbar\omega_{NR}\hat{X}_1$$

$$\frac{\partial}{\partial t}\hat{X}_1 = -\omega_{NR}\hat{X}_2$$

$$\frac{\partial}{\partial t}\hat{X}_2 = \omega_{NR}\hat{X}_1$$

we see by the Heisenberg equation of motion (Eq. (3.25)) that the two quadrature amplitudes are constants of the motion with respect to $\hat{H}_0$. They are thus continuous QND observables.

$$\frac{d}{dt}\hat{X}_1 = 0$$

$$\frac{d}{dt}\hat{X}_2 = 0$$

It remains for us to choose either $\hat{X}_1$ or $\hat{X}_2$ and identify an interaction hamiltonian $\hat{H}_I$ that commutes with it and also represents a feasible measurement. Our best bet is to use the $\hbar g \hat{x} b^\dagger b$ term in the hamiltonian (Eq. (3.1)), adjusting the parameter $b^\dagger b$ experimentally by varying the SMR pump to make the interaction commute with $\hat{X}_1$. We see however that the $\hbar \lambda \hat{x}^2 b^\dagger b$ term is likely to cause trouble, because it may not commute with $\hat{X}_1$ even if the $\hbar g \hat{x} b^\dagger b$ term is made to do so. In the following, we will neglect the weaker $\hat{x}^2$-dependent term. In practice, as we will see in sections 3.5 and 6.5, this means a restriction on the pump strengths at which we can work.

A good choice of interaction hamiltonian is to modulate the coupling at frequency ω_{NR}, by modulating the electric field in the SMR. [54]

$$\hat{H}_I = E_0 \cos(\omega_{NR} t) \hat{x} \hat{Q} \tag{3.30}$$

where E_0 is the electric field amplitude and $\hat{Q}$ represents the charge on the coupling capacitance C_g. Restating this in terms of quadrature amplitudes, we have

$$\begin{aligned} \hat{H}_I &= E_0 \cos(\omega_{NR} t) \hat{x} \hat{Q} \\ &= E_0 \cos(\omega_{NR} t) \left(\hat{X}_1 \cos(\omega_{NR} t) + \hat{X}_2 \sin(\omega_{NR} t) \right) \hat{Q} \\ &= \frac{E_0}{2} \left((1 + \cos(2\omega_{NR} t)) \hat{X}_1 + \sin(2\omega_{NR} t)) \hat{X}_2 \right) \hat{Q} \end{aligned}$$

If the oscillating components of this measurement are then filtered out, only the DC portion remains:

$$\hat{H}_I = \frac{E_0}{2} \hat{X}_1 \hat{Q} \tag{3.31}$$

This $\hat{H}_I$ commutes with $\hat{X}_1$, thus enabling a continuous QND measurement of that quadrature of the NR oscillation. In practice, the way that we can make the coupling have the form of equation (3.30) is to apply a pump tone at ω_{SMR}, fully modulated at frequency ω_{NR}. This is equivalent to pumping simultaneously with equal strength at two tones, $\omega_{SMR} - \omega_{NR}$ and $\omega_{SMR} + \omega_{NR}$.

$$\begin{aligned}\hat{H}_I &= E_0 \cos(\omega_{SMR} t) \cos(\omega_{NR} t) \hat{x}\hat{Q} \\ &= \frac{E_0}{2} \left(\cos((\omega_{SMR} - \omega_{NR})t) + \cos((\omega_{SMR} + \omega_{NR})t)\right) \hat{x}\hat{Q} \qquad (3.32)\end{aligned}$$

The filtering needed to arrive at equation (3.31) will also filter out the oscillations at frequency ω_{SMR}. This pumping scheme thus offers a practical means for QND measurement of quadrature amplitude $\hat{X}_1$.

The filtering is provided automatically by the SMR resonance. If our device works in the sideband-resolved limit, $\kappa \ll \omega_{NR}$, then the SMR decay time is much longer than the NR oscillation period, and the signal emerging from the SMR faithfully represents the measurement indicated by the desired interaction hamiltonian (Eq. (3.31)). [54]

The selection of the X_1 quadrature is illustrated in figure 3.4. We can regard this measurement scheme as acting sort of like a lock-in amplifier! Of the two quadratures comprising the full motion $\hat{x}$ (Eq. (3.28)), the measurement selects only the one in phase with the modulation of the pump. However, there is a subtle and important difference here from measuring $\hat{x}$ and feeding the measurement into a lock-in amp. The difference is that no information about $\hat{X}_2$ emerges from the SMR, and that the filtering takes place *before* the amplification of the signal, which unavoidably adds noise. [54] Thus by avoiding measurement backaction the double-pump measurement scheme should preserve the ability to continuously measure the amplitude X_1 with a precision beyond that which is physically possible for x.

We should keep in mind that this discussion of a QND or backaction-evading measurement deals only with effects on the NR by the measurement interaction itself. The backaction evasion eliminates these effects on the measured observable. In practice, however, we expect the NR to be subject to forces arising from sources other than the act of measurement. These will in general affect both quadratures of the NR motion, and will be fully visible during the QND measurement. In fact, in many proposed applications the whole point of the QND measurement is to observe such effects - for instance, the impulse of gravitational waves on the mass of the mechanical resonator. When we described a QND observable in section 3.4.1 as having to be "predictable", this is in respect only to the effects of measurement. The point is to suppress the measurement backaction as a source of noise with respect to more interesting signals.

3.4.3 Classical backaction evasion and limitations of real devices

If we model the backaction classically, the behavior of the double-pump QND-type measurement is readily apparent. In section 3.3 we discussed classical backaction due to noise exciting the SMR while the SMR is pumped off-resonance. Evasion of classical noise in the SMR (due to amplifier noise, thermal excitation or noise in the pump) is an important application of BAE techniques. The classical behavior of backaction evasion serves as a useful analogue for the quantum regime in which backaction driving of the NR would arise due to microwave shot noise. A measurement that demonstrates sensitivity to only a single quadrature of NR motion, and that demonstrates insensitivity to classical noise in the SMR, can be expected to behave as a QND measurement when the measurement enters the quantum regime, i.e. when pump power is sufficiently high to drive the NR with microwave shot noise.

To describe the backaction force in classical terms, we refer to the circuit model of the coupled SMR and NR, described in section 2.4. Consider the voltage within the SMR to consist of a pump tone at frequency $\omega_{SMR} + \omega_{NR}$ or $\omega_{SMR} - \omega_{NR}$, as well as a noise signal at frequency $\omega \simeq \omega_{SMR}$:

$$V_{SMR}(t) = V_p \cos((\omega_{SMR} \pm \omega_{NR})t) + V_n \cos(\omega t + \phi_n) \tag{3.33}$$

where V_n is a noise amplitude that is random in time and corresponds to a mean-squared average voltage noise density S_V (in units of volts^2 per angular frequency) at frequencies around ω_{SMR}, while ϕ_n is a random phase. The voltage on the SMR falls also across C_g, generating a backaction force on the NR equal to $F_{BA} = \frac{1}{2}\frac{\partial C_g}{\partial x} V_{SMR}^2$. (For simplicity we'll denote $\frac{\partial C_g}{\partial x}$ as $\frac{\partial C}{\partial x}$.) We can see that of the various terms in V_{SMR}^2, only the cross-term $2V_p \cos((\omega_{SMR} \pm \omega_{NR})t) \cdot V_n \cos(\omega t + \phi_n)$ will apply a force at the right frequencies to drive the NR. We decompose this term into two terms, one of which goes as $\cos((\omega_{SMR} \pm \omega_{NR})t - \omega t - \phi_n)$, and discard the other. If we denote $\delta\omega = \omega_{SMR} - \omega$, we have, for $\omega_{pump} = \omega_{SMR} \pm \omega_{NR}$,

$$F_{BA} = \frac{1}{2}\frac{\partial C}{\partial x} V_p V_n \cos((\omega_{NR} \pm \delta\omega)t \mp \phi_n)$$

Considering only the components of noise that lead to driving at the NR resonance, i.e. $\delta\omega \simeq 0$, gives insight into the BAE effect. For $\omega_{pump} = \omega_{SMR} \pm \omega_{NR}$, we then have $F_{BA} = \frac{1}{2}\frac{\partial C}{\partial x} V_p V_n \cos(\omega_{NR} t \mp \phi_n)$. Yet if we apply *both* pumps in the BAE configuration, each of amplitude V_p, and make them phase-coherent with one another, the force appearing at ω_{NR} due to *each* pump derives from the *same* voltage noise at ω_{SMR}, making the two components of backaction force phase-coherent with one another. The total force is then

$$\begin{aligned} F_{BA} &= \frac{1}{2}\frac{\partial C}{\partial x} V_p V_n (\cos(\omega_{NR} t - \phi_n) + \cos(\omega_{NR} t + \phi_n)) \\ &= \frac{\partial C}{\partial x} V_p V_n \cos(\omega_{NR} t) \cos(\phi_n) \end{aligned} \tag{3.34}$$

Thus in the BAE pump configuration it is evident that despite the random phase of the noise at ω_{SMR}, the NR is driven only at a single phase, dictated by the phase of the pump tones. The force in Eq. (3.34) is proportional to $\cos(\omega_{NR} t)$ and not $\sin(\omega_{NR} t)$. In this condition, the backaction drives only one quadrature of NR motion. The driven quadrature is designated as X_2.

The backaction-driving being confined to X_2 is half of the story. The other half is that the measurement measures exclusively X_1. We can examine this behavior using the classical analysis of sideband amplitudes described in section 2.4, where the pump tone within the SMR was described as $V_p \cos(\omega_p t + \phi_p)$, and ϕ_p identified with respect to the phase of the pump signal at the input of the SMR as $\phi_p = \arctan\left(\frac{-2\Delta\omega_p}{\kappa}\right)$. Here we have $\omega_p = \omega_{SMR} \pm \omega_{NR}$ and assume that the phase of each input pump tone is adjusted to zero the phase of the voltage within the SMR as in Eq. (3.33). Now we note that a harmonic oscillator driven on resonance acquires a $\frac{\pi}{2}$ phase shift relative to the driving force. Thus the phase ϕ_m of the mechanical motion driven by the backaction force will be $\frac{\pi}{2}$ relative to F_{BA}. The solution for sidebands appearing within the pumped SMR due to mechanical motion is given in equations (2.44) to (2.47), where (V_s, ϕ_s) are amplitude and phase of an upper (sum) sideband and (V_d, ϕ_d) apply to a lower (difference) sideband. It can be seen from these expressions that the phase of an upper sideband follows ϕ_m while that of a lower sideband follows $-\phi_m$. These have been termed respectively "phase preserving" and "phase conjugating" detection of the motion. [54] [32] For two pumps in the BAE configuration, one upper sideband will be generated by the red pump and one lower sideband by the blue pump, overlapping at ω_{SMR} having a difference in phase $\phi_s - \phi_d = 2\phi_m$. For the backaction-driven motion, the phase is $\phi_m = \frac{\pi}{2}$, making the two sidebands cancel. Thus no backaction-driven motion will appear as a sideband at ω_{SMR}. The X_2 quadrature of mechanical motion is invisible to the measurement. Mechanical motion of truly random phase, such as thermal motion, will have amplitude in both X_1 and X_2 quadratures, and will thus generate a sideband.

Calculation of the backaction force (Eq. (3.34)) enables calculation of the X_2 amplitude as a function of SMR noise and pump amplitudes. This has been done classically by Bocko and Onofrio [54] [57] as well as by Clerk et al. [20] [58] using a quantum-noise analysis. It is important to note that the backaction force described in Eq. (3.34) is an idealized case because it considers only backaction forces arising from the noise at ω_{SMR}. In fact, the pump at $\omega_{SMR} - \omega_{NR}$ will also mix with noise at $\omega_{SMR} - 2\omega_{NR}$, while the pump at $\omega_{SMR} + \omega_{NR}$ will mix with noise at $\omega_{SMR} + 2\omega_{NR}$, to generate forces at ω_{NR}. These forces are incoherent and will thus

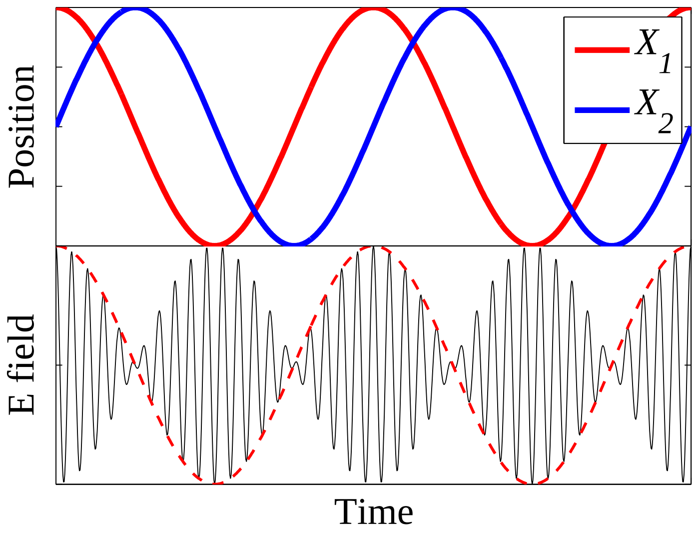

Figure 3.4: Schematic illustration of electric field in SMR for single-quadrature detection, as in equation (3.32). Beating of pump field defines quadratures X_1 and X_2 of mechanical motion.

excite both X_1 and X_2. The driving of X_1 imposes a limit on the effectiveness of the backaction evasion. However because of the Lorentzian lineshape, the voltage noise at $\omega_{SMR} \pm 2\omega_{NR}$ will be much smaller, approximately a factor of $\frac{\kappa}{4\omega_{NR}}$ times the level at ω_{SMR}. Taking the X_1 position noise density (the square of the amplitude, having units of m^2/Hz) due to these two forces and summing them to find the total S_{X_1}, and comparing this to the X_2 position noise density, yields a quantitative measure of the BAE effectiveness. The result strongly illustrates the value of being in the sideband-resolved regime in order to make these measurements efficiently: [57]

$$\frac{S_{X_2}}{S_{X_1}} = \frac{32\omega_{NR}^2}{\kappa^2} + 3 \tag{3.35}$$

Past experimental investigations of backaction-evading single quadrature detection have been undertaken primarily for improvement of measurement of vibratingbar gravitational-wave antennas. In these devices, backaction evasion was sought as a means of counteracting the effects of amplifier noise on the measured device. Noise in pump sources or thermal noise in electrically resonant transducers could also be a concern. Two representative efforts appear in the work by Marchese et al. [57] and by Cinquegrana et al. [59]. The former group employed a 50 kHz resonant bridge circuit consisting of two LC oscillators sharing a common inductor and common ground connection. A 1.87 kHz, 0.2 kg torsional mechanical oscillator simultaneously modulated the capacitances in the two arms of the bridge, in inverse fashion, so that $\frac{\partial C}{\partial x}$ in one arm was equal and opposite to that in the other arm. The resonant bridge was excited with coherent double pump signals and white noise, while a separate actuator and transducer allowed the mechanical motion to be directly excited and monitored independently of the bridge. This work was able to clearly demonstrate sensitivity to a single X_1 quadrature of motion, and to demonstrate insensitivity to the motion excited by the backaction of the white noise. A particular feature of this work was the use of the independent transducer to observe the backaction-driven mechanical motion in both the X_1 and X_2 quadratures, enabling measurement of the complete "noise elipse" for the backaction driving. For their circuit having $\omega_{mech} = 0.5\kappa$, they achieved a value of $\frac{S_{X_2}}{S_{X_1}} = 14 \pm 4.6$, close to that predicted by equation (3.35). In the result by Cinquegrana et al., a similar bridge circuit, incorporating a 380 g, 928 Hz mechanical resonator and 129.4 kHz electrical resonance, was measured at a temperature 4.2 K. The researchers were able to demonstrate that their system was sensitive to only a single quadrature of mechanical motion, and were able to distinguish the brownian motion of the mechanical resonance superimposed on the electrical resonance noise and not obscured by backaction-driven motion. A more recent attempt at backaction-evading measurement has been made by Caniard et al. [60] using two mechanically resonant mirrors mounted at each end of an optical cavity. Their scheme differs from the one discussed here in exploiting a difference in the two mirrors' resonance frequencies, meaning that at intermediate frequencies, the phase response of the two mirrors will be opposite. Because optical power circulating within the cavity exerts force in opposite directions on the two mirrors, radiation-pressure noise at the intermediate frequency will actually cause the two mirrors to move in unison, thus maintaining the cavity length. The researchers were able to demonstrate the backaction-evading behavior by injecting a noisy optical signal. This system, however, does not function as a single-quadrature detector of the mechanical motion, and because the BAE does not appear at either mechanical resonance frequency, the sensitivity to external forces is greatly reduced.

3.4.4 Quantum squeezed states of mechanical motion

Quantum squeezed states of an electromagnetic field have been extensively studied, both at optical [61] and at microwave [62] wavelengths. In both regimes, parametric amplification processes were used to generate fields having one quadrature with variance below the vacuum fluctuation level $\frac{1}{2}\hbar\omega$. Optical squeezed states have also been produced using parametric downconversion as well as four-wave mixing in optical fibers and atomic vapors. [63] The electromagnetic field of a resonant cavity behaves as a simple harmonic oscillator and serves as a model for applying the same concept to a mechanical system. The mechanical case has been the subject of theoretical study for more than twenty years. [64]

Because in the ideal case the X_1 quadrature is not subject to any backaction at all, the BAE technique holds the possibility of generating a squeezed state of mechanical motion, i.e. one in which the uncertainty in one quadrature is reduced below the zero-point motion. [20] [54] The uncertainty relation of the two quadratures given in equation (3.29) shows that at the minimum uncertainty condition, if each quadrature has equal uncertainty, we have $\Delta X_1 = \Delta X_2 = \Delta x_{ZP} = \sqrt{\frac{\hbar}{2m\omega_{NR}}}$. To suppress ΔX_1 below Δx_{ZP}, all that need be done is to increase the measurement strength by increasing the pump power (as described in section 3.6) until the additive uncertainty due to amplifier noise and noise in the SMR is reduced below Δx_{ZP}. Because the measurement is QND, backaction will add nothing to the uncertainty in X_1.

As Clerk et al. point out however (Ref. [20]), a measurement that is truly decoupled from X_1 is by nature unable to affect the intrinsic fluctuations in X_1 arising from its zero point and thermal motion. In averages over many measurements, these fluctuations would appear as extra uncertainty in the measured X_1 value. While the added uncertainty due to amplifier noise would be $< \Delta x_{ZP}$, the mechanical motion itself would be only “conditionally” squeezed. To enforce the squeezing of the motion, the authors propose to use the precision of the X_1 measurement in a feedback scheme that would actively damp the X_1 amplitude. An alternate proposal [65] would employ parametric amplification of the NR beyond the self-oscillation limit for short durations, in order to squeeze one quadrature below the zero point motion. This technique could be employed even if the average occupation of the mechanical mode is initially well above $\bar{n} = 1$, but a BAE type scheme would nonetheless be required to measure the resulting squeezed state. A number of other schemes have been proposed for generating quantum squeezed states of mechanical motion. [66] The demonstration of such states would be a dramatic demonstration of truly non-classical behavior, and backaction evading single-quadrature measurement is an important step towards this goal.

3.5 NR motion parametrically amplified in BAE pump configuration

3.5.1 Electrostatic frequency shift due to $\partial^2 C/\partial x^2$

Apart from the NR frequency shift imposed by optical-spring effects, we can identify a frequency shift due to electrostatic energy in the capacitance C_g coupling NR to SMR. [67], [68] In figure 2.4 we can see how the NR motion changes the gap in C_g. We assume that the equilibrium position of the NR is $x = 0$. The total energy stored in the capacitor is $\varepsilon_{NR} = \varepsilon_{mech} + \varepsilon_{electrostat}$, or

$$\varepsilon_{NR} = \frac{1}{2}kx^2 + \frac{1}{2}C_g V^2$$

Expanding C_g to 2nd order in x we have

$$\varepsilon_{NR} = \frac{1}{2}kx^2 + \frac{1}{2}V^2\left(C_{g,0} + \frac{\partial C_g}{\partial x}x + \frac{1}{2}\frac{\partial^2 C_g}{\partial x^2}x^2\right) \tag{3.36}$$

where $C_{g,0}$, $\frac{\partial C_g}{\partial x}$ and $\frac{\partial^2 C_g}{\partial x^2}$ are evaluated at $x = 0$. Since $C_{tot} = C + 2C_\kappa + C_g$ and C_g is the only varying term, and in practice $C \gg C_\kappa \gg C_g$, we can simplify the notation by replacing $\frac{\partial C_g}{\partial x}$ with $\frac{\partial C}{\partial x}$ and $\frac{\partial^2 C_g}{\partial x^2}$ with $\frac{\partial^2 C}{\partial x^2}$. Rearranging equation (3.36) we have

$$\varepsilon_{NR} = \frac{1}{2}C_{g,0}V^2 - \delta\varepsilon_{EM} + \frac{1}{2}(k + k_{EM})(x + \delta x_{EM})^2 \tag{3.37}$$

In practical application we can neglect the energy shift $\delta\varepsilon_{EM} = \frac{\frac{1}{2}\left(\frac{1}{2}\frac{\partial C}{\partial x}V^2\right)^2}{k+\frac{1}{2}\frac{\partial^2 C}{\partial x^2}V^2}$, and the shift in the equilibrium mechanical position $\delta x_{EM} = \frac{\frac{1}{2}\frac{\partial C}{\partial x}V^2}{k+\frac{1}{2}\frac{\partial^2 C}{\partial x^2}V^2}$. However, the "electrostatic spring constant" k_{EM} becomes important experimentally

$$k_{EM} = \frac{1}{2}\frac{\partial^2 C}{\partial x^2}V^2$$

The additional spring constant introduces a shift in the mechanical resonance frequency $\omega_{NR} = \sqrt{k_{tot}/m} = \sqrt{(k + k_{EM})/m}$. Taylor-expanding yields

$$\omega_{NR} = \omega_{NR,0}\left(1 + \frac{1}{2}\frac{k_{EM}}{k}\right) \tag{3.38}$$

Note that C_g scales roughly as $\frac{1}{d}$, where d is the gap between the NR and the nearby gate electrode. Therefore, $C_g \sim \frac{1}{d+x}$, meaning $\frac{\partial^2 C}{\partial x^2}$ will be negative. Increasing voltage will tend to *reduce* the resonance frequency of the NR.

For $V = V_{SMR}\cos(\omega_{pump}t)$, and $\omega_{pump} \gg \omega_{NR}$, the electrostatic spring constant will have a time-averaged value $\frac{1}{2}\frac{\partial^2 C}{\partial x^2} \cdot \frac{1}{2}V_{SMR}^2$. The NR is located at a voltage antinode within the SMR, having a standing-wave amplitude twice the wave amplitude given by equation (2.38); this is the same as the lumped-element model voltage of Eq. (2.26). We can use equation (2.30) to express k_{EM} in terms of the magnitude $\bar{n}_{SMR}$ of pump energy within the SMR.

$$k_{EM} = \frac{1}{2C}\frac{\partial^2 C}{\partial x^2} \cdot \bar{n}_{SMR}\hbar\omega_{pump} \tag{3.39}$$

In most practical cases in Eq. (3.39) we may approximate $\omega_{pump} = \omega_{SMR}$. We can define the parameter λ

$$\lambda = \frac{\omega_{SMR}}{2C}\frac{\partial^2 C}{\partial x^2} \tag{3.40}$$

Then the electrostatic spring constant may be expressed

$$k_{EM} = \lambda \cdot \hbar \bar{n}_{SMR} \tag{3.41}$$

The NR frequency shift in Eq. (3.41) may be seen when a single pump tone is applied. Another important condition is to apply two pump tones in the SMR for backaction evasion. Then the SMR voltage is:

$$\begin{aligned} V &= \frac{V_{SMR}}{2}\left(\cos((\omega_{SMR} - \omega_{NR})t) + \cos((\omega_{SMR} + \omega_{NR})t)\right) \\ &= V_{SMR}\cos(\omega_{SMR}t)\cos(\omega_{NR}t) \end{aligned}$$

Taking V^2 and time-averaging over a microwave cycle $\frac{1}{\omega_{SMR}}$, we have

$$\langle V^2 \rangle = \frac{1}{4}V_{SMR}^2(1 + \cos(2\omega_{NR}t))$$

Considering the SMR internal energy $\bar{n}_{SMR}\hbar\omega_{SMR}$ to be the sum of the energies due to the two pump tones (and approximating $\hbar(\omega_{SMR} - \omega_{NR}) = \hbar(\omega_{SMR} + \omega_{NR}) = \hbar\omega_{SMR}$) we have $\bar{n}_{SMR}\hbar\omega_{SMR} = 2 \cdot \frac{1}{2}C\left(\frac{V_{SMR}}{2}\right)^2$ and we can express

$$\langle V^2 \rangle = \frac{1}{C}\bar{n}_{SMR}\hbar\omega_{SMR}(1 + \cos(2\omega_{NR}t))$$

Then we can express $k_{EM} = \frac{1}{2}\frac{\partial^2 C}{\partial x^2}\langle V^2 \rangle$ and extend equation (3.39) to this double-pump case

$$\begin{aligned} k_{EM} &= \frac{1}{2C}\frac{\partial^2 C}{\partial x^2}\bar{n}_{SMR}\hbar\omega_{SMR}(1 + \cos(2\omega_{NR}t)) \\ &= \lambda \cdot \hbar\bar{n}_{SMR}(1 + \cos(2\omega_{NR}t)) \end{aligned} \tag{3.42}$$

Note that in the limiting case $\omega_{NR} = 0$, i.e. if we reduce to a single pump tone, equation (3.42) reduces to equation (3.41) (keeping in mind that $\bar{n}_{SMR}$ is defined slightly differently in equation (3.42) as the sum of two pump energies, whereas in (3.41) a single pump tone is assumed).

3.5.2 Parametric amplification of NR motion

Oscillation of the mechanical spring constant and therefore of the mechanical frequency is a condition for parametric amplification of the mechanical motion. As described by Rugar [69], this amplification is phase-dependent: it amplifies one quadrature by an amount $\frac{1}{1-Q_{NR}\frac{k_{EM}}{2k}}$ while the other is amplified by an amount $\frac{1}{1+Q_{NR}\frac{k_{EM}}{2k}}$, i.e. it amplifies one quadrature and deamplifies the other. Thus we can see from equation (3.38) that when the oscillating frequency shift $\left(\omega_{NR,0} \cdot \frac{1}{2}\frac{k_{EM}}{k}\right)$ is made $\geq \Gamma_{NR}$, the NR will self-oscillate uncontrollably.

Parametric amplification will amplify any motion of the NR and has the distinct benefit of doing so without adding noise. It has been shown to readily amplify the thermal motion of a mechanical resonator. [69] [70] The phase-dependent amplification means that while one quadrature's motion is increased, the other's is reduced in energy, that is, cooled. Such a behavior is referred to as "thermomechanical noise squeezing." [69]

However, further analysis comparing equations (3.38) and (3.42) with the single-quadrature detection described in section 3.4.3 indicates that the parametrically amplified and deamplified quadratures are *not* the X_1 and X_2 defined by the double pump tone, but are instead defined at a phase of $\frac{\pi}{2}$ relative to these. This poses a problem for backaction-evading measurement, because X_1 and X_2 are no longer independent. At sufficiently high levels of parametric amplification, X_1 will reflect both quadratures of motion equally, destroying the BAE completely. When not considering backaction, however, the parametrically-amplified quadrature will dominate over the deamplified one in the measurement, and thus we can treat the parametric amplification as an effective decrease $\left(\omega_{NR,0} \cdot \frac{1}{2}\frac{k_{EM}}{k}\right)$ in the linewidth Γ_{tot}, and associated amplification of the motion.

3.6 Position sensitivity

The Heisenberg uncertainty principle requires that the product of the uncertainties in position Δx and momentum Δp, be $\Delta x \Delta p \geq \frac{\hbar}{2}$. The minimum of this condition is satisfied when $\Delta x = \Delta x_{ZP} = \sqrt{\frac{\hbar}{2m\omega_m}}$ and $\Delta p = m\omega_m \Delta x_{ZP}$. Thus, to reach the SQL, the *total* uncertainty in position must be Δx_{ZP}. When reaching this limit, we expect the components of the noise spectral density S_x^{imp} due to additive noise and S_x^{BA} due to measurement backaction to be equal. For a (angular-frequency) linewidth Γ_m and position noise spectral density S_x the absolute position uncertainty due to this noise is $\Delta x = \sqrt{\frac{\Gamma_m}{4} S_x}$. (Note that we use throughout this work a convention of single-sided spectral densities.) Thus we have, at the standard quantum limit

$$\begin{aligned}\Delta x_{ZP} &= \sqrt{\frac{\Gamma_m}{4} S_x^{tot}} \\ &= \sqrt{\frac{\Gamma_m}{4} (S_x^{imp} + S_x^{BA})} \\ &= \sqrt{\frac{\Gamma_m}{4} \cdot 2 S_x^{imp}}\end{aligned}$$

Thus at the SQL we expect

$$S_x^{imp}(SQL) = \frac{\hbar}{m\omega_m \Gamma_m} \tag{3.43}$$

From a position noise S_x we can find an energy spectral density $S_N = m\omega_m^2 S_x$ and from this the total energy in the Lorentzian line $E = \frac{\Gamma_m}{4} S_N$. Thus at the SQL we can define an equivalent energy of the measurement imprecision

$$E^{imp}(SQL) = \frac{1}{4}\hbar\omega_m$$

Thus at the SQL, the imprecision noise raises the level of the measured amplitude by an amount equivalent to $\frac{1}{4}$ quantum of mechanical energy. Because we expect at the SQL for the backaction noise to equal the imprecision noise, the backaction will also add $\frac{1}{4}$ quantum of mechanical energy. Whereas the energy associated with imprecision noise adds only to the measured value, the backaction energy, however, is in fact added to the mechanical resonator itself: the mechanical amplitude is increased by backaction. Stronger coupling which further diminishes S_x^{imp} doesn't gain you anything, as it will only increase S_x^{BA}. For continuous position measurement, detection of this backaction represents the true signature of quantum-limited measurement: You can't measure the motion any more precisely, because the motion you're trying to measure is being *perturbed by the measurement* in a manner dictated by quantum mechanics.

There are two important things to note here. First, there is in principle no lower limit on S_x^{imp}. While the achievement of $S_x^{imp} = S_x^{imp}(SQL)$ is an important technological challenge and was an experimental goal in the work reported in this dissertation, it does not represent a fundamental lower limit on anything. As long as you continue to increase the coupling between the mechanical resonator and the detector, and don't add any extra noise to the system, this source of uncertainty continues to diminish. The second thing to note is that experimentally, S_x^{imp} is usually pretty easy to determine. It results from "additive noise", i.e. noise which is added to the measurement by the amplifier or other components of the system, but which does not drive the mechanical motion. Such noise is generally frequency-independent over a relatively broad band and can therefore be resolved accurately by averaging over a wide spectral span. Indeed, the fundamental lower limit possible for this additive noise is one quantum: one-half quantum of white noise at the measurement frequency, contributed each by vacuum fluctuations and by the amplifier, if the amplifier is quantum-limited. This lower limit of $\frac{1}{2}$ quantum of additive noise from the amplifier is derived formally by Caves [71].

The backaction noise S_x^{BA}, on the other hand, is typically very difficult to measure because it may be seen only in its effects on the mechanical motion. In most practical experiments, evidence of such backaction driving will appear as a very small change in the mechanical motion relative to the thermally-driven amplitude. An ideal measurement would employ a mechanical resonator in its ground state, but such a system remains yet out of reach. In practice in most experiments the thermal motion is orders of magnitude greater than the expected magnitude of quantum backaction. Moreover, in real systems the effects of thermal heating and other classical noise sources may mask and mimic the quantum backaction, making it even more difficult to distinguish. The magnitude of the backaction is a function of the coupling strength of the measurement (which we vary in our system by varying the pump power). Although in quantum mechanical terms S_x^{imp} and S_x^{BA} are related by the Heisenberg uncertainty principle (see section 6.8), the classical noise added after the measurement may raise or lower S_x^{imp} without affecting S_x^{BA}. Thus the measured S_x^{imp} may not be very useful in predicting quantum limits on S_x^{BA}. If one wants to use the Heisenberg relations to predict the level of S_x^{BA} due to quantum backaction, one must first estimate what the quantum-limited S_x^{imp} would be.

An interesting result reporting $S_x^{imp} < S_x^{imp}(SQL)$ is given by Teufel at al, in the research group led by K. Lehnert. [72] They reported the use of a prototype ultra-low-noise microwave amplifier to read out the position of a 1.04 MHz nanomechanical resonator coupled to a 7.49 GHz SMR. The amplifier is a Josephson parametric amplifier, which operates nonlinearly and may thus in principle surpass some of the quantum limits on linear amplifiers. Where a quantum-limited linear amplifier would add $\frac{1}{2}$ quantum of energy at the measurement frequency, and an ideal nonlinear amplifier is capable of adding zero quanta, this amplifier is reported to add only 1.3 quanta. Considering the unavoidable $\frac{1}{2}$ quantum of noise contributed by vacuum fluctuations of the microwave field, this makes their total added noise a factor of 3.6 above the shot noise limit. The readout scheme is very similar to that of the Lehnert group's earlier work (Ref. [17], discussed in section 2.4 of this dissertation), in which the SMR is driven on-resonance and its phase tracks the motion of the NR. For this very small level of added noise, the coupling strength that these researchers achieved between their SMR and NR was sufficient to suppress the position uncertainty S_x^{imp} below the level $S_x^{imp}(SQL)$, defined in Eq. (3.43). By applying a microwave power of $> 10^3$ pW to their SMR, they achieved $S_x = (0.80 \pm 0.03) S_x^{SQL}$. In other words, they achieved a position uncertainty due to additive noise that equaled $\sqrt{0.8} \cdot \frac{1}{\sqrt{2}} \Delta x_{ZP}$. Furthermore, by driving with a blue-detuned microwave pump, they suppressed the linewidth of their NR sufficiently to achieve $S_x = 0.07 S_x^{SQL}$. (This latter technique is analogous to the parametric amplification effect that we employed to improve our position sensitivity, as discussed in section 6.6, and similarly has the disadvantage of dramatically increasing the thermal amplitude of the mechanical motion.) With such a low position uncertainty, there should necessarily be quantum noise backaction driving the NR. For instance, Naik et al. observed quantum noise backaction (reference [3]) using the shot noise of a single-electron transistor, even though they did not achieve $S_x < S_x^{SQL}$. Indeed, for $S_x = 0.8 S_x^{SQL}$ and a total additive noise 3.6 times the shot noise limit, the backaction-driven position noise density should be $4.5 S_x^{SQL}$, corresponding to 1.1 added quanta of mechanical energy.

However, the device used by Teufel et al. would have great difficulty distinguishing this amount of additional mechanical amplitude, as the mechanical mode temperature is 130 mK, or 2600 quanta. Lehnert's research group has also reported elsewhere observing in similar SMR-NR devices evidence of strong classical backaction (most likely thermal heating) driving the NR for increasing pump powers ([17]). Here they report that the mechanical mode temperature increases with drive power and that the linewidth also increases from its initial value of $\Gamma_m = 2\pi \cdot 1.7$ Hz, strongly suggestive of thermal heating. Thus it appears very challenging to use their device to achieve true quantum-limited position measurement by detecting quantum backaction. The recent results with this device do not include any measurements of backaction driving the nanoresonator, or estimates of how much classical backaction is contributed by their ultra-low-noise amplifier and how much may be obscuring the quantum backaction. Furthermore, as their device had $\kappa = 2\pi \cdot 2.88$ MHz it operates in the bad-cavity limit and would be poorly adaptable to backaction evading measurements. (See section 3.4.3) Nonetheless, the results reported by Teufel et al. powerfully demonstrate the advantage of low-noise amplification in seeking quantum limited position measurement.

Calculating the position sensitivity due to additive noise is a matter of considering how the noise in the measurement mimics the way the actual motion appears in the measurement. Indeed the actual thermal motion of a mechanical resonator or the motion of a quantum state will after all appear in the measurement apparatus as just another noise signal; we can call the added noise a "position noise". In spectral terms this means that the noise contribution is just the additive white noise within the noise bandwith of the mechanical resonator. Alternatively it can be thought of as the ratio of noise background level to measured peak amplitude. [73] Thus at the standard quantum limit the position noise, averaged over one decay time of the NR, equals the zero-point motion of the resonator. [27]

Clearly the mechanical linewidth Γ_{tot} is critical to the measured position sensitivity and for a given level of noise, a longer mechanical decay time, i.e. narrower linewidth, allows us to more closely approach the SQL. While in many measurements the linewidth is fixed, $\Gamma_{tot} = \Gamma_{NR}$, in some cases it is dependent on the pump power, which is also the parameter which is increased in order to increase the position sensitivity. The position sensitivity of an NR measured while undergoing backaction-cooling (section 3.1.3) is an interesting case. For motion measured using a single red-detuned pump, the increase in optical damping with increasing pump power leads to a rolloff and saturation in the position sensitivity. This situation may be analyzed following conventions presented by Braginsky and others [55], and assuming the sideband-resolved limit and that the SMR is pumped at $\omega_{SMR} - \omega_{NR}$. [74] For the ideal case of a dissipationless SMR in the ideal good-cavity limit, with no losses between SMR and amplifier, the limiting-value of the position uncertainty is given by

$$\Delta x = \sqrt{\bar{n}_{amp} + \bar{n}_{vac}} \cdot \Delta x_{ZP}$$

where $\bar{n}_{amp}$ is the additive amplifier noise, expressed as a number of SMR quanta, and $\bar{n}_{vac}$ is the noise due to vacuum fluctuations. Because the lowest possible n_{amp} equals $\frac{1}{2}$ for a quantum-limited linear amplifier, and n_{vac} is at least $\frac{1}{2}$, the position sensitivity attained using a single red pump reaches the standard quantum limit only in the ideal case in the limit of high pump power, i.e. strong coupling. This conclusion accords with our other discussions of backaction cooling (section 3.1.3) in regard to its backaction temperature proportional to $\bar{n}_{NR}^{opt}$. In the good-cavity limit,

$\bar{n}_{NR}^{opt} = 0$. In other words, when applying a single red pump in a sideband-resolved device, the quantum back-action corresponds to a near-zero-temperature bath and will not drive the NR no matter how high the pump power. [73] We will demonstrate some of this kind of behavior in section 6.2.

Chapter 4

Fabrication, Setup and Apparatus

4.1 Fridge setup and internal wiring

In order to approach the goal of placing the mechanical resonator into its quantum ground state, it is necessary to work at very low temperatures. Furthermore, the need for a very high-Q microwave resonator requires operating well below the superconducting transition temperature of aluminum, $T_c = 1.14$ K. Moreover, to prevent the SMR from being thermally excited, we should operate at a temperature well below the energy of one microwave quantum at 5 GHz, $\hbar\omega_{SMR}/k_B = 240$ mK. We meet all of these requirements by using an Oxford Kelvinox 400 dilution refrigerator, capable of a base temperature below 10 mK. The refrigerator is mounted to an optical table supported on sand-filled concrete pillars. For operation, a counterweighted helium dewar is raised from below by a winch and bolted to the table. Low-temperature thermometry is provided by calibrated RuO resistance thermometers supplied by Oxford and reliable down to 20 mK. An AVS-47B resistance bridge and TS-530A temperature controller (Picowatt Inc) read the thermometers and provide temperature control to a heater at the mixing chamber stage.

Measurement wiring for microwave signals within the fridge employs coaxial cables and additional inline components to meet several requirements: 1) Present a continuous 50 ohm line impedance to the signals, attenuating the signal only where needed for control of thermal noise. 2) Offer minimal thermal conductance between fridge stages so as not to add extra heat loads to the fridge. 3) Be well thermalized to the fridge (particularly the inner conductor of the coaxial cable) so as not to heat the sample. 4) Block or attenuate Johnson noise emitted by dissipative components at room temperature or lower temperatures. Any lossy component or section of cable at temperature T will radiate as blackbody radiation a white noise density equal to $k_B T$ down the signal lines, which is liable to excite the SMR or thermally heat it. 5) Shield against interference by signals that could drive the SMR or NR resonances. Additional wiring for low-frequency signals must meet all these needs except for a less strict need for impedance matching. The low frequency signals reach the sample by coupling into the RF lines via a bias tee thermalized at the mixing chamber stage.

Detailed solutions to these issues have been discussed elsewhere in e.g. the Ph.D. dissertation by LaHaye [75]. In developing our experiments we went through several iterations of fridge wiring. For instance, when initially prototyping SMRs we added several coax lines to enable measuring multiple devices at once, but we later removed these because they added too much heat load to the fridge. Here we describe the wiring configuration used to perform the backaction cooling and evasion measurements reported in chapters 5 and 6. A wiring diagram appears in fig 4.1 and an annotated photograph appears in fig 4.2. Wiring variations used in earlier prototyping will be noted in other chapters where needed.

Within the fridge are three signal lines: a microwave drive line, a microwave return line and a low-frequency drive line. On the drive line, microwave frequency

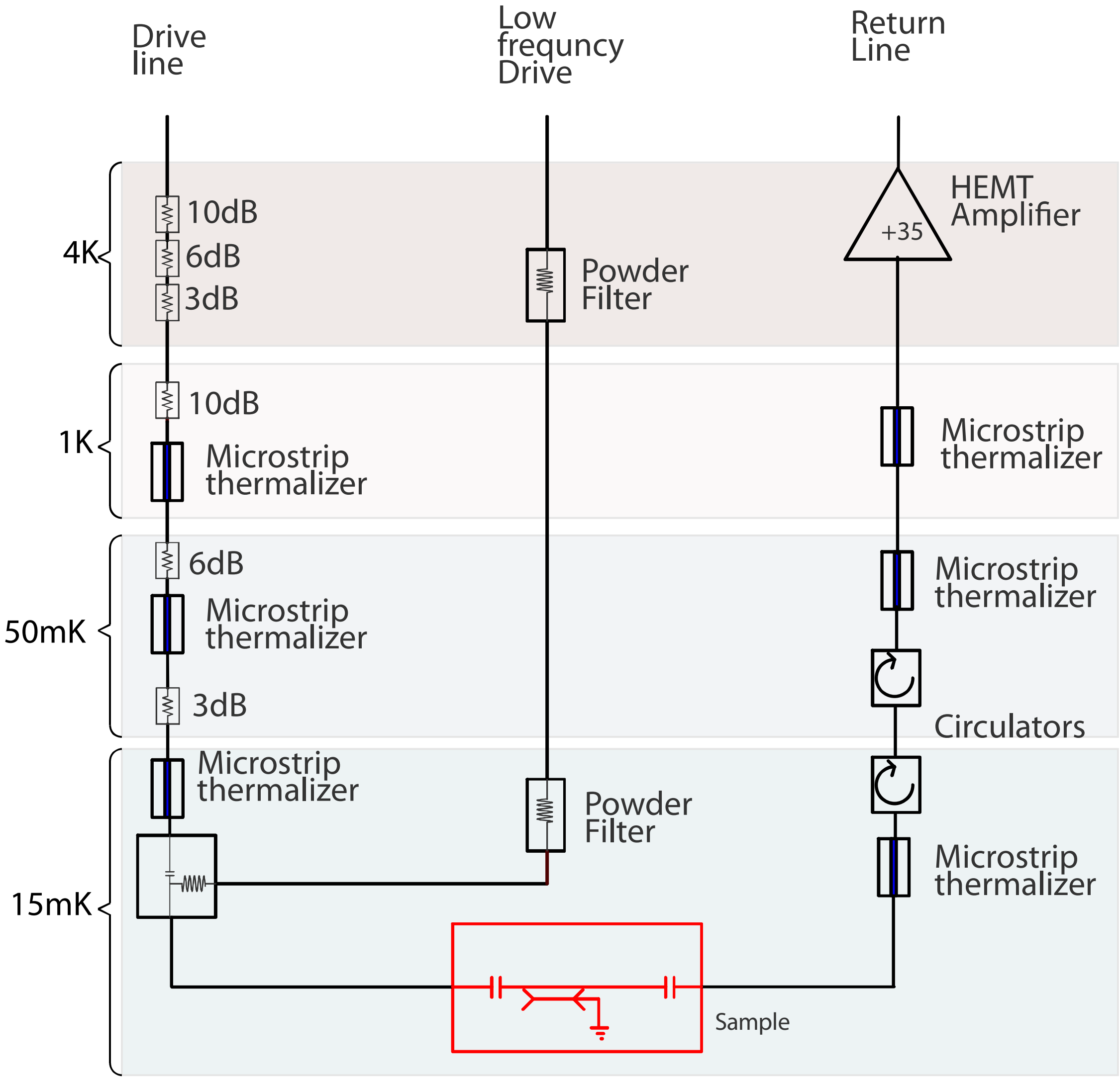

Figure 4.1: Schematic of interior wiring within dilution fridge. (Diagram prepared by T. Rocheleau.)

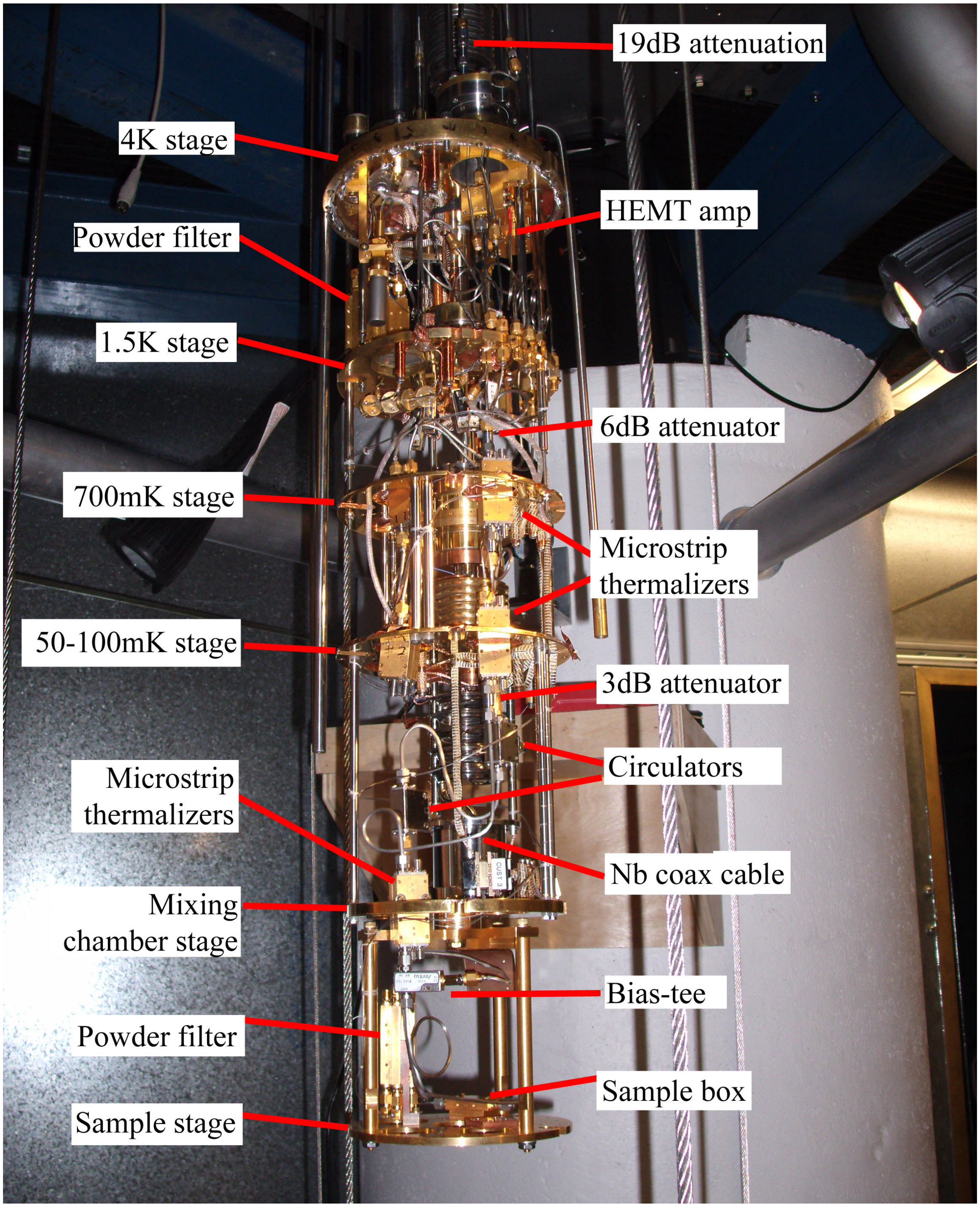

Figure 4.2: Photograph of Kelvinox 400 dilution fridge with vacuum can removed, showing internal wiring. Some components indicated in figure 4.1 are hidden in this photo.

blackbody radiation is suppressed using cold NiCr attenuators (Midwest Microwave) mounted at successive temperature stages, each of a magnitude to attenuate the Johnson noise emitted from the preceding stage. Microwave signal lines between 300K and 4K are Au-plated, CuNi-inner, CuNi-outer, 50 Ω semirigid 0.085" diameter coax cables (Coax Co, Ltd, Japan), which provide similar low thermal conductivity but better microwave transmission as compared to stainless-steel coaxial cable used elsewhere. [75] On the drive line at stages below 100 mK, and on the return line between the mixing stage and 1.5 K, microwave signals are carried by Nb-inner, Nb-outer 50 Ω semi-rigid 0.085" coax cables. On both drive and return lines, segments of 50 Ω superconducting Al microstrip on silicon serve to thermalize the inner conductor of the microwave lines at successive temperature stages. A detailed discussion of this kind of thermalizer appears in the PhD dissertation by M. LaHaye. [75] T. Rocheleau designed and installed the microstrip thermalizers used here.

On the return line, measured signals are amplified by a cryogenic HEMT amplifier (CITCRYO1-12A, S. Weinreb, Caltech). The builders of this amplifier tested it before delivery and found a noise temperature of 3.56 ± 1 K and gain of 37 dB at 5 GHz. As discussed in section 5.4, we will use this noise temperature to calibrate our signal lines in-situ. This amplifier is anchored to 4K and is isolated from the sample by two cryogenic circulators (Quinstar QCY-050100CM0). Two circulators in series were found to be necessary to prevent the 3.56 K noise radiating from the input of the amplifier from exciting the SMR above its ground state. We verified this in situ when the fridge was cold, by applying no pump power and observing the emitted spectrum in a range $\omega_{SMR} \pm \kappa$. After averaging the output signal for a duration sufficient to resolve an emitted power corresponding to less than 1 quantum stored in the SMR, we observed no resonance, and from this we conclude that the amplifier noise did not excite the SMR above its ground state.

Considering equations (2.35), (2.33) and (2.53), it is clear that a precise knowledge of the parameters $loss$ and $gain$ are necessary to know the signal levels within the SMR and to compare the results accurately to theory. While the gains and losses in wiring external to the fridge could be readily measured, the losses internal to the fridge are difficult to ascertain because they vary between room temperature and low temperatures. Most significantly, the microstrip thermalizers suffer from excess dissipation at room temperature due to free charge in the Si substrates, and are fully functional only at temperatures below 1 K where the Al is superconducting. (Our estimates of their behavior rely on measurements made at 4 K, where the substrate dissipation is eliminated by freeze-out of the substrate charge.) Nonetheless, based on measurements of the various components at room temperature and at 4 K, we estimated $loss$ at 5 GHz to be 48.5 dB from the top of the fridge to the sample and $gain$ at 5 GHz to be 51 dB from the sample to the measurement point in the control room. The uncertainties in each of these values are at least 3 dB, which motivated us to calibrate our signal levels in situ, based on equipartition and on the HEMT noise temperature. (See sections 5.5 and 5.4.)

It is important that the HEMT gain (37 dB) is great enough that the noise emitted by the HEMT (3.56 K, amplified 37 dB) will dominate the input noise of the room temperature amplifier (Miteq AFS3-04700530-07-8P-4-GW, noise figure

0.63 at 5 GHz, see section 4.2) even after approximately 5 dB attenuation in the coax cable between the HEMT amp and the top of the fridge. The additional 27.7 dB gain added by the room temperature amplifier enabled our measurement to remain limited by the HEMT amplifier noise despite further attenuation between this amplifier and the control room. We verified this by comparing the input noise of our spectrum analyzer to the noise from the sample; when monitoring the sample, the observed noise floor was ~ -142dBm/Hz while the spectrum analyzer noise floor was ~ -154dBm/Hz. It is also important to estimate the loss between the sample and the HEMT amp, because this cannot be determined in situ from RF measurement. From measurements of the microstrip thermalizers and circulators at 4 K, we estimate this loss to be 1.5 ± 1 dB.

The low-frequency signal line is intended to carry < 10 MHz signals for direct driving of the NR. This wiring is CuNi-inner, CuNi-outer 0.012” diameter cable (Coax Co, Ltd, Japan) and attenuates the signal by a total of about 18 dB at 5.5 MHz. At the mixing stage, a bias-tee (Anritsu K252) couples this signal into the RF line. On this line, Cu powder filters at the 1.5 K and mixing stages suppress all higher frequencies. Design and performance of this type of powder filter is described in the PhD dissertation by M. LaHaye. [75]

Studies in the literature have demonstrated that SMRs will exhibit excess internal dissipation due to magnetic flux trapped in the superconducting film. Early measurements of our prototype SMRs exhibited excess dissipation. We surmised that the ambient magnetic field of several gauss in the room where the fridge was located (due to magnetic materials in the concrete pillars and supporting structure) may have contributed to this. To eliminate this potential problem, we installed a Cryoperm magnetic shield can which bolted to the 50 mK stage of the fridge in place of the radiation shield can supplied by Oxford. This shield, which has a magnetic permeability optimized for low temperatures, enclosed all components beneath that stage. In addition, we wrapped two sheets of 0.010" thick Mu-Metal shielding around the fridge vacuum can. While we did not measure the resulting field in situ (which would require a magnetometer on the sample stage that could be read during fridge operation), we estimate based on vendor specifications that the shield reduced the field at the sample stage to tens of milligauss.

4.2 Wiring external to fridge

In all of these experiments, great care was taken to limit spurious signals and interference. The dilution fridge and instrumentation were installed in a shielded room. RF signal lines into and out of the shielded room were routed through DC-block filters. Due to limitations of cable attenuations, we operated the two Agilent microwave sources and one SR844 lock-in inside the shielded room; all others were placed outside. All other electronics was located in a separate control room. Photographs illustrating the inside of the shielded room and control room appear in figure 4.3. Every microwave pump signal passed through DC-block filters before entering the fridge. All instrumentation amplifiers within the shielded room were powered from batteries. Circuitry for voltage regulation of the battery power supplies was designed and installed by T. Rocheleau.

While wiring within the fridge is fixed during the experiment, the wiring outside the fridge was reconfigured for the several different kinds of measurements. Figures 4.4 and 4.5 illustrate the wiring configurations needed for the two primary types of measurement described in this work. Several other variants were needed for other measurements such as driven response of the NR. A photograph of a portion of the wiring appears in figure 4.6. Further variations were also employed in earlier prototyping of SMR-NR devices. For instance, when studying SMRs that operated in the "bad cavity" regime $\omega_{NR} \lesssim \kappa$, we found that the SMR transmitted enough of the pump signal (see e.g. equation (2.35)) to overload the low-noise room-temperature amplifier. To prevent this, a portion of the pump power was split from the source, phase-shifted to cancel the undesired signal and injected at the amp input. This kind of wiring change sometimes had to be done on-the-fly during measurements. Details of particular variants are described as necessary in other chapters.

Referring to figures 4.4 and 4.5, the microwave sources used for pump signals were of type Agilent E8257D, which has a maxiumum output of 25 dBm; when a third source was needed, we used a Rohde and Schwarz SMA100A, capable of 18 dBm maximum power. For 5 to 10 MHz driving signals on the low-frequency line, we used a Tektronix AFG3252. Lock-in amplifiers were of type Stanford SR844, and the spectrum analyzer was an Agilent N9020A. All sources and measurement devices were synchronized to the 10MHz signal of a SRS FS725 rubidium frequency standard.

The power-splitters are Pasternack model PE2028; directional couplers are

Figure 4.3: **(Left)** Photograph inside shielded room showing power supply rack on left and rack containing RF sources and lock-in on right. **(Right)** Photograph in control room. Fridge valve panel is on left. Spectrum analyzer is in lower middle of rack on right.

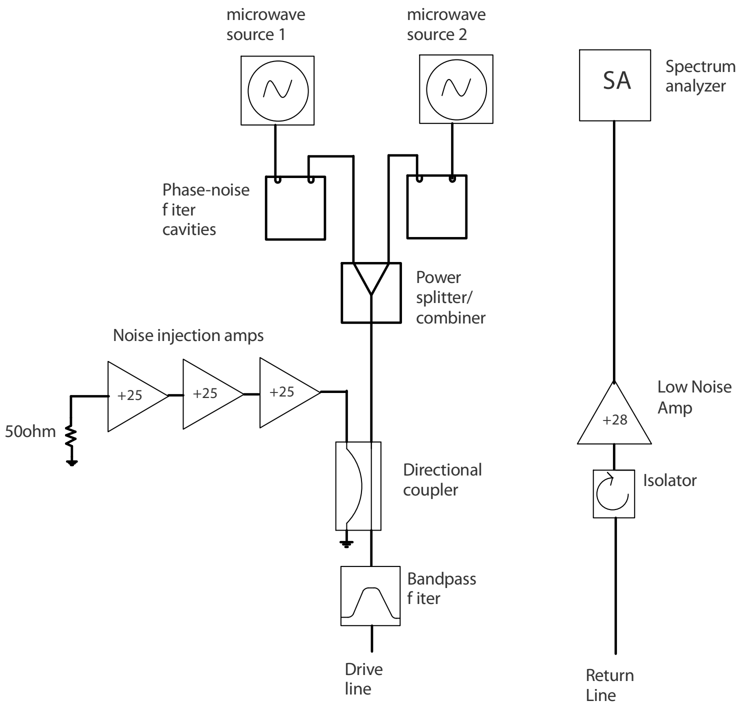

Figure 4.4: Schematic for BAE demonstration or backaction cooling. During cooling, either noise-injecting amplifiers were shut off, or the entire subcircuit containing directional coupler and noise-injecting amplifiers was removed. Drive and return lines join to corresponding points on fridge. (Diagram prepared by T. Rocheleau.)

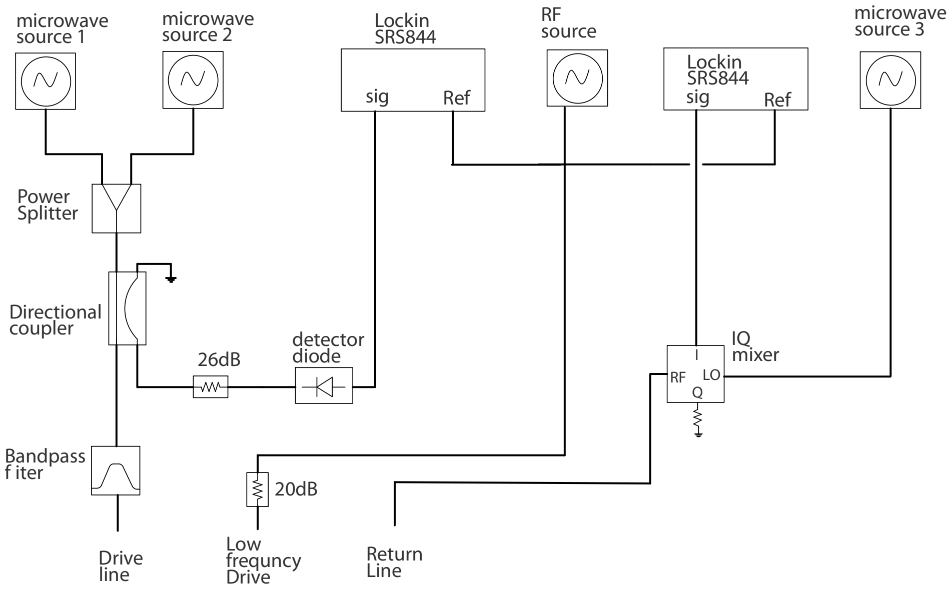

Figure 4.5: Schematic for demonstrating single-quadrature detection of driven NR. Signal lines join to corresponding points on fridge. (Diagram prepared by T. Rocheleau.)

Pasternack model PE-2204-10 and PE-2210-20. The room temperature low noise amplifier is a Miteq AFS3-04700530-07-8P-4-GW. The bandpass filter is a Minicircuits VBFZ-5500. The IQ mixer is a Marki Microwave IQ0307LXP; in some wiring configurations this was replaced by a non-IQ-type mixer, Marki TL30007LA. To inject broadband microwave noise for backaction evasion measurements (figure 4.4, and section 6.5) we used two Quinstar OLJ-04122025-J0 amplifiers in series with a Miteq LCA-0408. The room temperature circulator is a Ditom D3C-4080 and the diode detector used for tracking the phase of the double microwave pump signal in BAE measurements (section 6.5.1) was an Eclipse DT4752A3. We used SMA-terminated MiniCircuits type CBL-6FT-SMSM+ signal cables (in various lengths from 3 to 6 ft), which proved far superior to other types in suppressing crosstalk of

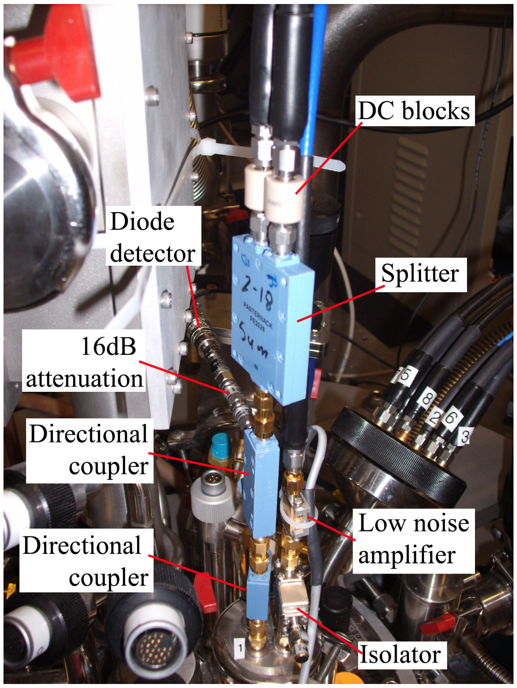

Figure 4.6: Representative photograph of microwave components connected at top of fridge. For scale, the splitter is about 1.5 in wide. (The wiring configuration is slightly different than those shown in figures 4.4 and 4.5 and was used in measurements not discussed in this dissertation.)

signals. One practice we tried to maintain was to not disconnect and reconnect the circuit too often, as the transmission through the connection points could change very slightly each time. This could be a particular problem with some of the gold-plated connectors. On repeated use the plating could flake off and become lodged between the pin and shield of the connector, partially shorting the connector and adding up to a dB of loss! Stainless-steel connectors proved to be more reliable in this regard.

4.3 Device fabrication

Our fabrication technique builds on procedures our group had developed in past years. Devices are made on silicon-nitride (SiN)-coated silicon chips. The NR is formed of a doubly-clamped SiN beam covered by an aluminum film; the nitride acts as the structural element while the aluminum serves as both an electrode and an etch mask. The mechanical structure is defined by electron-beam lithography and freed by undercutting with a dry etch rather than a wet etch, thus avoiding the stresses of a liquid dip on these delicate structures. The development of the fabrication procedure is documented extensively in Ph.D. dissertations by Naik [41] and Truitt [76].

In this recent work, we adapted the procedure to couple the NR to an aluminum superconducting microwave resonator rather than a single-electron transistor as in earlier work. This made for simpler and more versatile fabrication since the SMR can be defined entirely by photolithography. We also adapted the procedure to use high-stress silicon nitride rather than low-stress nitride as in earlier devices, to exploit the very low dissipations demonstrated by Verbridge et al. in high-stress nitride resonators [77]. However, early prototype trials indicated that chips coated with high-stress nitride exhibited unusually high dissipation at microwave frequencies. The amount of dissipation exceeded by at least a factor of 100 the published values of dissipation in nitride [11], and remains unexplained. To counter this, we adapted the procedure to remove nearly all of the nitride from the chip except in the NR itself. These developments required several iterations. The chip size was

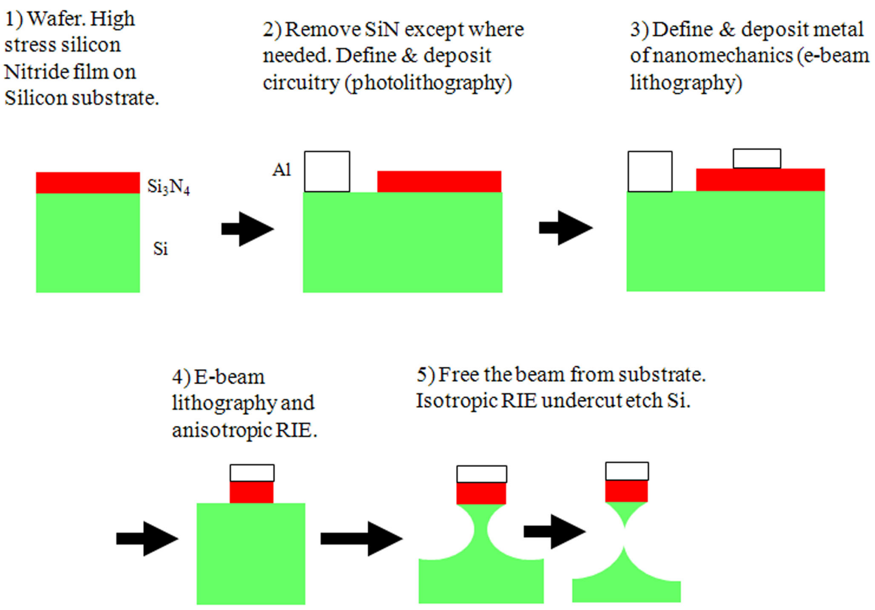

Figure 4.7: Schematic cross-section view of device fabrication.

also revised during the prototyping process, which accompanied a revision in sample box design and will be discussed below in section 4.4. I will present here the final procedure (shown schematically in figure 4.7) that we used to form the device employed for the measurements in chapters 5 and 6.

All fabrication was performed at the Cornell Nanoscale Fabrication facility, except for some of the aluminum deposition, which was done in a dedicated Al deposition chamber maintained by the Schwab group. T. Ndukum did the majority of the device design and fabrication, and in particular all of the e-beam lithography.

1. Substrates are 100 mm dia, ultra-high resistivity Si wafers: <100> orientation, 500 micrometers thick, with resistivity $>$ 10 kΩ·cm.

2. Low pressure chemical vapor deposition (LPCVD) of 70nm of high-stress SiN,

which will form the structural material of the NR.

3. Using photolithography and plasma etch, place alignment markers on the wafer to define the 3.5mm × 10mm die pattern.

4. Photolithographically define two 2 micron × 37 micron "patches" where the nano-resonators are to be located on each chip. Photoresist covers the patches; the rest of the wafer is exposed.

5. Strip the nitride in all exposed regions, using plasma etching (150W, 60mTorr, 50sccm CHF_3/5 sccm O_2) followed by a smoothing buffered oxide (BOE, 6:1) wet etch. The latter etches the nitride at ∼5-10Å/min but does not attack the underlying Si.

6. Photolithographically define the SMR followed by thermal evaporation deposition and lift-off of 260 nm of thermally evaporated (99.999% pure) Al.

7. Define the NR on top of the SiN patches using double-layer PMMA resist, electron beam lithography, electron-beam evaporation of 105 nm of Al and lift-off.

8. Dice the wafer into individual chips. Chips should be diced precisely with a narrow (< 50 micron wide) dicing blade to permit a tight fit into the sample box, minimizing the gaps that must be bridged for RF conduction.

9. Using e-beam lithography, define an "etch window" for plasma etch to free the NR. This window defines the length of the doubly-clamped beam.

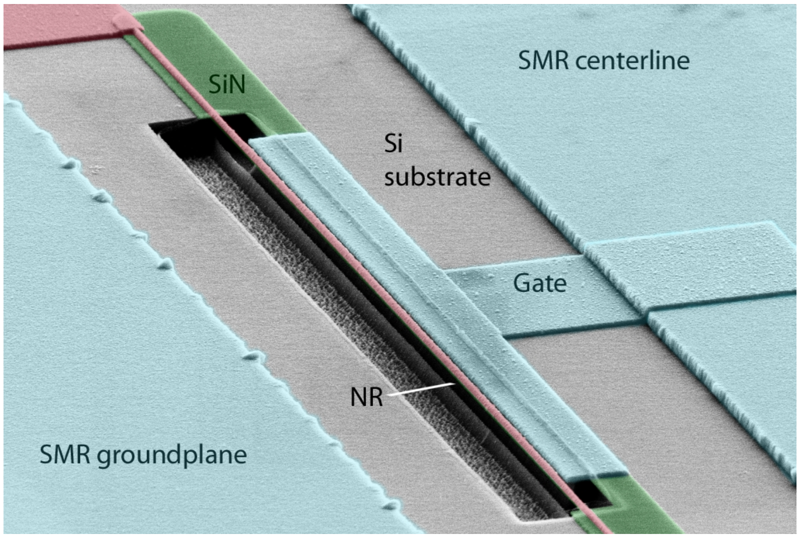

Figure 4.8: False-colored SEM microphotograph. NR coupled to centerline and groundplane of coplanar waveguide in SMR.

10. Plasma etch (150W, 60mTorr, 50sccm CHF_3/5 sccm O_2) to vertically etch the SiN.
11. Without removing the chip from the etch chamber, plasma etch (100W, 125mTorr, 50 sccm SF_6) to isotropically remove the silicon underneath the NR
12. Oxygen plasma clean to remove residual e-beam resist.

Figure 2.1 shows a full completed chip and figure 4.8 shows a false-color angle-view SEM image of the NR. The final NR consists of a 60 nm-thick SiN layer coated with 105 nm of Al. The 85 micron gap between NR and gate electrode may be more clearly seen in figure 4.9. Dimensions of the device were verified by high-magnification SEM inspection.

To offer redundancy and the possibility of more measurements per cooldown,

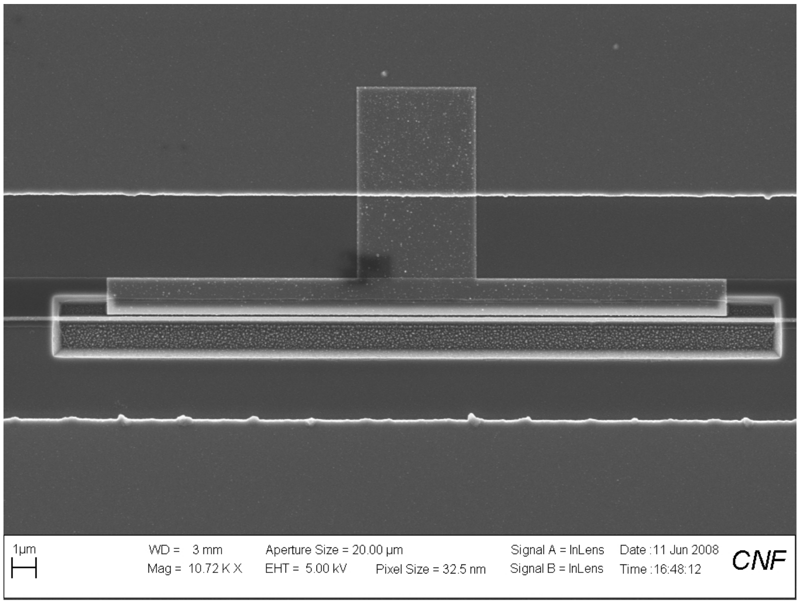

Figure 4.9: Top-view SEM microphotograph of NR and gate more clearly showing ~85 nm gap between them.

two nanoresonators were fabricated onto each chip, both coupled to the SMR. The lengths of the two NRs were made different to produce different resonance frequencies. In practice, on cooling down the sample, we usually found that one NR would be more easily-measurable than the other because its coupling was better or the other one had broken in handling, and only the intact well-coupled NR was studied.

As discussed in section 3.1.4, making the gate capacitance C_g large is critical to high-precision detection of the motion or to backaction cooling. In practice, this means reducing the gap d between NR and gate. The lower practical limit on d for these devices is about 60 nm. Smaller gaps are difficult to define reliably by our e-beam lithography and lift-off process, and even when they can be made the NR has a tendency to snap to the gate. Shorter beams, having higher spring

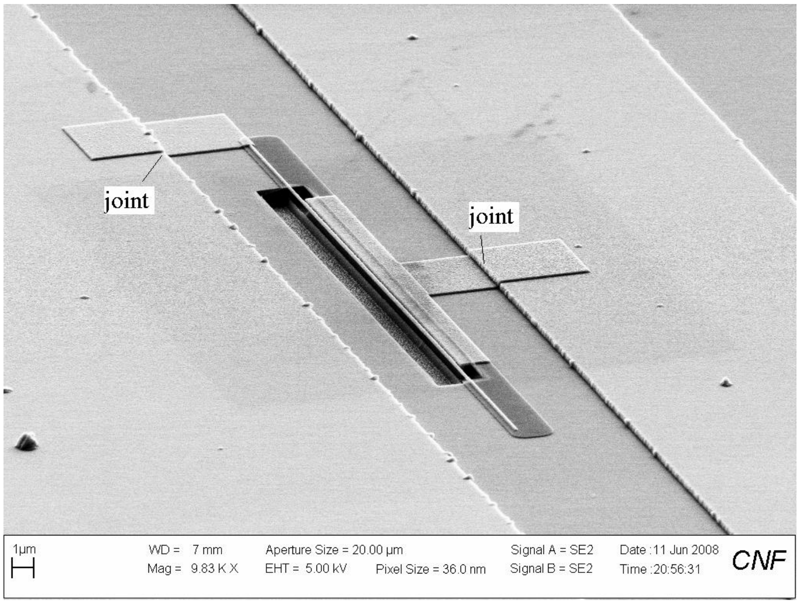

Figure 4.10: SEM microphotograph indicating joints between SMR and NR.

constant, will be less likely to snap. Another challenge concerning C_g is that the aluminum layers forming the SMR and NR are deposited in two separate steps, and the first aluminum surface oxidizes in air in the meantime, thus the contact points between the two layers can be a problem, indicated in figure 4.10. The NR aluminum is only half as thick as the SMR aluminum, but is deposited afterward, meaning that the contact area may be limited to a narrow insulating joint where the SMR centerline meets the gate material and another where the NR material meets the groundplane. If these joints act as capacitors of order $\sim C_g$, they would capacitively divide the gate capacitance, thus reducing the effective coupling of SMR to NR. The capacitance of these structures is difficult to calculate precisely, but our evidence from RF measurements of the device behavior suggests that this does indeed happen. (See section 6.2.) Fabrication of future devices should avoid

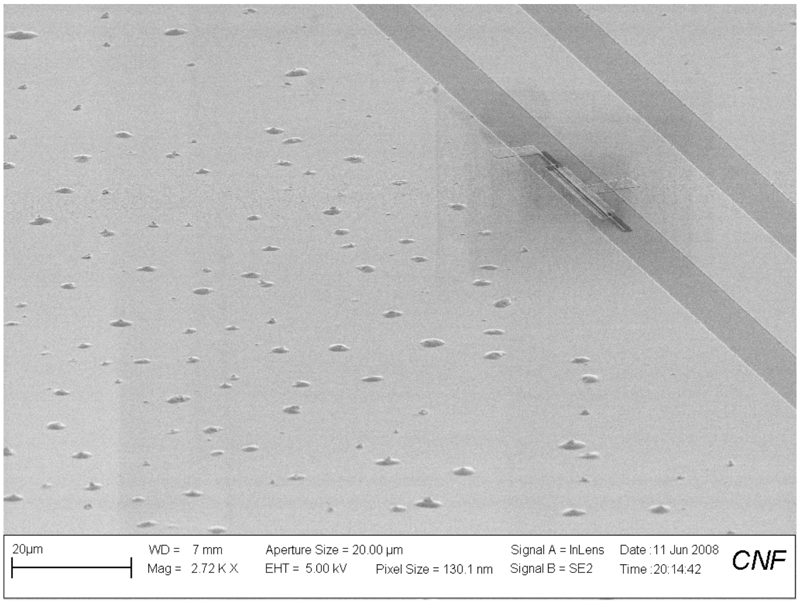

Figure 4.11: SEM microphotograph showing damage to Al film.

this issue by depositing the NR material prior to the SMR material, or some other way.

Another possible problem concerns the quality of the Al film in the SMR. We would like the SMR to carry as high a current as possible without dissipation; impurities in the Al could potentially reduce the superconducting critical current. Magnetic impurities are a particular concern, which motivated us to deposit the SMR material in a thermal evaporation chamber dedicated only to Al and having a base pressure of $\sim 5 \cdot 10^{-8}$ torr. However, other problems may arise in the fabrication. Figure 4.11 shows damage that occurred to the film probably owing to organic contaminants left on the wafer surface before SMR Al deposition, which later outgassed when the device was heated in the plasma etch. This device was used for the measurements reported in this dissertation; the impact of the damage is not known, but it may possibly account for the poor microwave power handling seen in this device.

We design the characteristic impedance of the CPW that forms our SMR to be $Z_0' = 50$ ohms. Because we know the substrate dielectric constant and our photolithography can reproduce features to better than a micron, by following the designs described in section 2.3 we expect our device's waveguide to closely match this design. More difficult to design precisely are the end-coupling capacitors of the SMR, C_κ, which are made as interdigitated capacitors shown in figure 2.5. The capacitance may be estimated from the geometry, and governs the coupling κ_{ext} of the SMR to the input and output transmission lines as per Eq. (2.25). We would like for $\kappa_{int} \ll \kappa_{ext}$, but the internal loss κ_{int} depends on dissipation in the aluminum and the substrate (see equation (2.23)) which is not always easy to control. In this device we designed C_κ to be 3.0 fF, which would make $\kappa_{ext} = 2\pi \cdot 141\text{kHz}$, or $Q_{ext} = 3.5 \cdot 10^4$. In section 5.4 we compare these estimates to values derived from RF measurements of the device.

4.4 Sample boxes

Proper mounting of the sample is critical to making a precise measurement. The sample package should transfer all the microwave input power and output signal to and from the on-chip waveguide without losses or impedance mismatches, and without exciting microwave modes that bypass the SMR. Figures 4.12 and 4.13 show the 3.5mm × 10mm × 500 micron sample chip mounted in our sample box.

To minimize impedance mismatches, the coplanar waveguide on the circuit board is designed to have a .016” wide centerline, closely matching the .010” pin size of the SMA connectors to which it is soldered. The circuit board is designed to match as closely as possible to the thickness and dielectric constant of the silicon chip, so that the microwaves travel as nearly as possible along an unbroken waveguide with no step changes. The board is made of Arlon AR1000 material, designed to have low dielectric losses at microwave frequencies, 0.015” thick, $\epsilon = 9.7$, with 1/2 oz/in Cu cladding on each side, subsequently gold-plated by the board fabrication vendor as protection against tarnishing. The waveguide centerline also matches the centerline of the lead-in portion of waveguide at each end of the chip. At these dimensions, the waveguide is a hybrid between pure CPW and microstrip, and the dimensions were calculated using “TXline” software to produce 50 ohm characteristic impedance (assuming the manufacturer’s values of the substrate dielectric constant). Throughout the groundplane, 0.014” dia “via” holes, spaced 0.04” apart, short the top surface of the circuit board to the grounded sample box. The box itself (designed by T. Rocheleau) is made of OFHC copper, gold-plated. The chip fits snugly into a hole in the circuit board and is held firmly against the gold-plated sample box surface by two clips. (To remove the chip, it must be forced out from underneath by a screw.) To ensure proper grounding of the SMR groundplane, a large number of Al wirebonds are used to connect the Al groundplane of the chip to the groundplane of the circuit board as well as to connect the two halves of the chip groundplane. It is important to bond each end of the chip centerline and groundplane to the circuit board centerline and groundplane with several short bonds, so that the microwaves

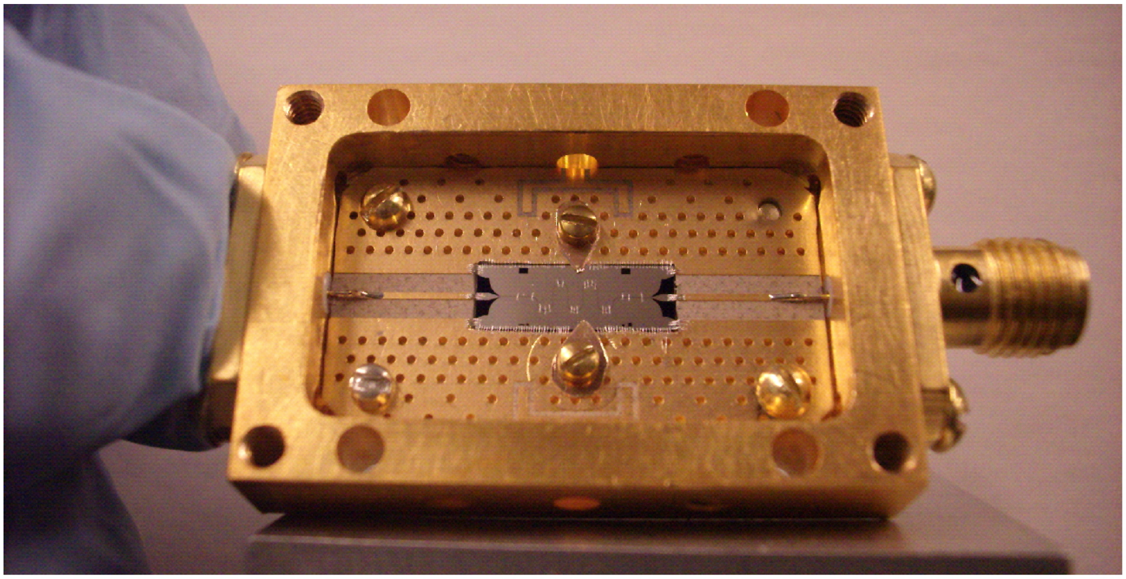

Figure 4.12: Chip in gold-plated copper sample box. SMA coaxial connector at each end is soldered to coplanar waveguide on circuit board to transmit signals to/from the chip. Gloved fingers holding box provide scale.

are launched properly from board to chip and vice versa.

Both box and circuit board are plated with ∼100 nm of gold as a protection against tarnishing, to enable reliable thermal contacts and wire bonding. While it is a standard practice to underlay gold plating with several microns of nickel plating, in our case we omit the nickel, to avoid the presence of magnetic material near the superconductor. Slow diffusion of the copper into the gold is expected to gradually degrade the gold film. However, studies in the literature [78] indicate that at room temperature a 100 nm Au layer should hold up for at least two years against grain-boundary diffusion of Cu.

We revised the sample box design twice before arriving at a satisfactory de-

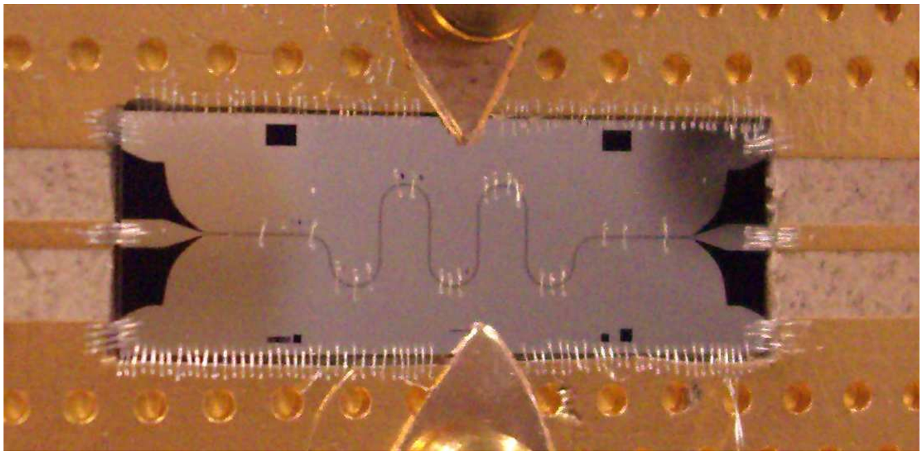

Figure 4.13: Close-up photo of chip in sample box showing wirebonds.

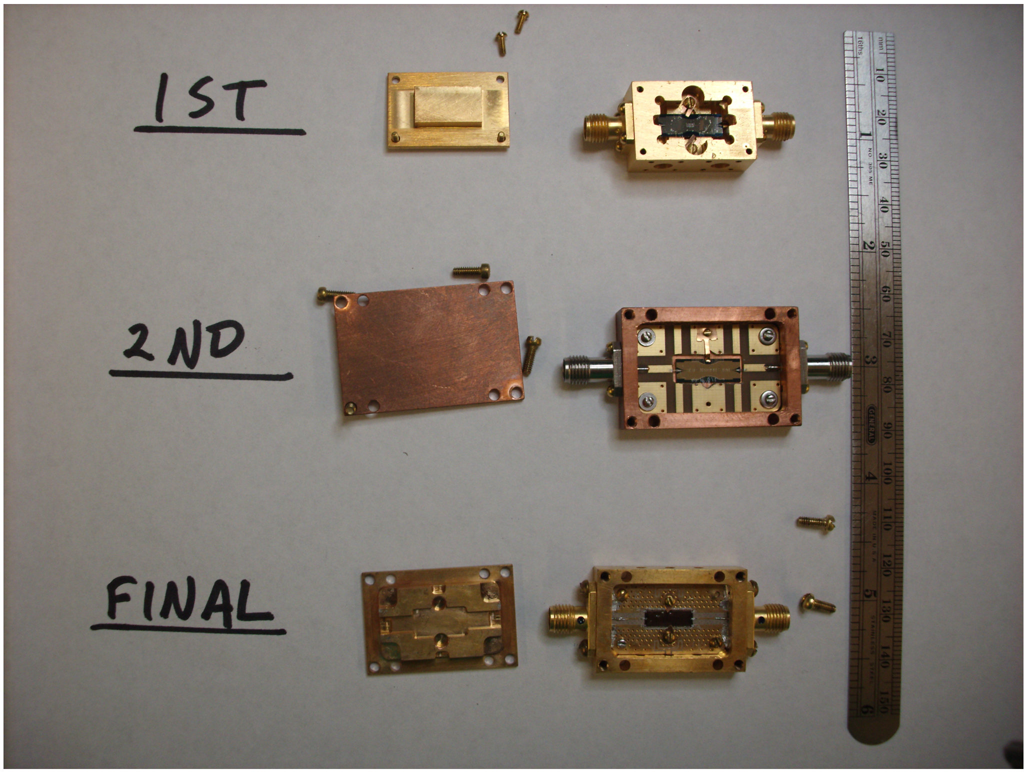

Figure 4.14: Photograph comparing three sample box designs. Note smaller chip size and "mode filling" lid in final design.

sign. Figure 4.14 shows the three designs. The first two types permitted too much microwave power to bypass the SMR, as shown in figure 4.15. The first type was designed with interior dimensions as small as possible to suppress free-space microwave modes, and designed without a circuit board to avoid modes propagating through the board. In this design the chip was wirebonded directly to the gold-plated copper sample box and to the center pin of the SMA connector. However, this was not successful because it was difficult to make enough bonds for a good RF connection. The large size (5×14 mm) of the chip designed for this box may also enable transmission through modes in its groundplane. A second design incorporated a circuit board which could be more readily bonded to the chip, but its groundplane was not sufficiently well-grounded with vias and the waveguide on the board was not well matched to the chip. The interior of this box was also large enough to permit propagating waveguide modes as low as 8 GHz. The final design (described earlier in this section) remedied these problems. It was also designed with a "mode filling" lid, that presses firmly against the circuit board everywhere except very near to the chip. The remaining open cross-section will not support propagating modes below 30 GHz. Although placing a copper surface close to the chip surface might potentially increase the dissipation of the SMR, our measurements did not indicate that the lid caused any such problems.

Very good discussions of microwave sample packaging design for low-temperature experiments may be found in the dissertations by Schuster [79] and Mazin [15].

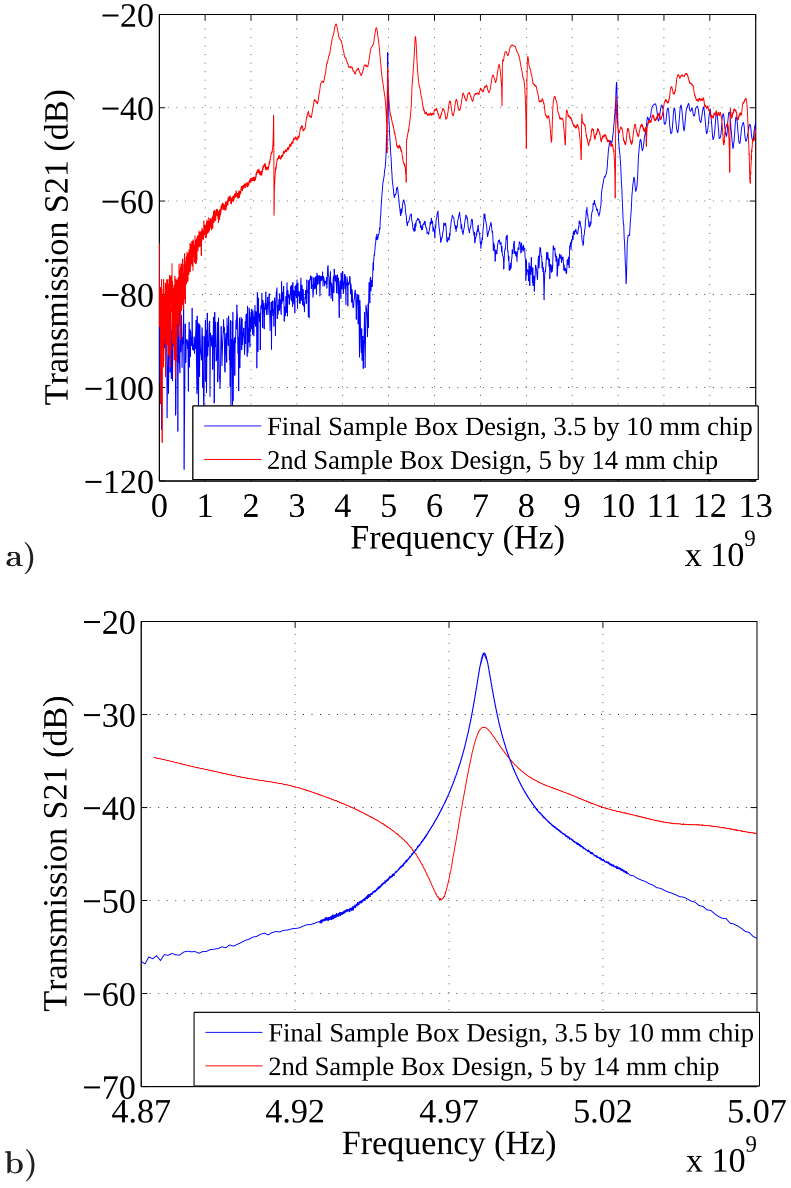

Figure 4.15: Results of sample box design development. Early designs held larger-area chip. Here the SMR in the early-type box has a fundamental mode at $\sim$ 2.5 GHz, the one in the later-type box $\sim$ 5 GHz. Both are prototype designs of SMR only, no NR. Devices were tested in fridge at $T < 50$ mK. **a)** Transmission spectra through device plus signal lines. Early design transmitted excess “bypass” power through spurious modes of box and chip. Final design achieved $>$ 40 dB suppression of all modes except through SMR itself, at frequencies up to about 9 GHz. **b)** Same measurement on narrower span showing clearly how microwave bypass power obscures SMR Lorentzian resonance. Signal line loss is appx 20 dB at 5 GHz.

4.5 Microwave filter cavities

As described in section 3.3, thermal noise in the signal lines at frequencies around ω_{SMR} can excite the SMR resonance, thus leading to backaction driving of the NR. Our microwave sources (Agilent E8257D and Rohde and Schwarz SMA100A) produce phase and amplitude noise totaling -145dBc/Hz at a frequency offset ~5.5 MHz from the carrier. In these experiments we used pump strengths at a frequency of $\omega_{SMR} - \omega_{NR}$ up to 14 dBm at the fridge input, meaning that the noise power density at ω_{SMR} will be up to ~-131dBm/Hz. By comparison, the Johnson noise emitted into the 50 ohm lines by dissipation at room temperature is -174 dBm/Hz. The cold attenuators on the fridge (fig 4.1) are intended to suppress the Johnson noise only.

To suppress the excess noise, we use TE011 cavity filters, following a design described in Ref. [80] and Ref. [81]. Figure 4.16 shows design and photographs of our microwave filter cavities. These were machined from OFHC copper, then heat treated at > 400C, then electro-plated with Au (Alfa Aesar, stock number 42307). To tune the frequency of each cavity, we insert or remove a 4mm diameter quartz rod mounted on a threaded rod at one end of the cavity. Because the axis of the cavity is a node of the resonance, this varies the effective dielectric constant without appreciably affecting the quality factor or insertion loss. To increase the conductivity of the copper and thereby improve the quality factor, we cool the cavities to 77K by mounting in a sealed probe filled with He gas and immersed in liquid nitrogen.

At an offset of 5.57 MHz from the carrier, we obtain a filtering factor greater

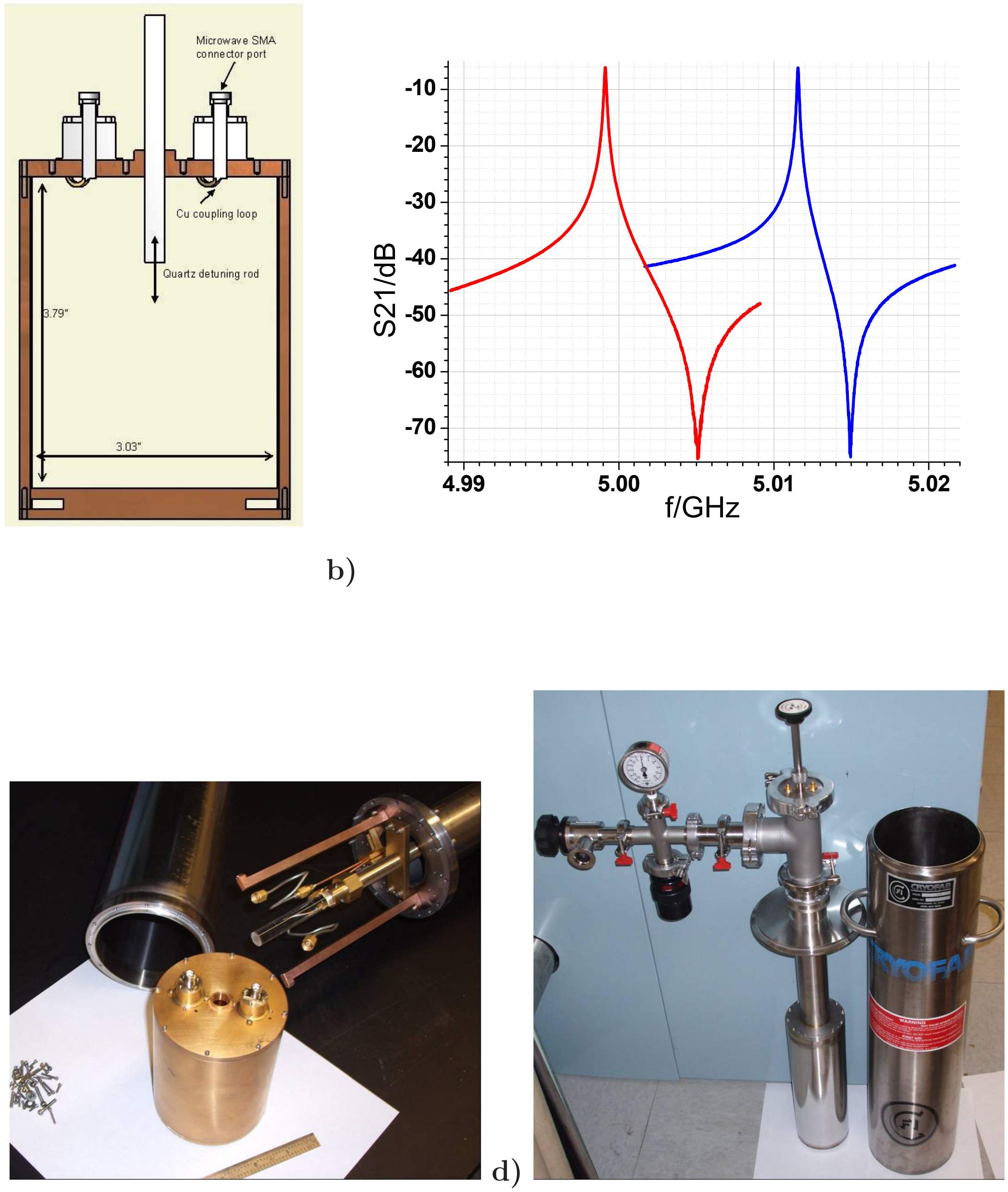

a) b)

c) d)

Figure 4.16: Filter cavity for suppressing phase noise. **a)** Design. **b)** Transmission of filter cavity tuned to maximum and minimum frequencies, measured at 77 K. Q ranges from 35373 to 41826. Sharp "dip" to the right of each peak is due to fortuitous interference with adjacent mode of cavity. **c)** Cavity and mounting brackets with quartz tuning rod. **d)** Assembled probe ready for cooling to 77 K.

than 50 dB. (see figure 4.16(b)), suppressing the phase noise to ∼-195 dBc/Hz. Even when a microwave pump power of +25dBm is applied, the phase noise at the input of the device should be far below the level of quantum vacuum fluctuations, i.e. the noise level of one quantum in the SMR (∼ -205 dBm/Hz). On resonance, the insertion loss of these filters was about 7 to 9 dB, thereby limiting the maximum pump powers that could be applied to the fridge.

To test the effectiveness of the filter cavities, we applied a microwave pump signal at several powers at frequency $\omega_{SMR} - \omega_{NR}$, with and without the use of filter cavities inline with the microwave source. These measurements were made through the SMR used for cooling and backaction evasion in the fridge. Figure 4.17 shows a wide span plot of the measured spectrum at two pump powers, and figure 4.18 shows the noise power density at ω_{SMR} as a function of pump power. This data demonstrates that even at the highest pump powers used in those measurements, when the filter cavities were employed, the phase noise of the microwave source did not excite the SMR out of its ground state, and the measurement noise remained dominated by amplifier noise.

Design, assembly and initial testing of the filter cavities was carried out by T. Rocheleau and M. Savva.

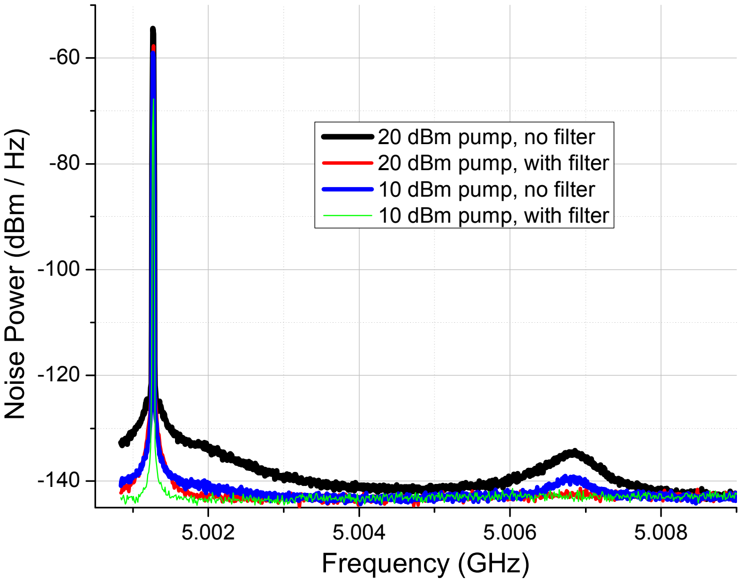

Figure 4.17: Power measured on spectrum analyzer (10 kHz bandwidth) while applying a fixed pump tone to the device at two different powers, with and without copper filter cavity. Pump at $\omega_{SMR} - \omega_{NR}$ is evident in plots. Excitation of SMR by microwave source phase noise is clearly seen when filter is not used.

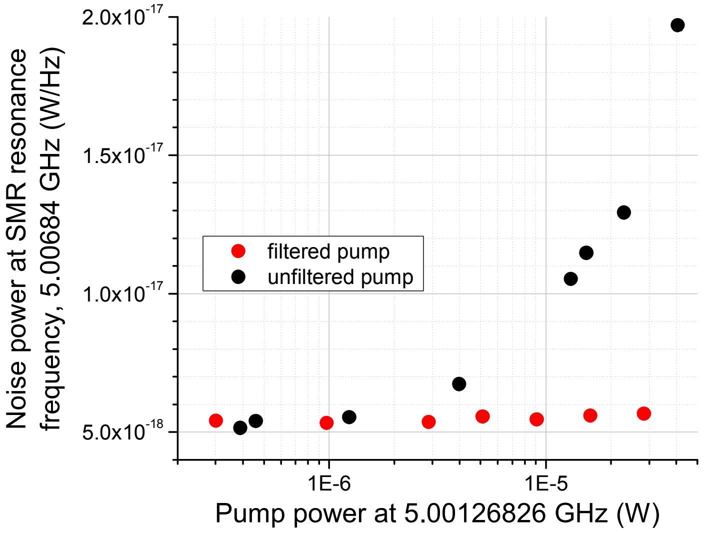

Figure 4.18: Noise power density S_{bgd} measured at SMR resonant frequency while pumping at $\omega_{SMR}-\omega_{NR}$. Filter cavity suppresses excitation of SMR by source phase noise.

Chapter 5

Measurement Methods

5.1 Characterization of SMR

To characterize the SMR, we use a network analyzer at the drive and return lines measure to its S21 parameter, i.e. transmission spectrum. A typical measurement appears in figure 5.1. We find the S21 to follow a Lorentzian form as in equation (2.35), and fit the spectrum to find κ and ω_{SMR}. Because of the recent experimental interest in SMRs, there has been much study of the various dissipation mechanisms in microfabricated superconducting waveguide at millikelvin temperatures. [82] [11] In the SMR that we used for backaction cooling and evasion experiments, at the power levels employed in those experiments the quality factor of was approximately 1.014×10^4, corresponding to a linewidth of 494 kHz. Section 5.4 describes how we estimate the portions attributable to internal dissipation and external loading, κ_{int} and κ_{ext}.

High pump powers are essential to achieving high coupling between SMR and NR for backaction cooling and sensitive position measurement. At sufficiently high powers, however, the current in the SMR will approach the critical current of the material; in this regime we expect an increasing population of quasiparticles in the superconductor to manifest as excess internal RF dissipation in the SMR. Measurements of the total dissipation κ of four SMR devices having two different designs of

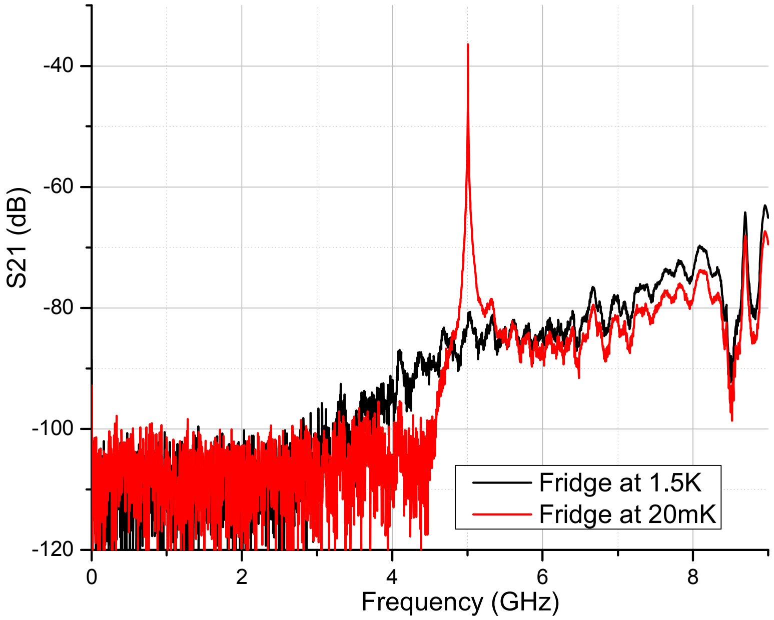

Figure 5.1: Wide span transmission spectrum of the sample. When the SMR is superconducting, the 5 GHz resonance is clearly visible, but vanishes when the SMR is normal (1.5K).

κ_{ext} appear in figure 5.2 as a function of internal circulating power within the SMR. Above 100 microwatts, we do see a distinct increase in internal dissipation. However, we find that in the sample we chose to use for backaction cooling and evasion studies, the κ degrades at a power about 20 times lower. The sharp step-change in κ at $P_{SMR} \simeq 5\mu$W (equivalent to $\bar{n}_{SMR} \simeq 3 \cdot 10^8$) was accompanied by strong internal dissipation and thermal heating in the SMR, setting an upper bound on the power we can employ with this sample. The poorer performance of this device has not been adequately explained and may be related to the damage to the aluminum film during fabrication, as described in section 4.3. Unfortunately, the other samples either were not fabricated with nanomechanical resonators, or the NRs had unsatisfactory coupling or were damaged on cooldown.

Using a simple model for the superconducting critical current density, $J_c = H_c/\mu_0\lambda_L$, where λ_L is the London penetration depth of ~ 20 nm, we find for aluminum $J_c \simeq 4 \cdot 10^{11}$ A/m^2, from which we find in our SMR geometry (assuming the RF current in our SMR penetrates only to the London depth) critical current $I_c \simeq 100$ mA. Using equation (2.39) this is equivalent to a power of ~ 100 mW in our 50-ohm waveguide, much higher than the onset of excess dissipation in our devices. The higher current densities that may in practice appear at edges or defects in the superconducting film may account for this discrepancy.

We found that the best way to measure dependence of κ on power was to add a splitter to the input line, and apply a fixed power microwave tone off-resonance from the SMR, while simultaneously using a network analyzer at a much weaker power to trace out the S21 response. In this way the internal power in the SMR was

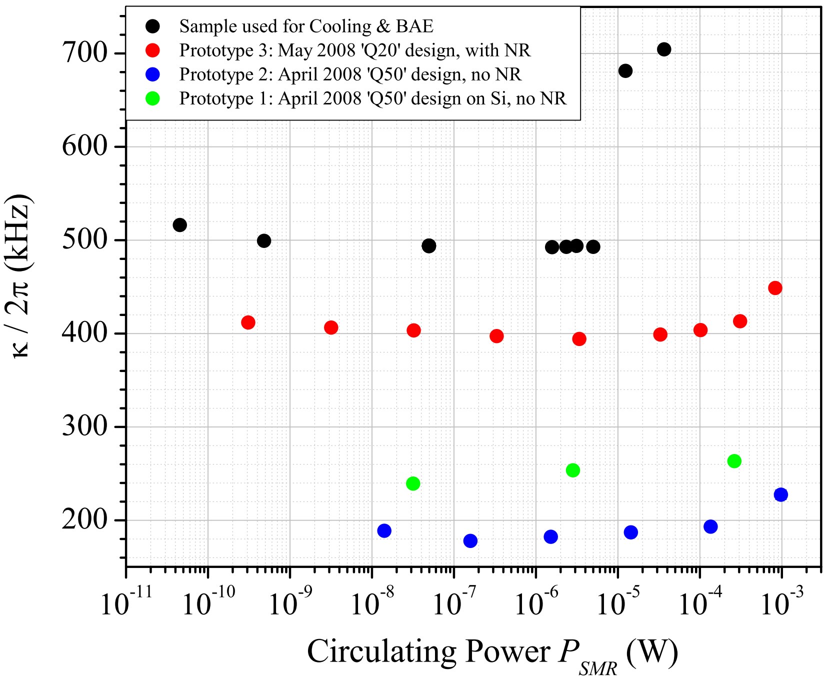

Figure 5.2: SMR linewidth vs circulating power in SMR. Four different devices, all measured at $T < 100$ mK. Measurements made by varying power of network analyzer. Circulating power P_{SMR} was calculated from equation (2.37) for $\Delta\omega = 0$. Black points are device used in measurements of chapter 6; red points are a different device having identical SMR design. For these two devices, calculation of P_{SMR} employed κ_{ext} and *loss* found in section 5.4. Green and blue points are another SMR design, for which the calculation of P_{SMR} employed values of κ_{ext} estimated from geometry, and estimated linelosses of the particular cables installed for those measurements.

maintained approximately fixed while the network analyzer swept frequencies. If we instead used the network analyzer to apply high power, then at high pump powers the κ_{int} dependence on P_{SMR} meant that different frequencies sampled different κ, distorting the lineshape. (The measurements appearing in figure 5.2 were not made in this way, so at the highest pump powers the κ may be only approximate.)

In developing our device, we measured more than a dozen different SMRs, varying materials and design seeking a design with low internal dissipation. One remarkable observation we made is that SMRs fabricated on top of high-stress SiN films on Si substrates exhibited severe excess internal dissipation, so much in fact that no resonance could be observed. We also fabricated chips with identical waveguide that had no breaks, whose transmission could be measured directly, and found that the dissipation in the $\lambda/2$ length of CPW on the chip was ~ 1.5 dB. This behavior was orders of magnitude greater than the published levels of dissipation in silicon nitride [11], and remains unexplained. Identical designs made on silicon showed no such dissipation. At least three SMRs were also fabricated on low-stress SiN films on Si substrates and did not exhibit the severe dissipation. Among other factors that we investigated were the use of high-resistivity Si substrates, the presence of small amounts of platinum on the chips (used as lithography alignment marks in locations far from the CPW gap), and the presence or absence of a superconducting groundplane on the backside of the chip. None of these were found to dramatically affect the quality factor of the SMR.

We expect internal dissipation in the SMR and variation in the SMR frequency to vary with temperature due to RF dissipation and kinetic-inductance of

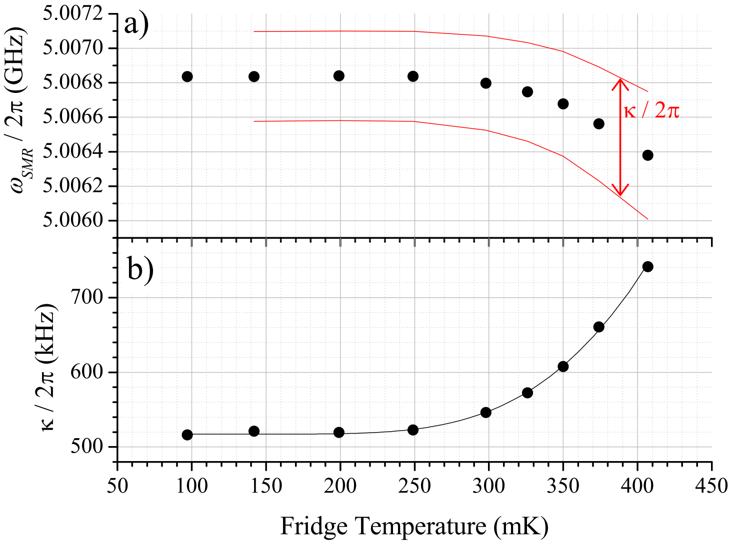

Figure 5.3: (a) SMR frequency vs. temperature, with linewidth boundaries overlaid. (b) SMR linewidth vs. temperature. Fit line is of the form $\kappa = \kappa_0 + \alpha \cdot e^{-\beta/T}$ predicted by BCS.

thermally-excited quasiparticles, as predicted by BCS theory. [10] Figure 5.3 shows temperature dependence of ω_{SMR} and κ. The critical temperature of the Al film was measured directly in the separate "transmission" waveguide device described above, and found to be 1.15 K. However, as this Al film was fabricated separately it may not accurately indicate the T_c of the Al used in the device for bacakction cooling and measurement.

5.2 Measured and calculated NR characteristics

Fabrication of our nanomechanical beam resonator is described in section 4.3. This resonator vibrates in tensile mode like a stretched string, with a restoring force contributed by the tension in the material, and a sinusoidal mode shape. The tension is intrinsic to the nitride film due to its growth at temperatures > 800 C and subsequent differential thermal contraction of the film and substrate, producing tensile stress in the film. To grow our nitride, we used process conditions demonstrated previously to produce a stress of 1200 MPa and density of 2.7 g/cc. [77] Our earlier designs [68] employed low-stress silicon nitride which relies on a restoring force due to the elastic modulus of the nitride. Such bending-mode resonators have a non-sinusoidal mode shape and higher mechanical dissipation than tensile-mode resonators. [83] The tensile mode is expected to have a frequency $\omega_{NR} = 2\pi \cdot \frac{n}{2l}\sqrt{\frac{S}{\rho A}}$, where n is the mode number ($n = 1$ for the fundamental mode), S is the tensile stress, ρ is the density and A is the cross-sectional area of the nitride. We assume that the aluminum on top of the beam has density 2.7 g/cc and contributes only added mass per unit length to the beam, not to the restoring force. For $l = 30\mu$, beam width 170 ± 10 nm, SiN thickness 60 ± 5 nm and Al thickness 105 ± 10 nm, we expect $\omega_{NR} = 2\pi \cdot 6.7$ MHz. The measured value of 5.57 MHz is somewhat lower than is likely given our uncertainties in dimensions, but may indicate a lower than expected stress in the nitride film. It is also possible that the undercut of the beam ends during fabrication adds slightly to the effective length, or that compressive stress in the aluminum film partially counteracts the tensile stress in the nitride.

We tested several prototype coupled SMR-NR devices before selecting one to make the backaction cooling and evasion measurements reported in chapter 6. It was common to observe the NR resonating at two frequencies, typically separated by a few tens of kHz. The measured amplitude at one frequency was smaller than at the other, suggesting that the two frequencies represent orthogonal vibrational modes x and y of the doubly-clamped beam comprising the NR. Oscillation y perpendicular to the gate would have a coefficient $\frac{\partial C_g}{\partial y}$ much smaller than for the in-plane x motion. In subsequent measurements we focused on the motion exhibiting the higher coupling, and ignored the presumably perpendicular mode.

Figure 5.4 shows measured values of the NR linewidth and frequency as a function of fridge temperature. The linewidth Γ_{NR} exhibits a linear temperature dependence which enables mechanical quality factors exceeding 10^6 at temperatures below 50 mK. However, at temperatures below about 150 mK the linewidth also appears to be perturbed by a time-varying dissipation which is also apparent in the measurements of thermal excitation of the NR mode. (See section 5.5.) Since these linewidths were found from Lorentzian fits of long averages of the NR response excited by thermal noise, as described in section 5.3, it is also likely that the apparent value is greater than the actual value of Γ_{NR} due to drifts in the frequency over time scales of minutes. Very small values of Γ_{NR} at the lowest temperatures indicate weak coupling to the thermal bath, and probably contribute to the poor thermalization of the NR to the fridge temperature in this regime.

The oscillation of the sinusoidally-shaped deflection of the 30 micron long NR is detected as a change of capacitance C_g defined by a fixed gate electrode covering the middle 26 microns of that length. It is convenient to reduce this two-dimensional oscillatory motion to an equivalent one-dimensional motion that may be described as a simple harmonic oscillator. Details of this kind of calculation have been described elsewhere for the case of a bending-mode resonator. [75] If the beam length is

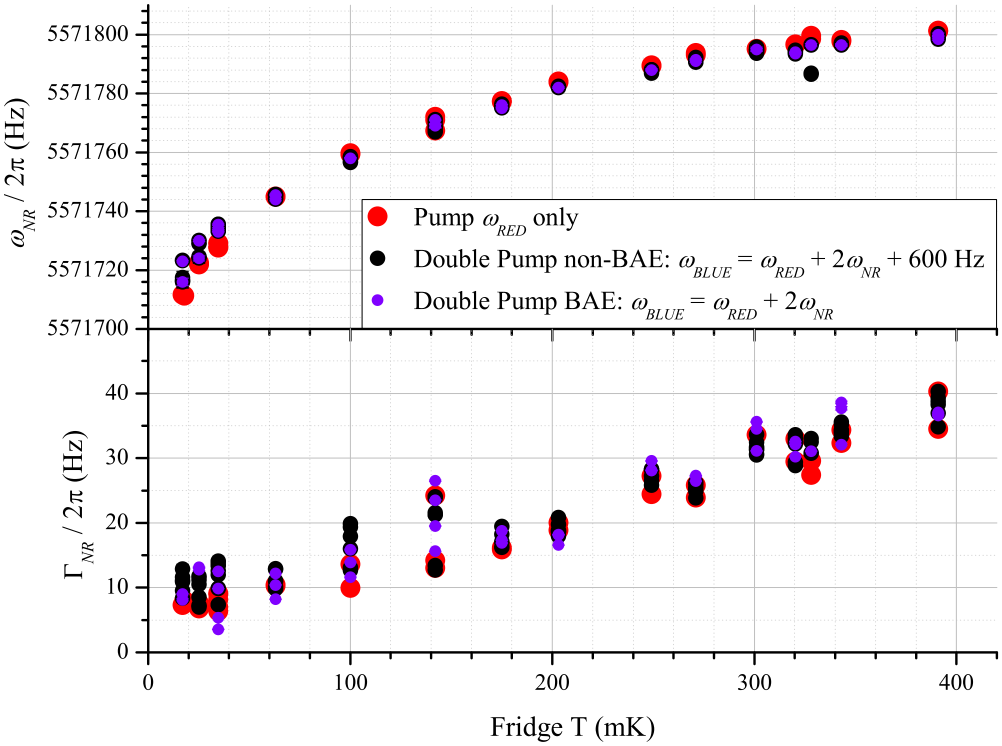

Figure 5.4: NR frequency and linewidth plotted against fridge temperature. Three different pump configurations. Same dataset as figure 5.6. Note that the linewidth appears linear with temperature down to ∼ 150 mK, below which is is believed to be affected by the same unexplained force-noise bath that prevents the NR motion from thermalizing to the fridge at these temperatures. (See section 5.5.) Considering only the datapoints recorded using a single red pump tone, a linear fit of all points above 150 mK yields a slope of 95 ± 9 Hz / K, passing through the origin with standard error of 2 Hz. The adjusted R-squared coefficient of this fit is 0.89.

in dimension z and we denote the deflection in the x direction as $u(z)$, then the kinetic energy per unit length dz is $\frac{1}{2}\rho A\left(\frac{du(z)}{dt}\right)^2 dz$. If $u(z,t) = u_{max}\sin\left(\frac{\pi z}{l}\right)e^{i\omega_{NR}t}$, where u_{max} is the deflection amplitude at the midpoint of the resonator, then we may integrate from 0 to l to find that the total energy amplitude of the NR is $\frac{1}{4}m_{tot}u_{max}^2\omega_{NR}^2$, where $m_{tot} = \rho Al$. However, instead of u_{max} we'd like to re-express this in terms of the average amplitude $\langle u_g\rangle$ over the length of the gate. This is actually the quantity that we measure as a change in the capacitance C_g. In our equivalent one-dimensional model we call this amplitude x_0. (See e.g. equation (2.41).) For beam length $l = 30$ microns, with a 26 micron gate, and mode shape $u(z) = u_{max}\sin\left(\frac{\pi z}{l}\right)$, we find $\langle u_g\rangle = 0.72\cdot u_{max}$. We equate the total kinetic energy calculated above to the potential energy of our equivalent 1-dimensional device, $\frac{1}{2}kx_0^2$, where the spring constant $k = m\omega_{NR}^2$ is defined in terms of an "effective mass" m. Thus we have $\frac{1}{2}kx_0^2 = \frac{1}{2}m\omega_{NR}^2\langle u_g\rangle^2$ equal to $\frac{1}{4}m_{tot}u_{max}^2\omega_{NR}^2$, from which we find effective mass $m = 0.97\cdot m_{tot}$. Using our values of the NR dimensions, we find $m_{tot} = 2.3\pm 0.3$ pg, $m = 2.2\pm 0.3$ pg and $k = 2.70\pm 0.37$ N/m.

5.3 Sideband measurement using spectrum analyzer

To detect the motion of the mechanical resonator when pumping at $\omega_{SMR}\pm\omega_{NR}$, we observe the sideband falling at frequency $\omega_{SMR} = 2\pi\cdot 5.00684$ GHz. As found from circuit analysis (equations (2.53) and (2.52)), the sideband voltage is proportional to mechanical amplitude x and total sideband power is proportional to RMS mechanical amplitude $\langle x^2\rangle$. To detect the motion we merely measure the sideband voltage or power directly at frequency ω_{SMR}. When the motion is driven by a force noise such as thermal noise, we observe the noise power spectrum on a spectrum analyzer. A wiring diagram for such a measurement appears in figure 4.4. Figure 5.5 shows a typical measured sideband when the NR is driven by thermal noise. Using Matlab software, we fit the sideband to a Lorentzian function $S_{bgd} + P_{sideb} \cdot \frac{4\Gamma_{tot}}{\Gamma_{tot}^2 + 4(\omega - \omega_{NR})^2}$, to determine the linewidth Γ_{tot}, background level S_{bgd} (in units of W/Hz), mechanical frequency ω_{NR} and peak area equaling P_{sideb} (in units of W). S_{bgd} is a measure of amplifier noise. In some cases it will also have a contribution due to excitation of the SMR, which may be driven by phase noise of the microwave source, thermal excitation of the SMR, or noise deliberately injected to study back-action evasion.

In addition to measurements of NR motion driven by thermal noise, we can also drive the NR directly at a single frequency with an electrostatic force through the "low frequency signal line" installed on the fridge and coupled to the SMR drive line via a bias tee. (See figure 4.1.) DC or low-frequency oscillating voltages on the order of a volt applied at the top of the fridge will be attenuated in the signal line and be capacitively divided by $\frac{C_\kappa}{C}$ within the SMR, but still produce voltages on the order of a mV across C_g, enough to drive the NR at detectable levels. Sweeping drive frequencies reveals the same Lorentzian lineshape as seen in figure 5.5. Direct drive of the motion with a coherent signal at the resonance frequency ω_{NR} becomes important in our demonstration of single-quadrature detection (sections 6.5.1 and 6.5).

The NR may be driven by an electrostatic force $\frac{1}{2}\frac{\partial C_g}{\partial x}V^2$ across the gate.

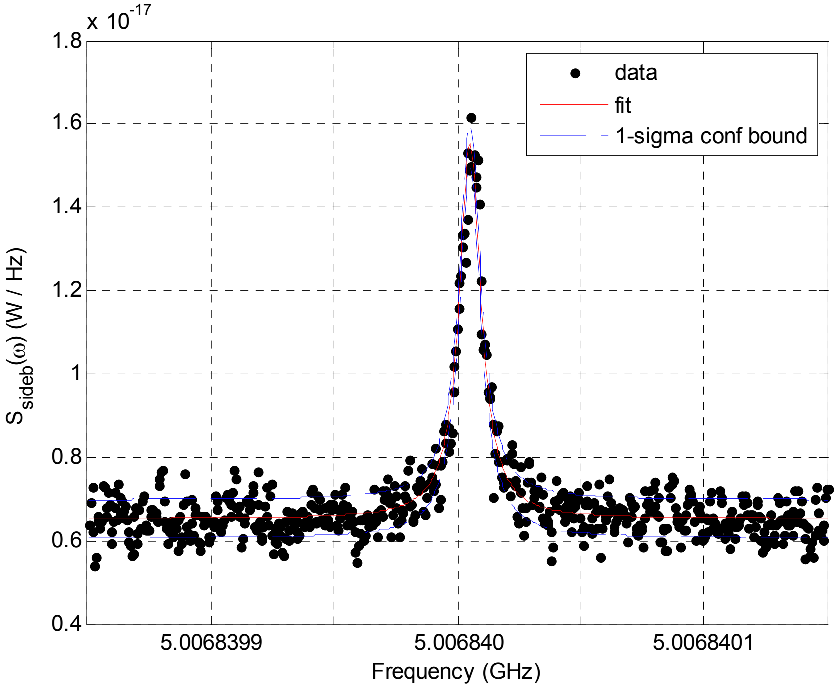

Figure 5.5: Typical motional sideband observed at frequency ω_{SMR} while pumping at frequency $\omega_{SMR} - \omega_{NR}$. Fridge T = 63 mK. Lorentzian fit to function $S_{bgd} + P_{sideb} \cdot \frac{4\Gamma_{tot}}{\Gamma_{tot}^2 + 4(\omega - \omega_{NR})^2}$ yields linewidth of 10.4 ± 0.2 Hz, $P_{sideb} = 149 \pm 3$ aW and $S_{bgd} = 6.56 \pm 0.01$ aW/Hz. This measurement appears as a datapoint at T = 63 mK in figure 5.6. Measurements included in figure 5.6 resulted from Lorentzian fits with adjusted R-squared coefficients ranging from 0.7 to 1.0. R-squared coefficient in this fit is 0.87.

Applying a voltage $V = V_{DC} + V_{drive}\cos(\omega_{NR}t)$ should result in a driving force $\frac{\partial C_g}{\partial x} \cdot V_{DC} \cdot V_{drive}\cos(\omega_{NR}t)$. However, we found omitting V_{DC} we were equally successful in driving the NR. This suggests that at low temperatures the SMR centerline is completely electrically isolated from ground and has trapped on it enough charge to carry a DC voltage on the order of a mV. A charge of 10^{-15} coulombs, or only about 6000 electrons, on the 1 pF SMR capacitance would produce a voltage of 1 mV. Slight variations or fluctuations in this charge due to leakage currents or other effects account for the variation in the drive amplitudes we were able to attain, and may also contribute to the unexplained fluctuating force-noise that we observed to drive the NR at low temperatures. (See section 5.5.)

5.4 Estimation of line loss, gain and κ_{ext}

Our ability to compare measurements precisely with theory depends on how well we know the energy $\hbar\omega_{SMR}\bar{n}_{SMR}$ stored in the SMR at any given applied pump power. We may determine $\bar{n}_{SMR}$ from either the applied or transmitted pump powers P_{in} or P_{out} using equations (2.33) or (2.34). Considering equations (2.35), (2.33) and (2.53), we can see that this relies on precision of parameters *loss*, *gain*, κ and κ_{ext}. While κ is a directly measurable quantity, the others are not. In section 5.5 below we show how we use the equipartition theorem to directly calibrate our measurement of the mechanical mode temperature. It would be very appealing to replicate this with the SMR in order to determine *gain* and κ_{ext}. The thermal occupation $\bar{n}^T_{SMR}$ of the SMR should follow the fridge temperature according to Bose-Einstein statistics, and should emit a frequency spectrum following equation (3.18). This noise should be detectable as a small temperature-dependent noise peak on top of the 3.56 K amplifier noise. However, an attempt to detect this was unsuccessful because other dissipative elements in the fridge wiring also emit Johnson noise at frequencies near ω_{SMR}. Noise emitted by the microstrip thermalizers or circulators between the SMR and HEMT amplifier partially reflect from the SMR, making it difficult to distinguish precisely the microwave noise emitted by the SMR.

To determine *gain*, we employ the noise emitted by our HEMT amplifier as a calibrated signal level. The amplifier noise temperature ($T_n = 3.56 \pm 1$ K at 5 GHz) was measured by the vendor at a temperature of 20 K on calibrated equipment before delivery to us. The uncertainty of ±1 K was communicated to us by the people who designed and built the amp, as an estimate of both systematic variations in the performance of the amplifier and their uncertainty in measuring the device before delivery. For the gain calibration, we treat the noise temperature as a broadband noise power density $k_B T_n$ at the input of the amplifier, and neglect any noise generated by dissipative elements between the device and amplifier, because these are all at temperatures < 1 K. Because the HEMT amplifier noise dominates the noise of all components beyond it in the circuit, the white noise power density at the spectrum analyzer should simply equal $k_B T_n \cdot gain_{amp}$, where $gain_{amp}$ is the total gain from the HEMT amp input to our spectrum analyzer. The *total* gain, however, must also include the losses between the sample and amplifier, which we estimated (see section 4.1) to be 1.5 ± 1 dB. Thus $gain = gain_{amp} - 1.5$ dB. The circuits depicted in figures 4.1 and 4.4 apply here, with microwave pumps shut off.

We expect *gain* to vary with frequency due to weak resonances in the lengths of cable separated by many joints lying between the HEMT amplifier and our measurement point. We also expect slight variations in gain over time, as the temperature of the cabling in the fridge varied and as we had to disconnect and reconnect components in the room-temperature wiring for different measurements. We observed both kinds of effects causing variations up to about 1 dB. In one early set of measurements we recorded the noise spectral density over a range of frequencies from $\omega_{SMR} - \omega_{NR}$ to $\omega_{SMR} + \omega_{NR}$. From this data we calculated that $gain(\omega_{SMR} - \omega_{NR})$ is 0.77 dB less than $gain(\omega_{SMR})$, and $gain(\omega_{SMR} + \omega_{NR})$ is 0.11 dB greater than $gain(\omega_{SMR})$. To account for time-variation in gain, in each dataset we used the S_{bgd} values determined from fits of the motional sideband (section 5.3) while applying low pump powers, to recalculate $gain(\omega_{SMR})$. From this we could estimate $gain(\omega_{SMR} \pm \omega_{NR})$ in each dataset as needed. (A better technique might be to shut off the microwave pump periodically during each dataset and measure the noise levels at $gain(\omega_{SMR} \pm \omega_{NR})$ directly.) For the datasets appearing in chapter 6, the gain values were,

Blue pump, 142 mK (fig 6.1):

$gain(\omega_{SMR}) = (1.1 \pm 0.4) \cdot 10^5$, $gain(\omega_{SMR} + \omega_{NR}) = (1.0 \pm 0.4) \cdot 10^5$

Red pump, 142 mK (fig 6.1):

$gain(\omega_{SMR}) = (8.9 \pm 3.0) \cdot 10^4$, $gain(\omega_{SMR} - \omega_{NR}) = (7.5 \pm 2.5) \cdot 10^4$

Double pump, 142 mK (fig 6.1):

$gain(\omega_{SMR}) = (9.1 \pm 3.1) \cdot 10^4$, $gain(\omega_{SMR} - \omega_{NR}) = (7.6 \pm 2.6) \cdot 10^4$

Red pump, 17 mK (fig 6.1):

$gain(\omega_{SMR}) = (9.4 \pm 3.2) \cdot 10^4$, $gain(\omega_{SMR} - \omega_{NR}) = (7.9 \pm 2.7) \cdot 10^4$

Red pump, 20 mK (fig 6.3):

$gain(\omega_{SMR}) = (6.6 \pm 2.2) \cdot 10^4$, $gain(\omega_{SMR} - \omega_{NR}) = (5.6 \pm 1.9) \cdot 10^4$

These values range from 48 to 50 dB, similar the estimate of 51 dB gain found from the HEMT amplifier gain specification along with room-temperature and 4 K measurements of various components (sections 4.1 and 4.2). Once we know $gain(\omega_{SMR})$, we can find the coupling κ_{ext} of the SMR to the signal lines, exploiting our good precision ability to measure the mechanical mode temperature based on the thermal calibration (section 5.5), as well as our ability to directly measure the backaction damping Γ_{opt}. The mechanical sideband during backaction cooling measurements can then act as a calibrated power source. As discussed in section 3.1.3 in reference to equation (3.11), we expect the total rate of photons $\bar{n}_{NR}\Gamma_{opt}$ upconverted from the NR into the SMR, multiplied by the SMR energy per photon, to be the power in the sideband. The total measured sideband power should then be the portion of this that is emitted by the end-coupling of SMR and amplified: Thus $P_{sideb} = \hbar\omega_{SMR}\bar{n}_{NR}\Gamma_{opt}\left(\kappa_{ext}/2\kappa\right) \cdot \mathrm{gain}$. For each set of cooling data (section 6.2) we determine Γ_{opt} at each datapoint by a Lorentzian fit of the thermal-noise sideband, to find $\Gamma_{tot} = \Gamma_{NR} + \Gamma_{opt}$, then subtract the values found at the lowest pump powers which should be equal to just Γ_{NR}. T_{NR} was found from measured sideband areas scaled by the thermal calibration, and $\bar{n}_{NR}$ found from $T_{NR}k_B = \hbar\omega_{NR}\bar{n}_{NR}$. Values of *gain* are known as described above, and P_{sideb} is directly measured. We calculated an average value of κ_{ext} for each of the single-pump datasets appearing in chapter 6 (i.e. the ones listed above), and averaged the four values together to find $\kappa_{ext}/\kappa = 0.61 \pm 0.24$.

Using equation (2.25) we find the corresponding value of C_κ is 4.38 ± 0.84 fF. This is in somewhat larger than the design value of 3.0 fF, discussed in section 4.3, but not unreasonable given the difficulty of designing such electrical microstructures with good precision. We may also readily calculate the internal quality factor of the SMR (section 2.2.1) to be $Q_{int} = (2.6 \pm 1.6) \cdot 10^4$. Clearly the quality of our SMR is limited by large internal losses. The uncertainties in these calculated values are traceable ultimately to the uncertainty in the HEMT amplifier noise temperature used as a calibration for *gain*, as well as the ±1 dB uncertainty in the losses between the device and the amplifier.

If we know in a given measurement both power P_{in} applied at the input of the fridge and P_{out} transmitted, and we know both *gain* and κ_{ext}, then we can also calculate *loss* using equation (2.35). Using the 142 mK red-pump and double-pump datasets listed above, we find an average $loss(\omega_{SMR} - \omega_{NR}) = (4.3 \pm 3.9) \cdot 10^{-5}$ and $loss(\omega_{SMR} + \omega_{NR}) = (4.2 \pm 3.8) \cdot 10^{-5}$. The loss is about 44 dB, somewhat less than the 48.5 dB estimated from room-temperature measurements of cables and other components (section 4.1). For the blue-pump dataset at 142 mK (figure 6.1) and for the red-pump dataset at 20 mK (figure 6.3) these values were used to calculate $\bar{n}_{NR}$, because P_{out} was not recorded during those datasets.

5.5 Thermal calibration

Equations (2.53) and (2.35) enable us to find the NR mean-squared amplitude from either P_{sideb}/P_{out} or P_{sideb}/P_{in}. The values of *loss*, *gain*, κ_{ext}, $\partial\omega_{SMR}/\partial x$, $\partial C_g/\partial x$ and C are known a priori to a poor precision, but we may instead exploit the equipartition theorem to obtain a precise calibration of the *mode temperature* of the mechanical motion, T_{NR}. This technique has been discussed extensively elsewhere in references [75], [41], [4] and [3].

We expect $T_{NR} = \frac{\hbar\omega_{NR}}{k_B} \cdot \bar{n}^T_{NR}$ to follow the Bose-Einstein distribution for the average thermal occupation $\bar{n}^T_{NR}$ of a single mode:

$$\bar{n}^T_{NR} = (e^{\hbar\omega_{NR}/k_B T} - 1)^{-1}$$

At temperatures $T \gg \frac{\hbar\omega_{NR}}{k_B}$, this reduces to $T_{NR} = T$, so the measured NR mean-squared amplitude should be proportional to the temperature of its thermal environment, i.e. the fridge. Assuming a single-sided power spectral density, we expect the power spectrum of thermal motion of the NR to be

$$S_x^{NR}(\omega) = \frac{4k_B T_{NR}\omega_{NR}}{mQ_{NR}} \frac{1}{\left(\omega^2 - \omega_{NR}^2\right)^2 + \left(\omega\omega_{NR}/Q_{NR}\right)^2} \tag{5.1}$$

the integral of which gives $\int_0^\infty S_x^{NR}(\omega)d\omega/2\pi = \langle x^2 \rangle = k_B T_{NR}/k$, where k is the spring constant of the NR, found from the estimated effective mass m as $k = m\omega_{NR}^2$. Thus comparing equations (2.35) and (2.53) we expect

$$\frac{P_{sideb}}{P_{out}} = \left[\left(\frac{\partial\omega_{SMR}}{\partial x}\frac{1}{\kappa}\right)^2 \cdot 2\frac{k_B}{k}\right] \cdot \frac{gain(\omega_{SMR})}{gain(\omega_{pump})} \cdot T_{NR} \tag{5.2}$$

$$\frac{P_{sideb}}{P_{in}} = \left[\left(\frac{\partial\omega_{SMR}}{\partial x}\frac{1}{\kappa}\right)^2 \cdot 2\frac{k_B}{k} \cdot loss(\omega_{pump}) \cdot \frac{\kappa_{ext}^2}{\kappa^2 + 4(\omega - \omega_{SMR})^2} \cdot gain(\omega_{SMR})\right] T_{NR} \tag{5.3}$$

The values of P_{sideb} are found from Lorentzian fits of the measured sideband, as described in section 5.3. Figure 5.6 shows P_{sideb}/P_{out}, plotted against fridge temperature, using all of the pump configurations employed with the device used in cooling and BAE measurements (except for single-pump, blue detuned.) While backaction driving or cooling effects would make the measurements deviate from equipartition, in these measurements backaction may be neglected because the SMR was not excited above its ground state, and the measurements made with a single red-detuned pump used a weak enough power so that $\Gamma_{opt} \ll \Gamma_{NR}$. At temperatures above 250 mK, the linewidth κ of the SMR was observed to increase due to the RF dissipation of thermally excited quasiparticles in the aluminum. The data in figure 5.6 was therefore corrected at each temperature by multiplying by $\left(\frac{\kappa(T)}{2\pi \cdot 494 \text{ kHz}}\right)^2$.

At temperatures above 60 mK, the response to all pump configurations closely follows the fridge temperature and the measured power agrees closely with what we expect from the device. In this regime a linear regression fit of all P_{sideb}/P_{out} measurements vs fridge temperature yields

$$P_{sideb}/P_{out} = (4.20 \pm 8.79) \times 10^{-12} + (2.78 \pm 0.03) \times 10^{-9} \cdot T_{NR} \qquad (5.4)$$

From this we see that the intercept is consistent with zero, and we define the empirical calibration factor $\text{cal}(P_{out}) = (2.78 \pm 0.03) \times 10^{-9}$ kelvin^{-1}. (A similar analysis was also done for P_{sideb}/P_{in}, yielding $\text{cal}(P_{in}) = (8.33 \pm 0.05) \times 10^{-12}$ kelvin^{-1}. In the fit of P_{sideb}/P_{in} vs fridge temperature, due to excess scatter and variations in line loss or gain it was necessary to set the intercept to zero.)

As can be seen from expressions (5.2) and (5.3), $\frac{P_{sideb}}{P_{out}}$ is a much more reliable

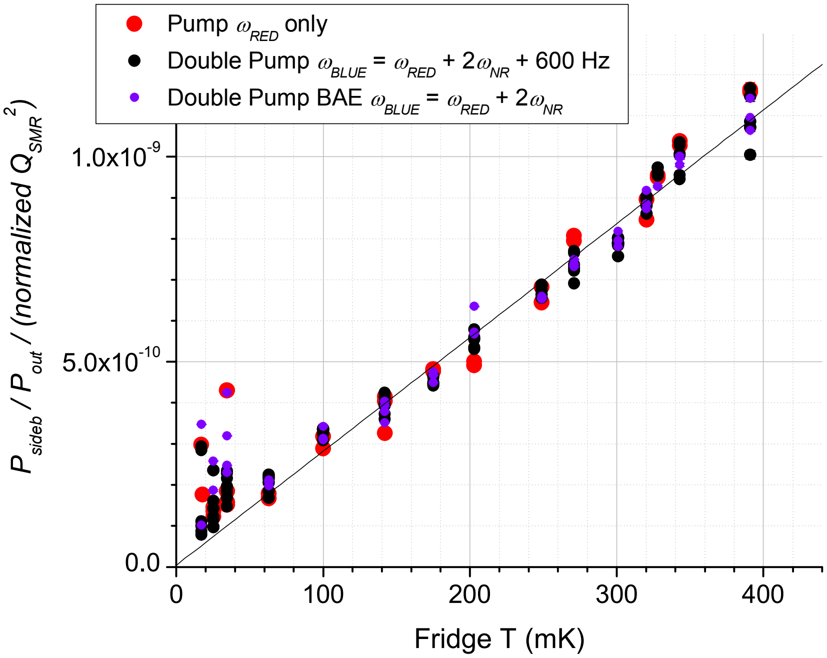

Figure 5.6: Thermal calibration data for device used in cooling and BAE measurements. Three pump configurations. Sideband power divided by transmitted pump power, plotted vs. fridge temperature. The linear fit excludes measurements below 63 mK where the device appears to be poorly thermalized. Adjusted R-squared coefficient of the fit is 0.98.

measure of the motion of the NR than $\frac{P_{sideb}}{P_{in}}$, because $\frac{gain(\omega_{SMR})}{gain(\omega_{pump})}$ is unlikely to change much over time, whereas absolute values of $gain(\omega_{SMR})$ and $loss(\omega_{pump})$ can vary up to about a dB between datasets, as described in section 5.4.

Using equation (5.2) and the value of cal(P_{out}), and accounting for the differences in gain at ω_{pump} and ω_{SMR} (see section 5.4), we can calculate $\frac{\partial\omega_{SMR}}{\partial x}$. We find that $\frac{\partial\omega_{SMR}}{\partial x} = 2\pi \times (7.5 \pm 1.6 \text{ kHz/nm})$. This agrees reasonably well with what we expect from the calculated value of effective SMR capacitance C and estimates of $\frac{\partial C_g}{\partial x}$ based on the geometry of the device. Further discussion appears in section 6.2.

It is interesting to note that below 60 mK, the NR appears to decouple from the thermal bath of the fridge temperature and be strongly coupled instead to an unidentified dissipative bath whose properties vary on a time-scale of seconds. The dissipation in this bath causes the NR quality factor to fluctuate from $\sim 5 \cdot 10^5$ to $> 10^6$, while the force noise in this bath drives the NR mode temperature to varying levels up to 7 times the fridge temperature. In past measurements of nanomechanical resonators it is not unusual to see the motion decouple from the thermal bath at the lowest fridge temperatures. [4] However, it is novel to observe the NR actually appear to be "heated" to greater mode temperatures as the fridge temperature drops. From the observed mode temperature of ~50 to ~150 mK and linewidths of 5 to 10 Hz (figures 5.6 and 5.4 at fridge T below 60 mK) we can estimate the NR to be driven by a white force noise at frequencies around ω_{NR} of $3 \cdot 10^{-19}$ to $10^{-18} N \Big/ \sqrt{Hz}$. The nature of this fluctuating force noise is unclear. The careful filtering we employed in all of the signal lines (section 4.1) suggests that it is not due to noise or thermal heating entering via the signal lines. As discussed in section 6.2, there is some evidence that microwave pump power can excite it. This behavior presents an impediment to the goal of cooling the NR motion to its quantum ground state, and is worth investigating further in future experiments.

Chapter 6

Results and Discussion

6.1 Summary of device parameters

Table 6.1: Geometric parameters of device used for backaction cooling and evasion measurements.

	Fabrication geometry, verified by inspection in SEM:	
w_{CPW}	16 μm	Width of Al centerline
d_{CPW}	10 μm	Gap between centerline and ground plane
t_{CPW}	260 nm	Thickness of Al film on SMR
l	30 μm	length of mechanical resonator
l_g	26 μm	length of capacitive gate opposite NR
w_{NR}	170 nm	width of mechanical resonator
t_{SiN}	60 nm	thickness of SiN
t_{Al}	105 nm	thickness of Al film on NR
d	85 nm	Distance between the NR and gate
	Parameters calculated using the geometry:	
m	$(2.2 \pm 0.3) \cdot 10^{-15}$ kg	effective mass of NR
k	2.70 ± 0.37 N/m	spring constant of NR
Z_0'	50 Ω	Characteristic impedance of CPW waveguide forming SMR
Δx_{ZP}	26 fm	zero-point motion of the NR

6.2 Backaction cooling

We studied backaction damping and cooling of the NR motion by applying a microwave pump tone at $\omega_{SMR} - \omega_{NR}$, and varying the pump power up to the maximum that the SMR could withstand, equivalent to about $3 \cdot 10^8$ pump quanta circulating within the SMR. At each pump power, we recorded the noise spectrum of

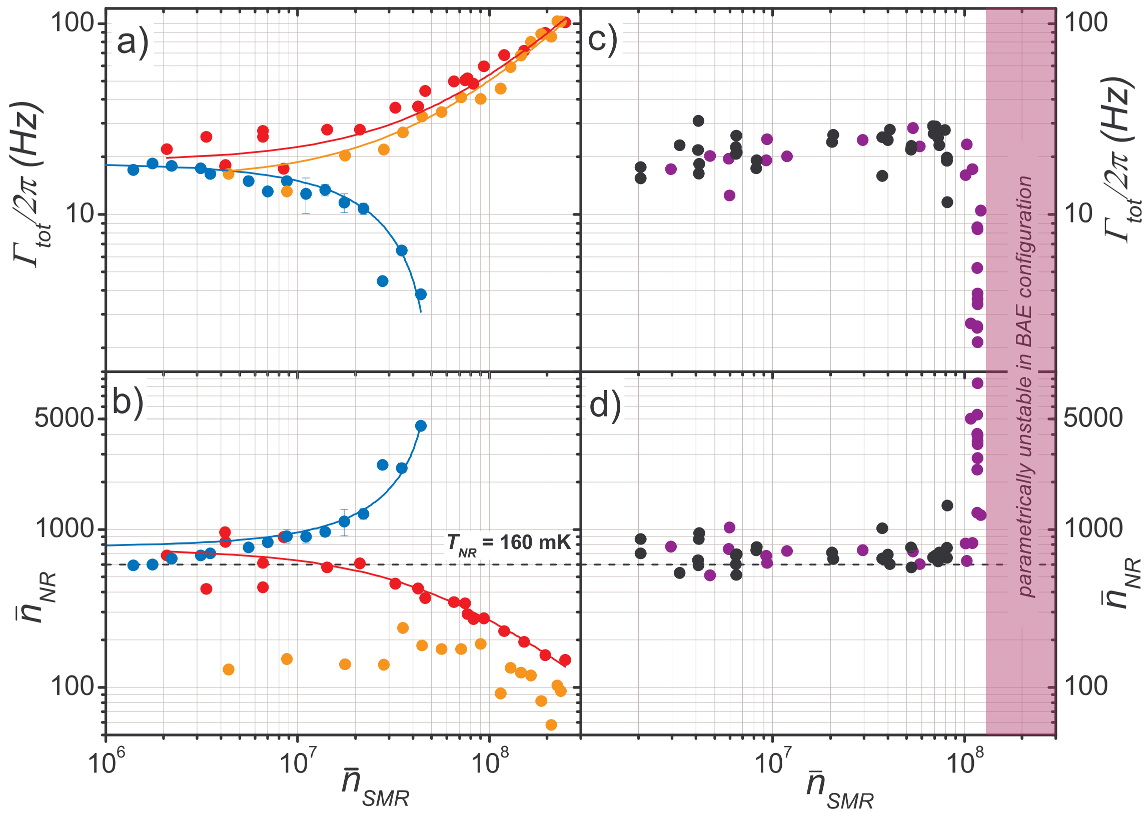

Figure 6.1: NR linewidth, $\Gamma_{tot}/2\pi$, and occupation factor, $\bar{n}_{NR}$, vs. average number of microwave photons $\bar{n}_{SMR}$ circulating within the SMR. **(a)** and **(b)** show NR behavior for a single pump tone: $\omega_{red} = \omega_{SMR} - \omega_{NR}$ (red and orange points) or $\omega_{blue} = \omega_{SMR} + \omega_{NR}$ (blue points). Solid lines show fits of the data to equations (3.3) and (3.6). Note that in **(b)** a fit of the base-temperature points (orange) to equation (3.3) was not possible due to fluctuating $\bar{n}^T_{NR}$ at this temperature. **(c)** and **(d)** show behavior for two simultaneous pump tones: The BAE condition (purple points) $\omega_{red} = \omega_{SMR} - \omega_{NR}$ and $\omega_{blue} = \omega_{SMR} + \omega_{NR}$, or the balanced pump, non-BAE condition (black points) $\omega_{red} = \omega_{SMR} - \omega_{NR}$ and $\omega_{blue} = \omega_{SMR} + \omega_{NR} + 2\pi \cdot 600\text{Hz}$. The latter condition balances rates of phonon upconversion and downconversion (note that 600 Hz $\ll \kappa/2\pi$), but offers no backaction evasion because the sidebands of the two processes do not overlap. In the BAE configuration (purple points), at high pump power we observe narrowing of Γ_{tot} and mechanical amplification due to the parametric amplification effect of the double pump tones having difference frequency $2\omega_{NR}$. Significant scatter in the parametrically-amplified datapoints results from unexplained drifts of up to ~5 Hz in Γ_{NR} and ω_{NR}. Shaded region is inaccessible to BAE due to parametric instability. Red, blue, black and purple points taken at a fridge temperature of 142mK, orange points taken at a fridge temperature of ~20mK.

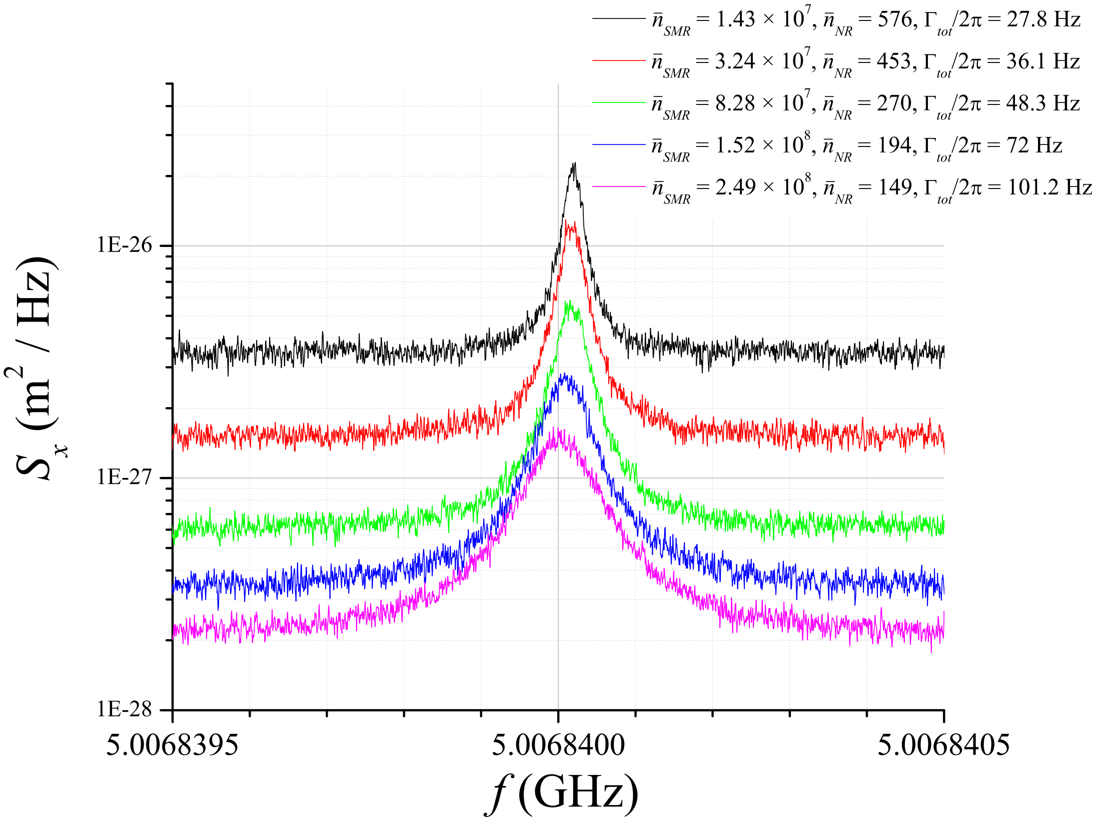

Figure 6.2: NR position noise spectra. Five representative measurements selected from 142 mK cooling dataset (fig 6.1, red points). For increasing pump amplitude, sideband peak exhibits broader linewidth and smaller total area (indicating cooling) and reduced background level (indicating improved position sensitivity, see section 6.6). Position noise calculated from measured power spectra via Eq. (6.5). Area of each Lorentzian equals $\langle x^2 \rangle$ for that measurement.

Table 6.2: RF parameters of device used for backaction cooling and evasion measurements.

	Determined from direct RF measurement:	
ω_{SMR}	$2\pi\cdot 5.00684$ GHz	SMR resonant frequency
κ	$2\pi\cdot 494$ kHz	SMR damping rate
ω_{NR}	$2\pi\cdot$ 5.5717 MHz	NR resonant frequency (varies by ~50 Hz with temperature, ~10 Hz with random drift)
	Parameters derived from RF measurement:	
C	1.0 pF	Effective SMR capacitance
L	1.0 nH	Effective SMR inductance
C_κ	4.38 ± 0.84 fF	Coupling capacitance into and out of SMR
$\frac{\partial C}{\partial x}$	3.0 ± 0.6 aF/nm	Change in SMR capacitance for NR displacement
$\frac{\partial \omega_{SMR}}{\partial x}$	$2\pi \cdot (7.5 \pm 1.6)\frac{\text{kHz}}{\text{nm}}$	Coupling constant
C_g	253 ± 54 aF	Capacitance between the NR and SMR
$\frac{\partial^2 C}{\partial x^2}$	0.06 F/m^2	2nd derivative of capacitance with respect to NR position
λ	$2\pi \cdot 0.15$ kHz/nm^2	Nonlinear coupling constant

the thermally-driven sideband at ω_{SMR} representing NR motion. Each sideband was then fit to a Lorentzian to find the NR frequency, linewidth and mode temperature, as described in sections 5.3 and 5.5. To prevent phase noise of the microwave source from exciting the SMR above its ground state, we used a microwave filter cavity inline with the microwave source. These measurements were repeated at several fridge temperatures. As shown in the thermal calibration (section 5.5) at fridge temperatures below 100 mK the NR was coupled to an additional force-noise bath of unknown origin that had a time-varying effective temperature greater than the fridge temperature. Measurements taken at 142 mK showed much greater stability and offer the clearest demonstration of backaction cooling, appearing in panels a) and b) of figure 6.1. This dataset was also used to determine position sensitivity of the device, which will be discussed below in section 6.6. Figure 6.1(a) and (b) also shows backaction cooling data taken at the fridge base temperature. Figure 6.2 shows several of the spectral measurements used to compile the data appearing in figure 6.1(a) and (b).

To compare the results with the theory described in section 3.1.3, the NR linewidth $\Gamma_{tot} = \Gamma_{NR} + \Gamma_{opt}$ and occupation number $\bar{n}_{NR}$ are plotted in figure 6.1(a) and (b) against the pump energy stored in the SMR, expressed as an average number of pump photons $\bar{n}_{SMR}$. For the datasets represented by red, blue, black and purple points, $\bar{n}_{SMR}$ was calculated using equation (2.34) from the pump power P_{out} transmitted through the SMR, amplifiers and signal lines (along with the parameters κ_{ext}, *loss* and *gain* determined as described in section 5.4). For the blue points, P_{out} was not recorded, so Eq. (2.33) was used to find $\bar{n}_{SMR}$ from P_{in}.

The data in figure 6.1(a) and (b) may then be fit to the theory represented by equations (3.6) and (3.3). The measured NR linewidth Γ_{tot} is fit to the equation $\Gamma_{tot} = (\Gamma_{NR} + \Gamma_{opt}) = (\Gamma_{NR} + \beta \cdot \bar{n}_{SMR})$ while the NR occupation $\bar{n}_{NR}$ is fit to $\bar{n}_{NR} = \Gamma_{NR}\bar{n}^T_{NR} / (\Gamma_{NR} + \beta \cdot \bar{n}_{SMR})$ in a simultaneous least-squares fit, using free fit parameters Γ_{NR}, $\bar{n}^T_{NR}$ and β, using "Origin" software. The fitting routine uses a Levenberg-Marquardt algorithm. From equation (3.6) we note that parameter β represents the coupling between SMR and NR: $\beta = \frac{4}{\kappa}\left(\Delta x_{ZP}\frac{\partial \omega_{SMR}}{\partial x}\right)^2$. For the dataset taken at 20 mK (orange points in figure 6.1), Γ_{NR} could not be fit, so only Γ_{tot} was fit.

Values of Γ_{NR} and $\bar{n}^T_{NR}$ are set by the environment and may vary from one dataset to another, but the coupling should be a fixed parameter of the device.

Indeed, independent fits of all the datasets shown in figure 6.1 (a) and (b) as well as the fit of Γ_{tot} measured while the SMR was excited (figure 6.3, see below) found values of β agreeing within uncertainty. We used the average of these, $\beta = 2\pi \cdot (3.49 \cdot 10^{-7}\text{ Hz})$, in figure 6.1 to produce all of the fit lines. The other fit parameters were

Red pump, fridge T = 142 mK:

$\bar{n}_{NR}^{T} = (752 \pm 41\ )$, $\Gamma_{NR} = 2\pi \times (19.1 \pm\ 3.7\text{ Hz})$

(42 points, reduced $\chi^2 = 7.5 \times 10^3$, adjusted $R^2 = 0.89$)

Blue pump, fridge T = 142 mK:

$\bar{n}_{NR}^{T} = (777 \pm 39\ )$, $\Gamma_{NR} = 2\pi \times (18.5 \pm 0.3\text{ Hz})$

(34 points, reduced $\chi^2 = 3.5 \times 10^4$, adjusted $R^2 = 0.96$)

Red pump, fridge T = 20 mK:

$\Gamma_{NR} = 2\pi \times (15.3 \pm\ 1.2\text{ Hz})$

(linear fit, 17 points, adjusted $R^2 = 0.97$)

Here the uncertainties are the standard errors of the fit values. Given that the datasets were taken on different occasions separated by weeks, these results represent reasonable fits of the data to equations (3.6) and (3.3) using parameters that are well within expectation.

We can quantify the maximum achieved cooling rate of $\Gamma_{opt} \simeq 2\pi \cdot 100$ Hz in terms of a cooling power $\dot{Q}$. As Γ_{opt} is the rate at which NR quanta are extracted by the upconversion process, we have $\dot{Q} = \Gamma_{opt} \cdot \hbar\omega_{NR} = 2.3 \cdot 10^{-24}$ W. The lowest occupation achieved by the backaction cooling was $\bar{n}_{NR} = 58 \pm 0.2$, achieved at base temperature. However, the fluctuating $\bar{n}_{NR}^{T}$ at this fridge temperature made this result difficult to reproduce. This behavior is discussed in section 5.5 as appearing to indicate that the NR is coupled to an additional time-varying force-noise in addition to the thermal bath, and that at the lowest fridge temperatures the coupling Γ_{NR} to the thermal bath is weak enough for the additional unidentified force-noise to dominate.

At these low fridge temperatures, another effect that may counteract the cooling is thermal absorption of applied RF power by the SMR and/or the NR. Such effects are hard to quantify, but one observation may be made by looking at the plot of NR frequency vs fridge temperature in figure 5.4. In this data, the double pump measurements employed a higher power than the single-pump measurements. At temperatures above 100 mK, where the NR is well coupled to the thermal bath, the NR frequency drops slightly with increasing pump power, as expected due to electrostatic frequency shift (section 3.5). However, at the lowest fridge temperatures, the NR frequency increases with pump power, suggesting that the NR is being thermally heated a few tens of mK by the applied RF power. There is also some evidence that RF power excites the excess force noise, leading to a hysteresis in the mode temperature with respect to microwave power levels. In one trial with the fridge held at 17 mK, we observed the NR mode temperature initially to be ~ 40 mK. After the microwave power was cycled to high levels and then reduced, the mode temperature was > 100 mK.

At a fridge temperature of 142 mK, these poor thermalization effects and thermal heating effects were less severe. (See also for example the discussion of excess backaction in section 6.8.) However the higher starting temperature meant that the lowest occupation achieved through backaction cooling was $\bar{n}_{NR} = 149.3 \pm 0.2$. With this behavior in mind, future experiments intending to cool the mechanical motion to its quantum ground state should not anticipate that the mode will thermalize to temperatures below 100 mK. Instead, other improvements are needed to the device to enhance the cooling power. Our clearest limitation in this experiment is the degradation in SMR dissipation for $\bar{n}_{SMR} \gtrsim 3 \cdot 10^8$. This is most likely due to the critical current of the SMR being suppressed due to contamination of the aluminum during the fabrication process. (See section 4.3.) Greater care in fabrication could distinctly improve the power-handling of the SMR. Further improvements in the power handling could be made by using a material such as Nb having a higher critical current. Considering equations (3.6) and (2.40), other enhancements in cooling power could also be made by reducing the linewidth κ of the SMR (using smaller capacitances C_κ at the ends of the SMR), and improving the coupling $\frac{\partial \omega_{SMR}}{\partial x}$. The latter could be readily improved by reducing the capacitance C of the SMR by raising the characteristic impedance Z_0' of the waveguide. (See section 2.3.) Improvements to the capacitance derivative $\frac{\partial C_g}{\partial x}$ could be made by reducing the gap d between NR and gate, but as this is already only 85 nm, reducing it much further will be technologically challenging. These tradeoffs are further discussed in section 3.1.4.

From the values of the fit parameter $\beta = \frac{4}{\kappa}\left(\Delta x_{ZP} \frac{\partial \omega_{SMR}}{\partial x}\right)^2$, and the estimated values of Δx_{ZP} and measured value of κ, we can derive values of the coupling $\frac{\partial \omega_{SMR}}{\partial x}$. We find $\frac{\partial \omega_{SMR}}{\partial x} = 2\pi \times (8.0 \pm 2.1 \text{ kHz/nm})$. This agrees well within uncertainty to the value $\frac{\partial \omega_{SMR}}{\partial x} = 2\pi \times (7.5 \pm 1.6 \text{ kHz/nm})$ derived from the temperature calibration

(See section 5.5). We can also use these values to make an estimate of the capacitance C_g between NR and SMR. Using a value of 7.5 ± 1.6 kHz/nm in the expressions in equations (2.53), we can use equation (2.40) to find $\frac{\partial C_g}{\partial x} = 3.0 \pm 0.6$ aF/nm, and from this we use the approximation $\frac{\partial C_g}{\partial x} \simeq \frac{C_g}{d}$ to estimate $C_g = 253 \pm 54$ aF.

Capacitance of these complicated structures is difficult to estimate accurately from geometry. A very crude model is to treat C_g as a parallel-plate capacitor, i.e. $C_g = \epsilon_0 \cdot l_g \cdot t_{Al}/d$, which yields a capacitance of 280 aF. This is an underestimate, because fringing fields contribute to the capacitance more in our device than in a parallel-plate geometry. We can also compare to the gate capacitance seen in past experiments. Naik (Ref. [41]) used an NR of similar geometry whose gate electrode was a 1 micron long single-electron transistor, across a 100 nm gap. This device had $C_g = 33.6$aF. Extrapolating to our much longer gate and narrower gap yields 1030 aF, which should be an overestimate because fringing fields at the ends of the gate are less important in a longer device. Nonetheless, these estimates suggest that our measured value of gate capacitance is about a factor of two smaller than expected. A probable cause of this discrepancy arises in the fabrication. Since the SMR and NR are fabricated in two separate steps, they are separated by a joint containing a thin insulating layer of native Al oxide. (See section 4.3 for fabrication details.) If the capacitance thereby added in series with C_g is of the same order as C_g, it would produce the observed discrepancy. Solving this problem would distinctly improve the coupling and the cooling power. Possible solutions might be to greatly increase the joint area, to ion-mill before the second deposition to remove the Al oxide, or to deposit the material for NR and SMR in the same fabrication step.

6.3 Backaction cooling when SMR is excited by noise

In section 3.3 we discussed the behavior of backaction cooling when the SMR is thermally excited. When $\bar{n}_{SMR}^{T} > 0$, the backaction will no longer appear to the NR as a zero-temperature bath, but will drive the NR with backaction, setting a limit on the cooling. In this case we cannot neglect the $\Gamma_{opt}\bar{n}_{NR}^{opt}$ term in the detailed balance equation (3.3), but approximately set the thermal occupation of the SMR $\bar{n}_{SMR}^{T}$ equal to $\bar{n}_{NR}^{opt}$. The sideband due to backaction-driven motion of the NR will add coherently with a 180 degree phase shift to the thermal noise in the SMR, so that the measured sideband does not accurately indicate the actual NR occupation. The proper value of $\bar{n}_{NR}$ may be found from the data using equation (3.23).

We studied this behavior by omitting the filter cavity at the microwave source during backaction cooling, thus allowing the phase noise of the microwave source to excite the SMR. These measurements were done at fridge base temperature. Phase noise power scales with pump power, and at the highest pump powers, the SMR was excited up to $\bar{n}_{SMR}^{T} \simeq 52$. Several measured spectra appear in figure 6.4, and a negative-going sideband appears at the highest pump power due to the backaction.

We determine $\bar{n}_{NR}^{eff}$ from the sideband area by using the thermal calibration described in section 5.5 (no differently than in the case where $\bar{n}_{SMR}^{T} = 0$). The occupation $\bar{n}_{SMR}^{T}$ may be calculated from the measured white noise spectrum at ω_{SMR} by first subtracting the portion attributable to amplifier noise, and scaling the result by the system gain to find the noise spectral density $S_{out}(\omega_{SMR})$ emitted by the SMR at resonance. We then have (modifying Eq. (3.19) to account for the

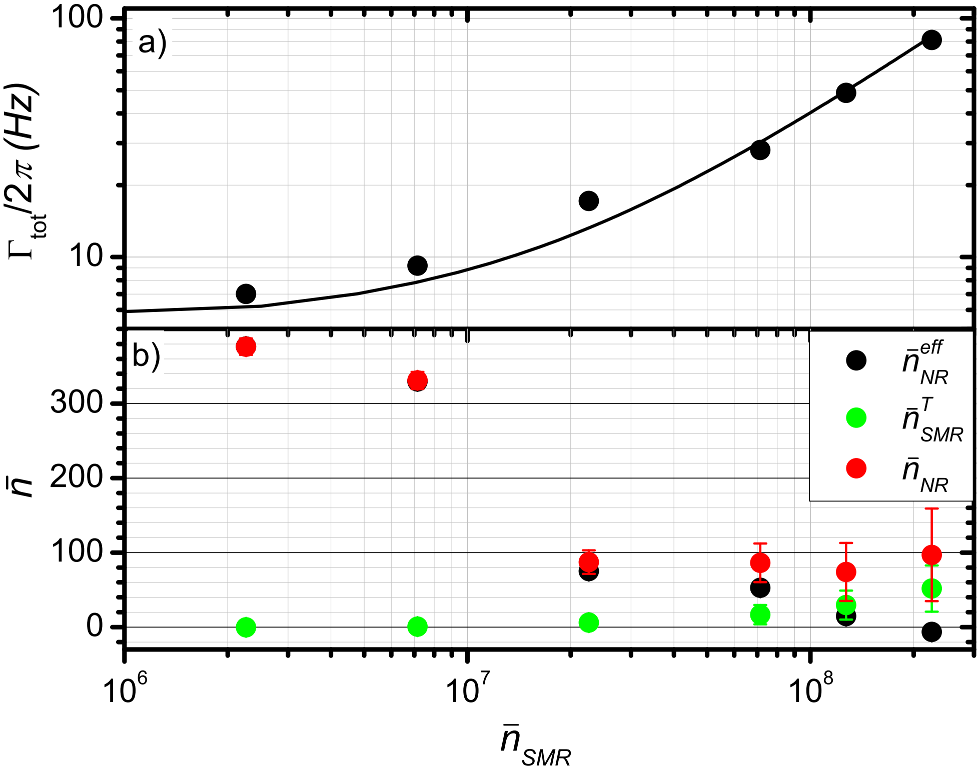

Figure 6.3: Cooling measurement while SMR is pumped at $\omega_{SMR} - \omega_{NR}$ and also driven by microwave source phase noise. Fridge temperature 20 mK. **(a)** NR linewidth, $\Gamma_{tot}/2\pi$, not affected by excitation of SMR. Solid line is a linear fit (8 points, adjusted $R^2 = 0.99$) to Eq. (3.6), as described in section 6.2. **(b)** SMR excitation expressed as an equivalent thermal occupation number $\bar{n}_{SMR}^{T}$, and apparent NR occupation $\bar{n}_{NR}^{eff}$ calculated directly from measured sideband area using thermal calibration factor. Correct NR occupation $\bar{n}_{NR}$ is calculated from these by equation (3.23). Note that at highest pump power $\bar{n}_{NR}^{eff}$ is negative. See also fig 6.4.

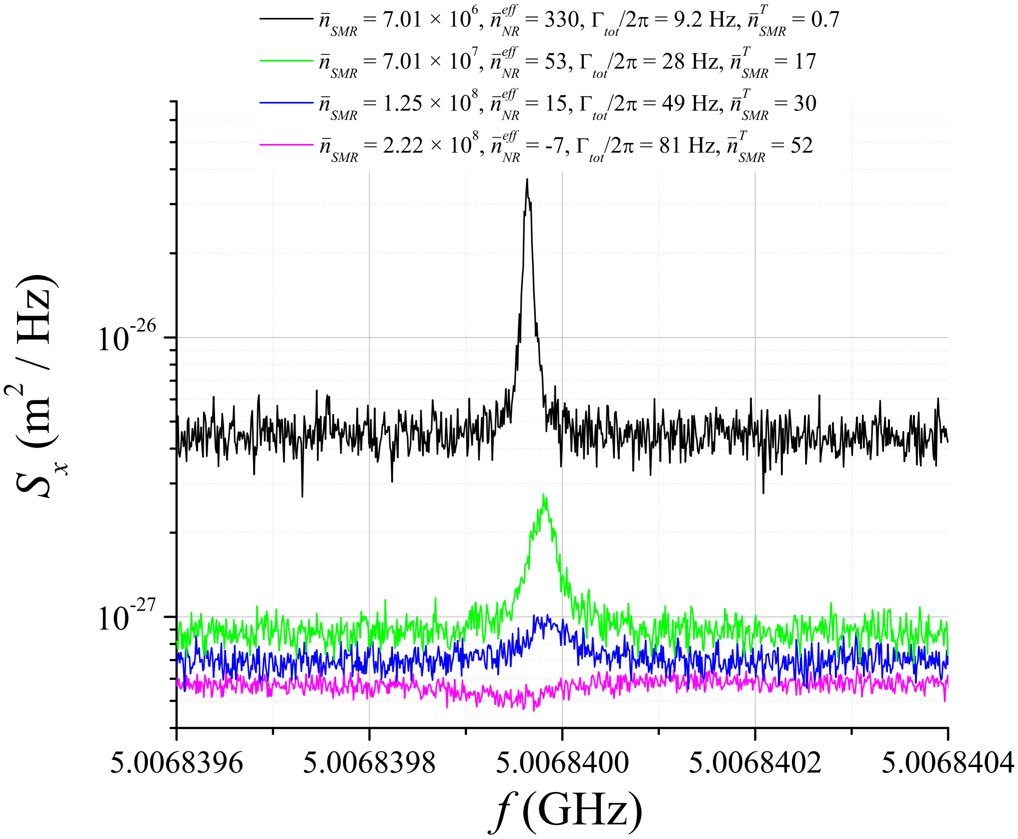

Figure 6.4: NR position noise spectra during backaction cooling measurements while microwave source phase noise excites SMR. Selected from dataset shown in fig 6.3. Position noise calculated from measured power spectra via Eq. (6.5). At high pump powers, background level rises due to excitation of SMR. (Compare to measurements at similar pump magnitude shown in fig 6.2). At highest pump power, backaction-driven motion of NR produces sideband that subtracts from noise level in SMR, yielding negative peak.

subtraction of amplifier noise)

$$\bar{n}^T_{SMR} = \frac{1}{\hbar\omega_{SMR}} \cdot \frac{\kappa}{2\kappa_{ext}} \cdot \frac{1}{gain(\omega_{SMR})} \cdot (S_{N,out}(\omega_{SMR}) - S_{amp}) \tag{6.1}$$

The fit values of linewidth Γ_{tot} and mode temperature $\bar{n}^{eff}_{NR}$ appear in figure 6.3, along with $\bar{n}_{NR}$ calculated using equation (3.23). The optical damping is not affected by the SMR thermal occupation. The fit line in figure 6.3(a) uses the same slope as in figure 6.1 ($\beta = 2\pi \cdot (3.49 \cdot 10^{-7}\text{ Hz})$) and has an intercept $\Gamma_{NR} = 2\pi \cdot (5.4 \pm 1.0)\text{Hz}$, indicating the very low natural NR linewidths that are possible at low fridge temperatures.

The excitation of the SMR places limits on the cooling of the NR motion. The lowest occupation achieved in this dataset was $\bar{n}_{NR} = 74 \pm 39$, much poorer than trials at the same fridge temperature with phase noise suppressed. This clearly demonstrates the utility of suppressing phase noise using the microwave filter cavities. The correction using Eq. (3.23) also imposes large uncertainties on the values of $\bar{n}_{NR}$ because of the uncertainties in $\bar{n}^T_{SMR}$ traceable to the uncertainty in amplifier noise temperature via the determination of system gain and κ_{ext}. (See section 5.4.) While in this device the excitation of the SMR was deliberately introduced, in other cases it could conceivably arise from thermal heating within the SMR or other system components, making it more difficult to control.

6.4 Optical-spring frequency shift

To examine the behavior of the backaction damping and optical-spring frequency shift, we applied a red-detuned pump tone at a fixed power $P_{in} = -7.4$ dBm into the fridge, varying the frequency $\Delta\omega = \omega_{pump} - \omega_{SMR}$ from $2\pi \cdot -8.19$ MHz to $2\pi \cdot -3.19$ MHz, i.e. from $-1.47\omega_{NR}$ to $-0.57\omega_{NR}$. The NR frequency ω_{NR} and linewidth Γ_{tot} were then determined from Lorentzian fits of the NR thermal noise sideband. Measurements were made at a fridge temperature of 145 mK. We were careful to use a low enough pump power that even at the pump frequency closest to ω_{SMR}, the power circulating inside the SMR was low enough not to degrade κ. We expect the behavior to be described by equations (3.16) and (3.15).

In these measurements, a filter cavity was not used to suppress phase noise from the pump source, because re-tuning the filter for each new frequency measurement would have been very tedious. In principle, it is possible for backaction driving of the NR as described in section 3.3 to affect the measurement. While we would not expect backaction driving to affect ω_{NR} and Γ_{tot}, at detunings $\Delta\omega > -\omega_{NR}$ and $\Delta\omega < -\omega_{NR}$, we would expect the backaction-driven NR signal to exhibit a phase shift other than 180 degrees, which when added to the noise amplitude emitted by the SMR would produce a distorted Lorentzian lineshape, which would be difficult to analyze. However, in this case the pump power and resulting phase noise was low enough that $\bar{n}_{NR} \gg \bar{n}^{T}_{SMR}$, so we may neglect backaction driving effects.

The resulting data appears in figure 6.5. When trying to fit the data to equations (3.16) and (3.15), it is important to note that for a fixed applied pump power, $\bar{n}_{SMR}$ varies with $\Delta\omega$ according to equation (2.33). The calculated value of $\bar{n}_{SMR}$ appears in figure 6.5(a) using parameters κ_{ext} and $loss$ determined as described in section 5.4.

Furthermore, the measurements of ω_{NR} will reflect not only the optical-spring

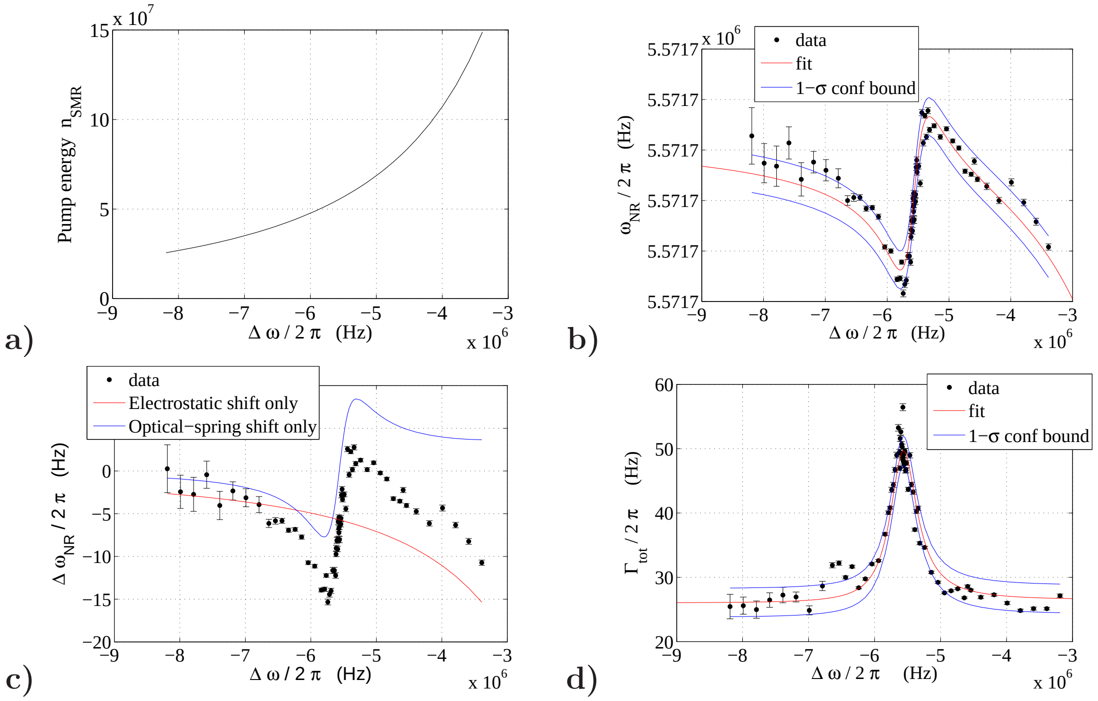

Figure 6.5: NR frequency and linewidth vs. detuning $\Delta\omega$ of pump frequency from SMR frequency, at fixed pump power. **(a)** Calculation of pump magnitude within SMR, $\bar{n}_{SMR}$. **(b)** Measured NR frequency with fit to combined optical-spring and electrostatic frequency shifts (equations (3.15) and (3.41)). **(c)** Shift from ω_{NR}, plotted alongside separate optical-spring and electrostatic frequency shifts, calculated using fit values from (b). **(d)** Measured NR linewidth with fit line (equation (3.16)).

frequency shift but also the electrostatic shift due to k_{EM} as given by equation (3.41). As shown in figure 6.5(b), using "Matlab" software, we fit the measured NR frequency against the frequency shift defined by equation (3.15), plus the shift defined by equations (3.41) and (3.38). Nonlinear least-squares fitting was performed using a Levenberg-Marquardt algorithm, yielding an R-squared value of 0.84. The data is plotted again in figure 6.5(c) as a shift from ω_{NR}, together with the fits of optical-spring and electrostatic frequency shifts shown separately. Fit parameters and their resulting values were $\omega_{NR} = 2\pi \cdot (5571741.1 \pm 0.7 \text{ Hz})$, $\left(\Delta x_{ZP} \frac{\partial \omega_{SMR}}{\partial x}\right)^2 = 4\pi^2 \cdot (0.074 \pm 0.004 \text{ Hz}^2)$, and $\hbar\lambda/2k = (-1.85 \pm 0.20) \cdot 10^{-14}$. From these results we can calculate

$$\frac{\partial \omega_{SMR}}{\partial x} = 2\pi \cdot (10.3 \pm 0.8 \text{ kHz/nm})$$

$$\lambda = 2\pi \cdot (-0.151 \pm 0.026 \text{ kHz/nm}^2)$$

$$\frac{\partial^2 C}{\partial x^2} = (-0.06 \pm 0.01) \text{ aF/nm}^2$$

The fit of Γ_{tot} to equation (3.15) appears in figure 6.5(d). In this fit, we use the fit value of ω_{NR} found from the first fit. The fit parameter $\left(\Delta x_{ZP} \frac{\partial \omega_{SMR}}{\partial x}\right)^2$ in this result is $4\pi^2 \cdot (0.074 \pm 0.004 \text{ Hz}^2)$, yielding $\frac{\partial \omega_{SMR}}{\partial x} = 2\pi \cdot (8.85 \pm 0.68 \text{ kHz/nm})$. The R-squared value in this fit was 0.95.

We can compare these values of $\frac{\partial \omega_{SMR}}{\partial x}$ to the value $2\pi \cdot (7.5 \pm 1.6 \text{ kHz/nm})$ found from thermal calibration (section 5.5). Considering that the data in figure 6.5 was taken over a 24 hour period in which drifts in ω_{NR} and Γ_{NR} may have been several Hz, and that in calculating $\bar{n}_{SMR}$ we could not account for dependence of $loss$ on frequency, and considering the large uncertainties in $loss$ and κ_{ext} that go into determining $\bar{n}_{SMR}$, these results seem to be in reasonable agreement with other measurements for this device (section 6.2).

These results also provide insight into the parametric-amplification effect that will arise when pumping the device simultaneously at both frequencies $\Delta\omega = \omega_{SMR} \pm \omega_{NR}$ for BAE measurement. Given that the natural NR linewidth is $\Gamma_{NR} \simeq 15$ to 25 Hz at a temperature of about 140 mK, we see from figure 6.5(a) and (c) that we can readily generate electrostatic frequency shifts approaching Γ_{NR} at reasonable pump powers. As described in section 3.5, in the BAE pump configuration an oscillating component of the electrostatic frequency shift will lead to amplification of the thermal motion, to degradation of the backaction evasion, and ultimately to uncontrolled self-oscillation of the NR when the frequency shift exceeds Γ_{NR}.

6.5 Backaction-evading single quadrature detection

6.5.1 Demonstration of single quadrature detection

To demonstrate sensitivity to a single quadrature X_1 of the NR motion, we drive the SMR in the BAE configuration of equal microwave pump tones at frequencies $\omega_{SMR} - \omega_{NR}$ and $\omega_{SMR} + \omega_{NR}$. The quadrature X_1 is defined by the phase ϕ_{beat} of the beat frequency of the RF field in the SMR, as described in sections 3.4.2 and 3.4.3,

$$V_{SMR}(t) = V_p \cos(\omega_{SMR} t) \cos(\omega_{NR} t + \phi_{beat})$$

which is the sum of the two pump tones, each of amplitude $\frac{V_p}{2}$. The phases of the two pumps may be known at the input of the signal lines at the top of the fridge; however they will acquire an unknown but fixed phase shift in the signal lines and the coupling into the SMR. Thus the only way to identify the X_1 phase is to measure it. A circuit for this measurement was shown in figure 4.5. For this measurement, ω_{NR} was first determined precisely by applying pumps at $\omega_{SMR}-\omega_{NR}$ and $\omega_{SMR}+\omega_{NR}+2\pi\cdot 600$ Hz and recording the thermal-noise sidebands. (We needed to do this re-measurement of ω_{NR} before each dataset because $\omega_{NR}/2\pi$ could drift 5 to 10 Hz from one day to another. The 600 Hz frequency separation enables the two sidebands to be individually resolved, but being $\ll \kappa/2\pi$ still enables us to treat the measured sideband amplitude as if it were at ω_{SMR}.) Meanwhile, we drive the NR with a fixed-phase RF signal at frequency ω_{NR} as described in section 5.3. The sideband voltage appearing at ω_{SMR} due to this driven motion is downmixed to ω_{NR} and monitored on a lockin amplifier, using the same RF source as a reference. Alternatively, the sideband power could be monitored directly on the spectrum analyzer. The phase of the RF drive was stepped progressively to identify the phase of maximum response, i.e. X_1.

The microwave tone synthesized by the Agilent E8257D exhibited phase drifts of up to a few tens of degrees per hour, resulting in an equivalent drift of ϕ_{beat}. Since varying the RF drive phase over 2π typically required half an hour to an hour of stepping and signal averaging, this could be a problem. To compensate, we extract a portion of the combined pump signal via a microwave directional coupler and apply it to an RF diode, as shown in figure 4.5. The diode bandwidth is $\gg \omega_{NR}$ but $\ll \omega_{SMR}$ so that it registers the envelope of pump power oscillating at twice the pump beat frequency. An attenuator is used to prevent the pump power from driving the diode nonlinear. The diode output is measured on a lock-in amplifier, with the same RF source used to drive the NR used here as a reference, making use of the $2f$ setting on the reference input of the SR844 lock-in. The measured phase was divided by 2 and subtracted from the phase of the RF drive. While the resulting phase value still contains an arbitrary fixed phase shift, it should negate the effects of pump phase slippage.

Figure 6.6(a) shows the results of this measurement, clearly showing sensitivity to a single quadrature of motion, with X_1 falling at about +20 degrees. The vertical scale is the magnitude of the sideband voltage, normalized to its maximum value. Several repetitions were averaged to make this trace, and the error bars are the standard error of the averaged values. It is interesting to note that the measurement does not appear to be entirely insensitive to X_2 motion at about -70 degrees. Imbalance in the two pump amplitudes within the SMR could produce such an effect, which we tried to counteract with careful balancing as described in section 6.5.3. Most likely the small apparent sensitivity to X_2 is due to drifts of a few Hz in ω_{NR} during the measurement, meaning that the NR was not driven exactly on resonance, introducing an additional time-varying phase shift in its response. Nonetheless the results indicate that the selectivity to X_1 is at least a factor of 10. Figure 6.6(b) shows thermally-driven motion of the NR using the same pump configuration (the RF drive is shut off to enable detecting the thermal motion), confirming that introducing two pump tones to produce the BAE pumping configuration has no effect on the device's ability to act as a sensitive position detector.

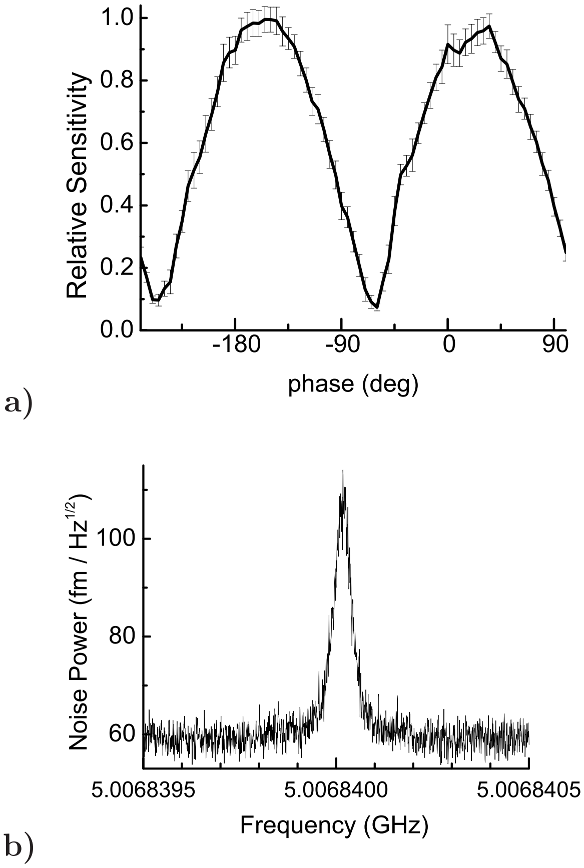

Figure 6.6: BAE pump configuration. Equal pump powers at $\omega_{red} = \omega_{SMR} - \omega_{NR}$ and $\omega_{blue} = \omega_{SMR} + \omega_{NR}$. **(a)** Demonstration of phase-sensitive nature of this scheme. While applying BAE pumps, NR is driven separately with a coherent drive signal at ω_{NR}. The phase of this drive is varied over 2π, while the sideband amplitude at ω_{SMR} is monitored. The response achieves a maximum when the drive excites the X_1 quadrature of NR motion defined by the coherent pump tones, and a minimum when X_2 is excited. Response amplitude is normalized to the X_1 response. Phase offset from 0 degrees is due to fixed phase shifts in signal lines. **(b)** Thermal motion of the X_1 quadrature of NR mode, measured at 142mK. Single-quadrature measurement scheme maintains the same sensitivity to small-amplitude motion. Pump conditions are same as in figure 6.7. Each pump power was ~ -2 dBm at the top of the fridge, for a total occupation of $\bar{n}_{SMR} \simeq 1.2 \cdot 10^7$ pump photons in the SMR.

6.5.2 Demonstration of backaction evasion

To ensure that backaction driving of the NR is restricted to the X_2 quadrature while only the X_1 quadrature is detected, it is necessary for the pump amplitudes within the SMR at the two frequencies $\omega_{SMR} - \omega_{NR}$ and $\omega_{SMR} + \omega_{NR}$ to be of equal amplitude. While we could attempt to balance the pump amplitudes using the estimates of *loss* and *gain* at the two pump frequencies (see section 5.4), given the uncertainties in these values we considered it more accurate to balance the amplitudes using the sidebands themselves, which should be directly proportional to the pump powers and should both undergo the same gain after being emitted by the SMR. We applied pump tones at frequencies $\omega_{SMR} - \omega_{NR}$ and $\omega_{SMR} + \omega_{NR} + 2\pi \times 600$ Hz. At a fridge temperature of 142 mK, we adjusted the balance of powers in increments of 0.2 dB, recording the area of the thermally-driven sidebands of the two pumps, then taking a linear regression to determine the exact pump power ratio that equalized the sideband areas. These measurements were made with filter cavities inline with the microwave sources, so that the precise amplitudes of the thermal noise sidebands would not be obscured by backaction. We repeated this procedure at four different pump powers over a range of 10 dB, and found that in all cases the sideband areas balanced when the transmitted pump powers had the ratio $P_{out}(\omega_{SMR} + \omega_{NR}) = P_{out}(\omega_{SMR} - \omega_{NR}) + 1.1$ dB. This is in reasonable agreement with our separate measurement of 0.88 dB as the difference in gain at these frequencies (section 5.4).

Using this balance of applied pump powers, we measured the NR thermal noise over a range of pump powers. In section 5.5 we showed that the thermal calibration factor is equally applicable to the double-pump configuration, and this was employed to calculate the NR occupation $\bar{n}_{NR}$ from $P_{sideb}/P_{out,redpump}$, assuming that the blue pump was balanced properly. Filter cavities were employed at each microwave source to ensure that no source phase noise excited the SMR, so we should not expect any backaction driving of the NR. The results are plotted in figure 6.1(c) and (d). For the horizontal axis, the occupation of pump photons in the SMR, $\bar{n}_{SMR}$, is calculated in the non-BAE case as the power in one pump, in the BAE case as the total power in both pumps, since in the latter case both pumps contribute to a single measured sideband. In contrast to single-pump measurements made at the same pump powers (panels (a) and (b) of the same figure), no backaction damping or cooling of the NR mode is observed. The absence of backaction damping in both cases is attributable to the balancing of upconversion and downconversion processes described in section 3.1.3. It is notable in this data that the mode temperature of the NR is somewhat higher than the fridge temperature, which we attribute to the unidentified excess force noise discussed in section 5.5. At low fridge temperatures that effect can dominate the NR amplitude but at these fridge temperatures it adds at most a few tens of mK to the NR mode temperature. In the BAE configuration, at the highest pump powers, $\bar{n}_{NR} > 10^8$, we observe linewidth narrowing and amplification of the thermal noise by the parametric amplification effect described in section 3.5.

To demonstrate backaction evasion, we must drive the NR with backaction, and demonstrate that it does not excite the measured X_1 quadrature. The wiring configuration used for this measurement appears in figure 4.4. The backaction is conveniently provided by injecting white noise into the SMR at frequencies around ω_{SMR} while applying pump tones in the BAE configuration after careful measurement of the NR resonant frequency ω_{NR} at the same total pump power. The white noise is generated using a string of three noisy microwave amplifiers, producing a measured noise power density of -96 dBm/Hz, injected into the drive line at the top of the fridge through a 10 dB coupler. Noise of this level excites the SMR into a thermal state with occupation factor $\bar{n}_{SMR}^{T} > 10^4$. At the measurement temperature of 142 mK, the thermally-driven motion of the NR ($\bar{n}_{NR} \simeq 600$) is then much less than backaction-driven motion. In the BAE case, thermal motion in the X_2 quadrature may be neglected, and in a case where backaction drives both quadratures we may neglect the thermal motion in both quadratures. In this measurement we used pump power weak enough that we may neglect parametric amplification. Each pump applied ~ -2 dBm at the top of the fridge, resulting in a total occupation of $\bar{n}_{SMR} \simeq 1.2 \cdot 10^7$ pump photons in the SMR. Injection of noise at the SMR frequency mimics the action of microwave shot noise which would provide the backaction in the quantum regime, and follows a similar procedure used by other researchers to demonstrate BAE [57]. While injecting noise, we recorded the spectrum around ω_{SMR}. The result appears as the purple trace in figure 6.7. Drifts of a few Hz in ω_{NR} required readjustment of the blue pump frequency, limiting our averaging time.

No motional sideband is distinguishable in the noise spectrum at ω_{SMR}. As described in section 3.4.3 the weak noise amplitude at $\omega_{SMR} \pm 2\omega_{NR}$ can mix with the pumps to drive the NR via backaction in both X_1 and X_2 quadratures. This deviation from ideal behavior will appear as motion in the X_1 quadrature and the ratio of the two quadrature amplitudes is given as a ratio of peak noise spectral densities $\frac{S_{X_2}}{S_{X_1}} = \frac{32\omega_{NR}^2}{\kappa^2} + 3$ (equation (3.35)). In our case we have $\frac{\omega_{NR}}{\kappa} = 11.3$, meaning we expect $\frac{S_{X_2}}{S_{X_1}} = 4 \cdot 10^3$. Our averaging time is too short to resolve the nonideal backaction motion or the thermal motion in the X_1 quadrature. Instead, we estimate the maximum possible sideband amplitude consistent with the random noise observed at ω_{SMR}. We take this to be the standard error of the measured noise power density within the noise bandwidth $\frac{\Gamma_{NR}}{4}$ of the NR. Multiplying this standard error by the noise bandwidth $\frac{\Gamma_{NR}}{4}$ yields an estimate of the minimum resolvable sideband power in the BAE measurement, denoted as P_{BAE}. A Lorentzian line having this area and linewidth Γ_{NR} is overlaid in black on figure 6.7.

To determine $\frac{S_{X_2}}{S_{X_1}}$ we would ideally like to directly measure the backaction-driven motion in the X_2 quadrature, recording the full "noise ellipse" of backaction-driven motion as demonstrated for instance by Marchese et al. [57]. However, the X_2 quadrature is by definition invisible to the BAE measurement. In the past, researchers developing BAE measurements with gravitational-wave antennas were able to add a separate transducer to their devices for independent measurement of X_2. [54] In our system, one option might be to apply a third microwave tone as a "probe" signal whose sidebands will be sensitive to both X_1 and X_2 while the two pump tones and noise injection are applied simultaneously.

Here we use a simpler technique of measuring the backaction due to a single pump tone that excites and detects both quadratures, and using this result to calculate the unseen X_2 backaction in the double pump BAE case. (For this calculation I rely on notes generously provided to my by A. Clerk. [84] [58]) After averaging

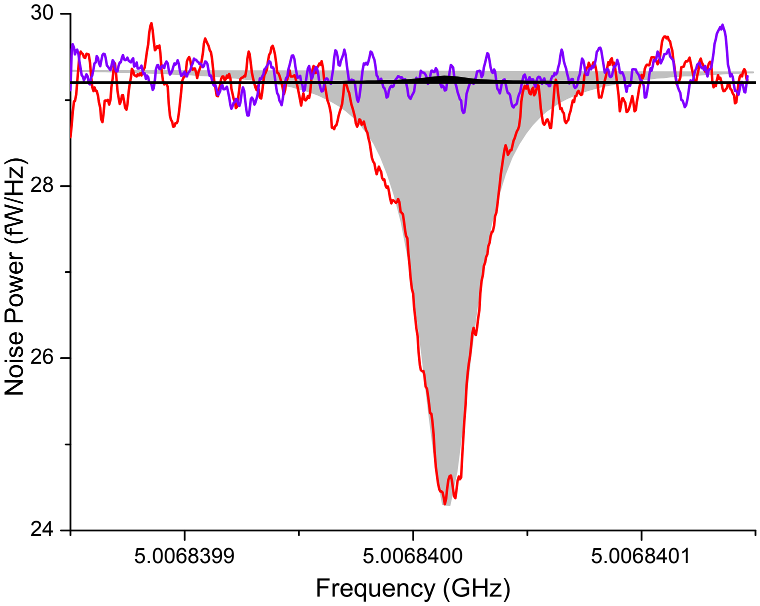

Figure 6.7: Demonstration of backaction evasion. Red line is motional sideband observed while pumping at $\omega_{RED} = \omega_{SMR} - \omega_{NR}$ and injecting noise to the SMR. Lorentzian fit (599 points, reduced $\chi^2 = 5.6 \times 10^{-32}$, adjusted $R^2 = 0.96$, gray shaded area) yields linewidth $\Gamma_{tot} = 2\pi \times (29 \pm 0.5)$ Hz and $P_{BA,red} =$ -234 ± 3 fW. Purple line is measured BAE noise spectrum measured while injecting same amplitude of white noise and pumping equally at $\omega_{RED} = \omega_{SMR} - \omega_{NR}$ and $\omega_{BLUE} = \omega_{SMR} + \omega_{NR}$. Black shaded area is a Lorentzian with amplitude equal to standard error of measured noise within span $\frac{\Gamma_{NR}}{4} = \frac{\pi}{2} \times (24.2 \pm 0.8)$ Hz. Area of this region is $P_{BAE} = 2.46$ fW, representing the maximum possible sideband power consistent with the measured noise. Pump conditions are identical to those in figure 6.6.

the spectrum in the BAE configuration for ∼1 hour, we shut off the blue pump and recorded the spectrum of the backaction given by a single red pump at the same power as in the BAE case and with the same level of noise injection. The backaction-driven single-pump spectrum appears as a red line in figure 6.7. We fit the peak area to find sideband power $P_{BA,red}$ and linewidth $\Gamma_{tot} = \Gamma_{NR} + \Gamma_{opt}$. The peak area is shaded in gray in the figure. A separate measurement using the double-pump non-BAE configuration permits us to measure the natural linewidth Γ_{NR} under identical conditions.

The expected noise spectra in the single-pump case with backaction-driven motion was discussed in section 3.3. Because the SMR "thermal" occupation $\bar{n}^T_{SMR}$ in this case is driven to such high levels by the injected noise, we may ignore the mechanical thermal-noise term proportional to $\bar{n}^T_{NR}$ in equation (3.21), leaving an expression that should correspond to the red curve in figure 6.7.

$$S_{N,out}(\delta) = gain \cdot \hbar\omega_{SMR} \cdot \frac{\kappa_{ext}}{\pi\kappa} \left(1 - \frac{\Gamma_{opt}(\Gamma_{NR} + \Gamma_{tot})}{4\delta^2 + \Gamma^2_{tot}}\right) \bar{n}^T_{SMR}$$

Integrating to find the apparent occupation due to backaction-driven motion in the single-pump case, corresponding to $P_{BA,red}$:

$$\bar{n}^{eff,BA}_{NR} = -\left(1 + \frac{\Gamma_{NR}}{\Gamma_{opt} + \Gamma_{NR}}\right) \bar{n}^T_{SMR} \tag{6.2}$$

From this expression and the measured value of $P_{BA,red}$, we would like to estimate the unseen backaction-driven occupation in the X_2 quadrature in the double-pump BAE case, $\bar{n}_{BA}$. Then this may be compared to the occupation of the X_1 quadrature, $\bar{n}_{X_1}$, as determined from the measured value P_{BAE}. A calculation of

$\bar{n}_{BA}$ has been done in reference [20], assuming that $\bar{n}^T_{SMR} = 0$, i.e. that the excitation of the SMR is limited to vacuum noise equaling $\frac{1}{2}$ microwave quantum. For large $\bar{n}^T_{SMR}$, that solution for $\bar{n}_{BA}$ may be adapted by multiplying it by $2\bar{n}^T_{SMR}$. [58] Taking into account that the power in the BAE case is double that in the single-pump case, $\bar{n}_{BA}$ may then be expressed in terms of the single-pump result $\bar{n}^{eff,BA}_{NR}$ (equation (6.2)). The ratio $\frac{S_{X_2}}{S_{X_1}}$ should equal $\frac{\bar{n}_{BA}}{\bar{n}_{X_1}}$. Expressing in terms of the measured sideband powers we have [58] [84]

$$\frac{S_{X_2}}{S_{X_1}} = 8\frac{\Gamma_{opt}}{\Gamma_{NR}}\frac{\Gamma_{tot}}{\Gamma_{tot}+\Gamma_{NR}}\frac{|P_{BA,red}|}{P_{BAE}} \tag{6.3}$$

For measured values $P_{BA,red} = -234$ fW, $P_{BAE} = 2.46$ fW, $\Gamma_{NR} = 2\pi \times 24$ Hz and $\Gamma_{tot} = 2\pi \times 29$ Hz , equation (6.3) yields $\frac{S_{X_2}}{S_{X_1}} = 82$. This represents a lower bound on the effectiveness of our backaction evading measurement, limited by averaging duration. The result compares favorably to other published demonstrations of backaction-evading single quadrature detection, such as in Ref. [57], which achieved $\frac{S_{X_2}}{S_{X_1}} = 26$. Further limitations on our BAE scheme due to the accompanying parametric amplification effect are discused in section 6.5.3.

6.5.3 Backaction evasion degraded by parametric amplification

In the BAE demonstration in section 6.5.3, the total pump power corresponded to $\bar{n}_{SMR} \simeq 1.2 \cdot 10^7$, which we can see from figure 6.5(a) and (c) should lead to an oscillating NR frequency shift of only ≤ 2 Hz. The resulting level of parametric amplification should degrade the BAE only slightly. To quantify the degradation in $\frac{S_{X_2}}{S_{X_1}}$ to be expected from a given level of parametric amplification, I rely on calculations helpfully provided by A. Clerk. [58] For an electrostatic frequency shift $\delta\omega_{NR} = \frac{1}{2}\frac{k_{EM}}{k} \cdot \omega_{NR}$ oscillating at frequency $2\omega_{NR}$, he finds that $\frac{S_{X_2}}{S_{X_1}}$ is limited to

$$\frac{S_{X_2}}{S_{X_1}} = \frac{1 - (\delta\omega_{NR}/\Gamma_{NR})^2}{(\delta\omega_{NR}/\Gamma_{NR})^2}$$

For the data in figure 6.7, given the measured $\Gamma_{NR} = 2\pi \cdot 24.2$ Hz and assuming $\delta\omega_{NR} = 2\pi \cdot 2$ Hz we find $\frac{S_{X_2}}{S_{X_1}}$ limited by parametric amplification to a factor of 145. This contrasts with the discussion in section in section 3.4.3 of limits to BAE due to mixing of noise from frequencies $\omega_{SMR} \pm 2\omega_{NR}$, which identified a limit $\frac{S_{X_2}}{S_{X_1}} = 4 \cdot 10^3$ for our device. This indicates that over nearly the whole regime of pump powers used in our measurements, our BAE efficiency is limited by parametric amplification rather than the more widely understood limits on BAE. This is likely to be the case for any attempt at BAE measurements using coupled SMR-NR devices. Nonetheless, in the measurement shown in section this limit still exceeded our ability to resolve $\frac{S_{X_2}}{S_{X_1}}$.

It is worth noting that when we applied higher pump powers where the parametric amplification should significantly degrade the BAE, and injected noise at ω_{SMR}, the resulting sideband spectrum appeared distinctly non-Lorentzian. Instead of a “dip” as in the red trace in figure 6.7, it appeared to be a “dip” for one portion of the linewidth, and a “peak” for another portion. From this I can surmise that the mixing of the backaction-driven X_1 and X_2 by parametric amplification results in a varying phase shift relative to the noise injected at ω_{SMR}. When we shifted the pump powers apart slightly in frequency, so that we pumped with microwave tones at $\omega_{SMR} - \omega_{NR}$ and $\omega_{SMR} + \omega_{NR} + \delta$, where δ was of the order of Γ_{NR}, this slight detuning appeared to suppress the effect of the parametric amplification on the BAE, recovering more of a flat noise spectrum. The exact behavior in these conditions merits further study.

6.6 Position sensitivity

Following the discussion in section 3.6 and conventions presented elsewhere [55], we would like to calculate the measured position uncertainty and compare it to quantum limits. For a measurement of thermal motion of the mechanical resonator, we expect the measured spectral density of motion to be a sum $S_x^{tot}(\omega) = S_x^{imp} + S_x^{BA} + S_x^{therm}(\omega)$. The first term reflects measurement uncertainty added by amplifier noise and vacuum fluctuations in the SMR. In our experiments the noise contributed by the HEMT amplifier dominates by about a factor of 30 over the the vacuum, or shot-noise, contribution. The second term reflects quantum backaction driving of the NR. As discussed in section 3.6, for shot-noise limited detection, at the standard quantum limit (SQL) the quantum backaction will contribute a mere $\frac{1}{4}$ quantum of mechanical energy to the NR motion. However, as we will show below, our position uncertainty never surpasses about 4 times Δx_{ZP} (neglecting the parametrically-amplified measurements in which the thermal noise is also amplified). Thus our coupling is barely adequate to reach the SQL even if our detection were shot-noise limited. On the other hand, in all of our measurements, thermal noise drives our NR to $\bar{n}_{NR} > 100$. Thus we will ignore the S_x^{BA}. We also assume that no other backaction force drives the NR. In these measurements we ensured that the SMR was not excited above its ground state, so there is no backaction driving as described in sections 3.3 and 6.3. Here we also neglect other effects of the measurement on the NR amplitude, such as thermal heating. Although we saw some evidence of pump-power-dependent thermal heating at the fridge base temperature (see figure 5.4 and discussions in section 6.2), at 142 mK we see no such effects, as discussed in section 6.8. In any case themal heating would appear merely as an increase in $S_x^{therm}(\omega)$. Thus in calculating the measurement uncertainty we assume that within the regime in which we are operating, the additive contribution of the amplifier noise tells the whole story.

The total measured noise spectral density at frequencies near the SMR resonance should be the sum of two contributions corresponding respectively to $S_x^{therm}(\omega)$ and S_x^{imp}: the noise due to the mechanical sideband, $S_{sideb}(\omega)$, and a fixed-amplitude, frequency-independent background noise due to the amplifier, S_{bgd}.

$$S(\omega) = S_{sideb}(\omega) + S_{bgd} \tag{6.4}$$

The thermal calibrations and expressions for P_{sideb}, equations (2.53) and (5.4), allow us to readily calculate the position noise spectral density (in units of m^2/Hz) of the measured NR amplitude [4]. We use the constant cal(P_{out}) determined from our thermal calibration data (see section 5.5) to relate mechanical amplitude to the measured power spectrum at frequencies near ω_{NR}, divided by the transmitted pump power P_{out}. (Note that we use throughout this work a convention of single-sided spectral densities.) To find the thermal excitation of the NR in terms of a noise spectral density we take

$$S_x^{therm}(\omega) = (k_B/k)\left(S_{sideb}(\omega)/P_{out}\right)/\mathrm{cal}(P_{out}) \tag{6.5}$$

The additive amplifier noise S_{bgd} contributes an uncertainty S_x^{imp} to our measurement of the NR position S_x. Expressed as a position noise spectral density (in units of m^2/Hz):

$$S_x^{imp} = (k_B/k)\left(S_{bgd}/P_{out}\right)/\mathrm{cal}(P_{out}) \tag{6.6}$$

In figure 6.2, I show $S_x(\omega) = S_x^{imp} + S_x^{therm}(\omega)$ found from measured sideband values $S_{bgd} + S_{sideb}(\omega)$. Figure 6.4 shows the case where excitation of the SMR $\bar{n}_{SMR}^T$ contributes additionally to S_{bgd} and therefor to S_x^{imp}, demonstrating how excitation of the SMR not only causes the measurement to drive the NR with backaction but also degrades the position sensitivity.

From S_x^{imp}, we can calculate the position uncertainty Δx in our measurement of the motion. This method is similar to the methods described in past work [75] and is equivalent to comparing additive noise with the mechanical response amplitude. [73] For a NR having linewidth $\Gamma_{tot}/2\pi$, this is given by the total position noise attributable to S_x^{imp} within the effective noise bandwidth of the NR:

$$\Delta x = \sqrt{S_x^{imp} \cdot \frac{\Gamma_{tot}}{4}} \tag{6.7}$$

Measured values of Δx calculated in this way from S_{bgd} appear for all pump configurations in figure 6.8. (The dataset is the same as the one appearing in figure 6.1.) The values of Δx are expressed in real units as well as in multiples of the zero point motion Δx_{ZP}. From equation (6.6) we expect the precision to

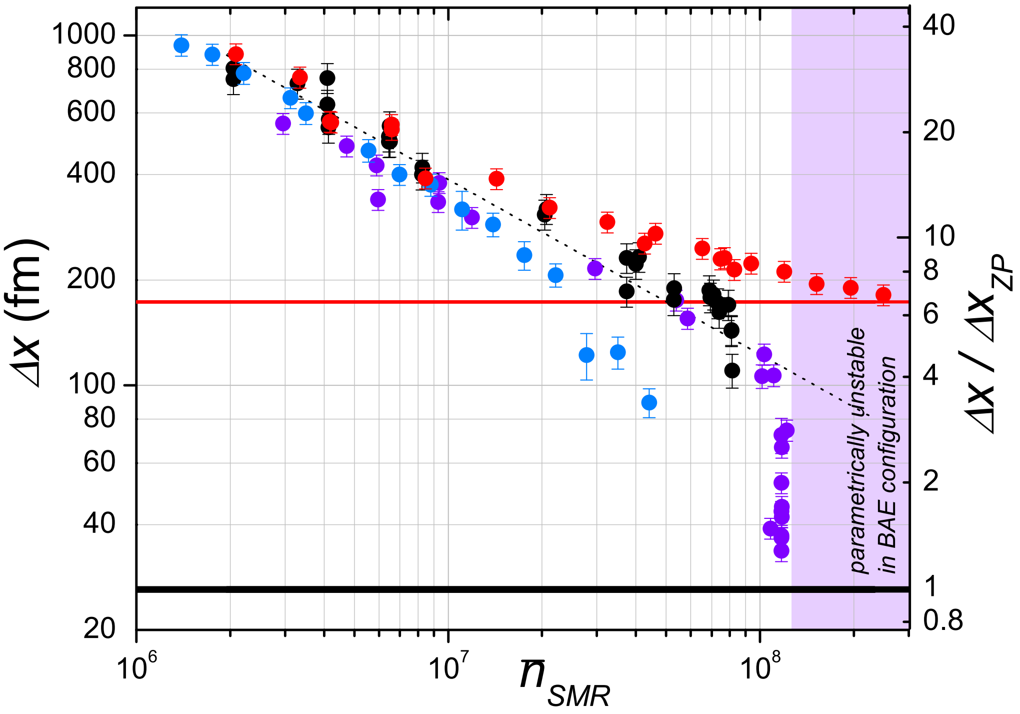

Figure 6.8: Measured position uncertainty Δx vs. SMR occupation. Same dataset as used in Fig. 6.1. Red-detuned pumping (red points) $\omega_{red} = \omega_{SMR} - \omega_{NR}$. Blue-detuned pumping (blue points) $\omega_{blue} = \omega_{SMR} + \omega_{NR}$. BAE pump condition (purple points) $\omega_{red} = \omega_{SMR} - \omega_{NR}$ and $\omega_{blue} = \omega_{SMR} + \omega_{NR}$. Balanced pump, non-BAE condition (black points) $\omega_{red} = \omega_{SMR} - \omega_{NR}$ and $\omega_{blue} = \omega_{SMR} + \omega_{NR} + 2\pi \cdot 600\text{Hz}$. The horizontal red line shows the limiting sensitivity for a single pump tone. The slanted black dotted line shows the expected sensitivity proportional to $\frac{1}{\sqrt{\bar{n}_{SMR}}}$ if linewidth Γ_{tot} is insensitive to pump power and equal to only the natural linewidth Γ_{NR} of the nanoresonator. Shaded region is inaccessible to BAE due to parametric instability.

improve inversely with pump power, i.e. inversely with the coupling of NR to the readout. Thus we expect Δx to scale inversely with the square root of pump power. At low pump powers, this behavior is followed by the measurements in all pump configurations. Yet from equation (6.7) we see that the contribution of additive noise to our position sensitivity is critically dependent on the NR linewidth Γ_{tot}. We find that at high pump powers the narrow linewidths possible in the high-stress SiN nanoresonator enable Δx to approach Δx_{ZP}.

The four pump configurations therefore present four distinct behaviors of position sensitivity as power is increased, because of the effects on linewidth demonstrated in figure 6.1. The double-pump, non-BAE configuration is the most straightforward. Because the pumps are balanced, there is no backaction damping, thus the natural linewidth of the NR is maintained independent of pump power, $\Gamma_{tot} = \Gamma_{NR}$, yet the measurement is sensitive to both quadratures of mechanical motion. In this regard it is similar to the technique of detecting motion by pumping at ω_{SMR}, employed by other researchers. [17] [72] [45] The best sensitivity achieved in this measurement is roughly $5 \cdot \Delta x_{ZP}$, or ~ 7 times the SQL level, at a cavity pump occupation of $8 \cdot 10^7$. We would expect that if the product $\mathrm{cal}(P_{out}) \cdot P_{out}$ could be raised a factor of 50, the measurement imprecision due to additive noise would reach the SQL. Given that the additive noise of our amplifier is about 30 times above shot noise, for such a measurement we would expect shot-noise backaction to add on the order of 10 mechanical quanta to the NR motion.

In comparison, the BAE pump configuration similarly preserves $\Gamma_{tot} = \Gamma_{NR}$, but this measurement, as described in sections 3.4 and 6.5, will introduce backaction only to quadrature X_2 while measuring only X_1. Thus the uncertainty is really an uncertainty in only the measured quadrature, ΔX_1. The best sensitivity achieved with backaction-evading measurement is seen in figure 6.8 to be roughly $4 \cdot \Delta x_{ZP}$ at $\bar{n}_{SMR} = 10^8$. At higher pump powers, where the sensitivity of the double-pump, non-BAE measurement would degrade due to shot-noise backaction, the BAE measurement should ideally exhibit no such limits on its sensitivity. This level of $\Delta X_1 = 4 \cdot \Delta x_{ZP}$ is as far as I'm aware the best sensitivity achieved to date in a BAE measurement. Other published results report uncertainties that are orders of magnitude greater. [54] It is also very interesting to note that this uncertainty derives entirely from the noise added by the amplifier, with a noise temperature of $T_N = 3.56$ K, or 14.8 quanta at the measurement frequency of $\omega_{SMR} = 2\pi \cdot 5.00684$ GHz. If the amplifier noise were eliminated, we must consider only the $\frac{1}{2}$ quantum, i.e. $\frac{1}{2}\hbar\omega_{SMR} = \frac{1}{2}k_B \cdot 240$ mK, of noise contributed by vacuum fluctuations of the microwave field. This would reduce ΔX_1 a factor of 5.4, leading to ΔX_1 below Δx_{ZP}. This demonstrates that our coupling and measurement strength in the BAE configuration is capable of generating a conditionally squeezed state, as discussed in sections 3.4.2 and 3.4.4. To my knowledge this is the first time such a measurement has been shown.

In the BAE configuration at slightly higher pump powers, however, the parametric amplification effect described in section 3.5 becomes significant. This has both benefits and drawbacks. Because the parametric amplification favors a phase $\frac{\pi}{4}$ away from X_1 and X_2, it will effectively combine the two quadratures, destroying the BAE effect. However, the mechanical preamplification adds no noise to the measurement, and also dramatically narrows the NR linewidth, making our measurement less sensitive to the additive amplifier noise. Because small fluctuations in ω_{NR} cause large variations in the parametric amplification, and a slight increase in the parametric amplification could cause the NR to self-oscillate, this effect was challenging to control. However, linewidths below 3 Hz were readily achievable and as low as 2.1 Hz were possible. In a measurement at SMR occupation $\bar{n}_{SMR} = 1.1 \cdot 10^8$, we found $\Gamma_{tot}/2\pi = 2.1$ Hz, reaching our lowest value of position uncertainty $\Delta x = 1.3 \cdot \Delta x_{ZP}$. The parametrically-amplified thermal noise spectrum appears in figure 6.9, along with a Lorentzian fit having linewidth $\Gamma_{tot}/2\pi = 2.1$ Hz. It is important to note that, even though the parametric amplification narrows the linewidth, reducing the effect of S_x^{imp}, it also amplifies the thermal motion by the same amount. Thus even though it helps approach the SQL, it makes it more difficult to observe shot-noise backaction. The parametric amplification thus does not improve our ability to achieve true quantum-limited measurement. This technique could, however, be very useful in detecting the thermal noise or the response to small forces in circumstances where the additive noise dominated the measurement.

The blue pump measurements appearing in figure 6.8 exhibit a similar behavior to the parametric amplification effect, narrowing the linewidth while amplifying the thermal noise. In this case however, the NR motion is driven to self-oscillating levels at pump powers too low to reliably achieve Δx as close to Δx_{ZP}. The red pump configuration presents another interesting case. This type of measurement has been commonly used in prototype gravitational-wave antennas. [57] [54] The limiting case for a single-pump measurement is discussed in section 3.6 as reaching Δx_{ZP}

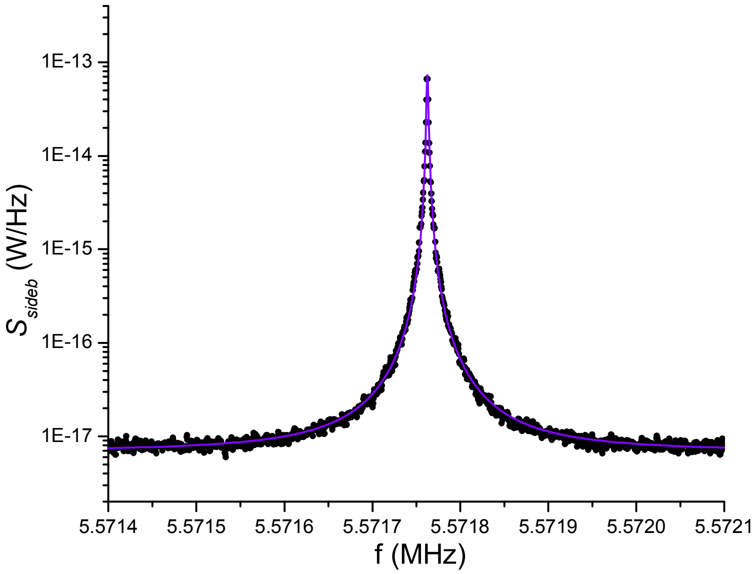

Figure 6.9: Highest-achieved mechanically-preamplified thermal noise of NR. Double-pump configuration, pumps at ω_{SMR} +/- ω_{NR}. Fridge temperature 142 mK, mechanically-amplified mode temperature 2.26 K, linewidth 2.1 Hz. (Here pump frequency is subtracted from horizontal axis so that the response is centered around f_{NR}). The measurement in this figure also appears in fig 6.1 (c) as the point with lowest Γ_{tot}, in fig 6.1 (d) as the point with largest $\bar{n}_{NR}$, and in fig 6.8 as the point of lowest Δx.

only in the limit of infinitely strong coupling. It is instructive to calculate how close we expect the measurement to reach and compare it to the measured limits appearing in figure 6.8. Combining equations 6.6 and 6.7, and using the definition $\Delta x_{ZP} = \sqrt{\frac{\hbar}{2m\omega_{NR}}} = \sqrt{\frac{\hbar\omega_{NR}}{2k}}$, we have

$$\left(\frac{\Delta x}{\Delta x_{ZP}}\right)^2 = \frac{k_B}{\hbar\omega_{NR}} \cdot \frac{S_{bgd}}{P_{out} \cdot \mathrm{cal}(P_{out})} \cdot \frac{\Gamma_{tot}}{2}$$

As discussed in section 5.4, S_{bgd} equals $k_B T_n \cdot gain_{amp}$, where $gain_{amp}$ is the total gain from the HEMT amp input to our spectrum analyzer, as opposed to the total *gain* which also includes the losses between the sample and amplifier. We can also incorporate the definition from equations (5.2) and (5.4) of $\mathrm{cal}(P_{out}) = \left(\frac{\partial\omega_{SMR}}{\partial x}\frac{1}{\kappa}\right)^2 \cdot 2\frac{k_B}{k} \cdot \frac{gain(\omega_{SMR})}{gain(\omega_{pump})}$, to find

$$\left(\frac{\Delta x}{\Delta x_{ZP}}\right)^2 = \frac{k \cdot k_B T_n}{\hbar\omega_{NR}} \cdot \frac{gain_{amp}(\omega_{SMR})}{gain(\omega_{SMR})} \cdot \frac{gain(\omega_{pump})}{P_{out}} \cdot \left(\frac{\partial\omega_{SMR}}{\partial x}\frac{1}{\kappa}\right)^{-2} \cdot \frac{\Gamma_{tot}}{4}$$

We can reduce this further by expressing the amplifier noise in terms of $T_n = \bar{n}_{amp} \cdot \frac{\hbar\omega_{SMR}}{k_B}$, and by using equation (2.34) to substitute for $\frac{gain(\omega_{pump})}{P_{out}}$:

$$\left(\frac{\Delta x}{\Delta x_{ZP}}\right)^2 = \frac{\bar{n}_{amp}}{(\Delta x_{ZP})^2} \cdot \frac{gain_{amp}(\omega_{SMR})}{gain(\omega_{SMR})} \cdot \frac{\kappa}{\kappa_{ext}} \cdot \left(\frac{\partial\omega_{SMR}}{\partial x}\right)^{-2} \cdot \frac{\kappa}{\bar{n}_{SMR}} \cdot \frac{\Gamma_{tot}}{4} \qquad (6.8)$$

In the limiting case of high pump powers, $\Gamma_{opt} \gg \Gamma_{NR}$, thus we may take $\Gamma_{tot} = \Gamma_{opt}$. Using expression (3.6) we have the limiting value

$$\left(\frac{\Delta x}{\Delta x_{ZP}}\right)^2 = \bar{n}_{amp} \cdot \frac{gain_{amp}(\omega_{SMR})}{gain(\omega_{SMR})} \cdot \frac{\kappa}{\kappa_{ext}} \qquad (6.9)$$

Note that the limiting precision is explicitly dependent on the losses between the sample and amplifier, but for the ideal case of zero losses and a quantum-limited amplifier $\bar{n}_{amp} = \frac{1}{2}$, this expression reduces to the theoretical expression discussed in section 3.6. For our HEMT amplifier having $T_n = 3.56 \pm 1$ K at 5 GHz, we have $\bar{n}_{amp} = 14.8 \pm 4.2$. The loss between sample and amplifier is also estimated (see section 4.1) to be $\frac{gain_{amp}(\omega_{SMR})}{gain(\omega_{SMR})} = 1.5 \pm 1$ dB. From these values, and our best estimates of κ_{ext}, and expression (6.9) we find a limiting value of $\frac{\Delta x}{\Delta x_{ZP}} = 5.8 \pm 1.5$. For comparison, we take the red-pump data in figure 6.8 and fit it to 1 over the pump power plus a constant: $\left(\frac{\Delta x}{\Delta x_{ZP}}\right)^2 = \frac{A}{\bar{n}_{SMR}} + B$. We find an excellent fit to this expression, with the fit parameter $B = 44.4 \pm 2.5$ yielding a limiting value of $\frac{\Delta x}{\Delta x_{ZP}} = \sqrt{B} = 6.7 \pm 0.2$. This value is shown in figure 6.8 as a horizontal red line. The theoretical and fit values are thus in good agreement within uncertainty. Or to look at it another way, equating expression (6.9) to the fit value of B yields $\bar{n}_{amp} = 19.3 \pm 8.4$, or $T_n = 4.6 \pm 2.0$ K.

6.7 Force sensitivity

We can also determine the force sensitivity of the device, as described in reference [85], which reports the best published sensitivity of $F_{min} = 0.8\ \mathrm{aN}/\sqrt{\mathrm{Hz}}$, with a closely matching sensitivity also reported in Ref. [3]. For a resonator of mechanical linewidth Γ_{tot}, the force sensitivity F_{min} represents the driving force that would produce an RMS mechanical amplitude equal to the apparent measured amplitude of the NR due to both additive noise and thermally-driven motion of the NR. Or in other words, what level of force driving the NR would produce a signal-to-noise ratio of one with respect to measurement noise and thermal noise? The measurement bandwidth is taken to be the noise bandwidth $\frac{\Gamma_{NR}}{4}$ of the NR. F_{min} is thus given (in

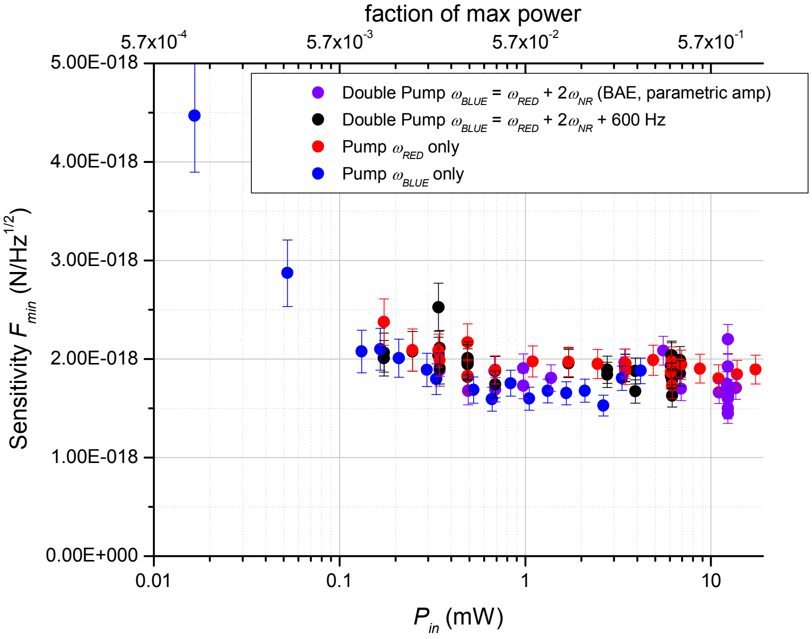

Figure 6.10: Force sensitivity vs. pump power, at fridge temperature of 142 mK. Same dataset as in figures 6.1 and 6.8.

units of $\mathrm{N}/\sqrt{\mathrm{Hz}}$) by

$$F_{min} = \frac{k}{\omega_{NR}}\sqrt{\Gamma_{tot}\cdot\left(S_x^{imp}\Gamma_{tot} + \frac{4k_B T_{NR}}{k}\right)} \tag{6.10}$$

It is evident from expression (6.10) that if $\frac{4k_B T_{NR}}{k} \gg S_x^{imp}\Gamma_{tot}$ then the thermal noise dominates, and the additive noise may be neglected. It is also evident that in this limit such processes as either positive or negative optical damping, or parametric amplification have negligible effect on the detectable force, because in the limiting cases of these processes T_{NR} scales inversely with Γ_{tot}. Figure 6.10 shows the force sensitivity F_{min} calculated for measurements at a temperature of 142 mK for all pump configurations. At high pump powers, we have sufficient sensitivity that in equation (6.10) the thermal noise of the NR dominates over S_x^{imp}. At this

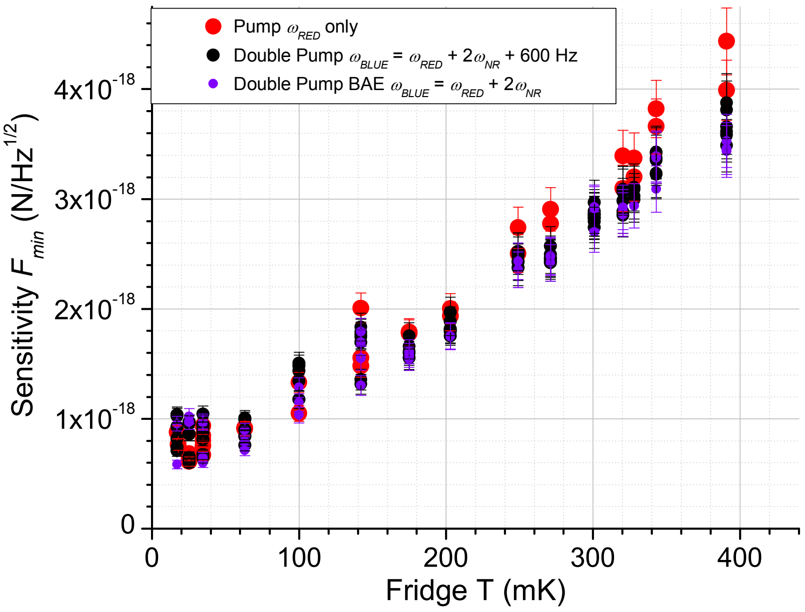

Figure 6.11: Force sensitivity vs. fridge temperature. Same dataset as thermal calibration (figure 5.6).

temperature we reliably achieve a force sensitivity of $1.7 \cdot 10^{-18} N \Big/ \sqrt{Hz}$. Figure 6.11 shows force sensitivity vs fridge temperature, calculated using equation (6.10) from the same dataset used in our thermal calibration (figure 5.6). At the lowest temperature at which the sample thermalized to the fridge (63 mK), we reliably achieved sensitivity of $8 \cdot 10^{-19} N \Big/ \sqrt{Hz}$ at high pump powers.

At our lowest fridge temperature of ∼17mK, we occasionally observed a NR mode temperature of 46mK and linewidth of 8 Hz, yielding a force sensitivity of $6 \cdot 10^{-19} N \Big/ \sqrt{Hz}$. Each of our measurements of T_{NR} is made simultaneously with a measurement of Γ_{tot} by measuring and fitting the thermal noise of the NR, which may tend to overestimate Γ_{tot} because of drifts in the NR frequency during the averaging. Another way to consider it is to measure Γ_{tot} separately using a more rapid measurement under the same conditions. This was the technique used by Mamin et al. [85]. We have made separate measurements of Γ_{tot} using a time-domain ring-down technique, and found $\Gamma_{tot} = 2\pi \times 1.9$ Hz at 50 mK and $\Gamma_{tot} = 2\pi \times 3.2$ Hz at 75 mK. Taking $T_{NR} = 60$ mK and $\Gamma_{tot} = 2\pi \times 3$ Hz and assuming sufficient pump power to overcome S_x^{imp} we find $F_{min} = 0.4$ aN/$\sqrt{\text{Hz}}$, an improvement on the best published results.

6.8 Approach to quantum limits on $S_x \cdot S_F$

The Heisenberg uncertainty principle $\Delta x \Delta p \geq \frac{\hbar}{2}$ may be applied to the act of position measurement as $\Delta x_{meas} \Delta p_{perturb} \geq \frac{\hbar}{2}$, where Δx_{meas} is the uncertainty in the measurement and $\Delta p_{perturb}$ is the change in the momentum due to measurement backaction. [55] This relation in turn may be re-expressed as a limit on the product of the measurement precision S_x, and the resulting back-action force noise S_F. For single-sided noise spectral densities, the limit is $S_x S_F \geq \hbar^2$ [55]. At sufficiently high coupling strengths of the measuring system to the measured mechanical motion, the shot noise of the microwave pump field will generate the back-action force noise S_F to enforce this limit. In our system, the coupling is most easily increased by increasing the pump power. The measurement imprecision decreases with increasing pump power as shown in equation (6.6). In our system, in the range of accessible pump powers, we expect the shot-noise S_F to drive the NR only very weakly, only to amplitudes barely approaching one quantum of NR energy. In practice, however, classical effects may produce force noise stronger than the shot-noise S_F. Any such effects that also increase with increasing pump power will mimic and obscure the quantum back-action. In our measurements we avoid one important effect by making sure that the SMR is not excited above its ground state $\bar{n}^T_{SMR} = 0$; thus the classical backaction noise driving (described in sections 3.3 and 3.4.3) may be neglected. However, other classical effects such as thermal heating of the NR can also drive the NR to increasing amplitudes as pump power is increased. We treat this "classical backaction" as adding to the backaction force noise S_F, and want to set limits on the magnitude of this force. We may then estimate how closely such classical backaction would permit us to observe quantum-mechanical contributions to S_F.

To distinguish the classical contribution to S_F, we look for evidence of a white force noise which drives the mechanics to a mode temperature $T_{NR(BA)}$ additional to the average thermal bath temperature. To be a signature of backaction, $T_{NR(BA)}$ should also increase with increasing pump power. As a force F at the resonant frequency will drive a mechanical resonator to an amplitude FQ/k, a force noise S_F drives a resonator of linewidth Γ to mean-squared motion $\langle x^2 \rangle = S_F \cdot \left(\frac{Q}{k}\right)^2 \cdot \frac{\Gamma}{4}$, and therefore we express

$$\begin{aligned} T_{NR} &= T_{NR(therm)} + T_{NR(BA)} \\ &= T_{NR(therm)} + \frac{S_F(P_{pump})}{4mk_B\Gamma_{NR}} \end{aligned} \tag{6.11}$$

where S_F has units of N^2/Hz. Note that if we express $T_{NR(BA)} = \hbar\omega_{NR} \cdot \bar{n}_{BA}$ and use equation (3.10) to express S_x in terms of an effective imprecision occupation

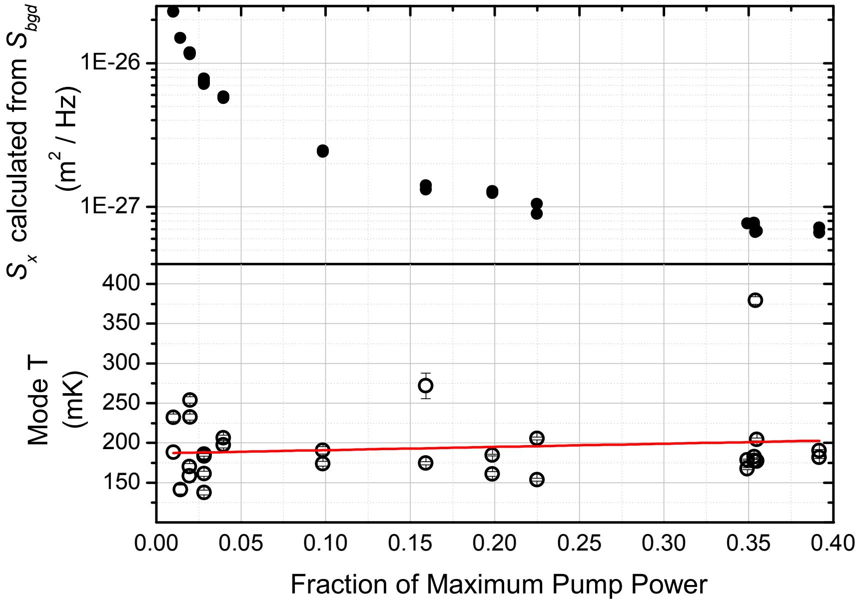

Figure 6.12: Position noise due to additive amplifier noise, and mode temperature, plotted against pump power, when pumping with two tones at $\omega_{SMR} - \omega_{NR}$ and $\omega_{SMR} + \omega_{NR} + 2\pi \times 600\text{Hz}$. Data in lower panel also appears as black points in figure 6.1 (d). Red line is a linear fit to NR mode T as a function of pump power, consistent with no excess backaction in the measurement.

$S_x = \frac{4}{\Gamma_{NR}} \cdot 2\bar{n}_{imp}(\Delta x_{ZP})^2$, we have $S_x S_F = 16\hbar^2 \cdot \bar{n}_{imp} \cdot \bar{n}_{BA}$, thus by the uncertainty relation we must have $\sqrt{\bar{n}_{imp} \cdot \bar{n}_{BA}} \geq \frac{1}{4}$. The increase in mode temperature in equation (6.11) is most easily distinguished when T_{NR} is otherwise expected to be independent of pump power. Naik et al. [3] identified $T_{NR(BA)}$ and therefore S_F for a superconducting SET coupled to a NR, by reducing $T_{NR(therm)}$ to negligible levels by lowering their fridge temperature. Regal et al. [17] did something similar with a coupled SMR-NR system, pumping their SMR on-resonance to avoid backaction damping effects while operating at the lowest fridge temperature and examining the dependence of their NR mode temperature on microwave pump power. Here we wish to avoid the behavior at our lowest fridge temperatures in which an unidentified non-thermal force-noise drives the NR to amplitudes far in excess of thermal noise (section 5.5). Instead we use Eq. (6.11) to estimate S_F as a function of pump power based on measurements at 142 mK.

To avoid any backaction cooling or parametric amplification effects, we apply equal microwave pumps at $\omega_{SMR} - \omega_{NR}$ and $\omega_{SMR} + \omega_{NR} + 2\pi \times 600\text{Hz}$. This data is included in figure 6.1 (d) and also appears in figure 6.12, with a linear regression fit line attempting to determine a trend in the mode temperature as a function of pump power. The fit yields intercept 187 ± 12 mK, slope 40.4 ± 58.7 mK per normalized power of 1, with adjusted $R^2 = -0.02$. Thus at the highest pump power in this dataset, the fit finds $T_{NR(BA)} = 14 \pm 21\text{mK}$. The large uncertainty in the fit means that the data is consistent with no backaction driving of the NR at all. Nonetheless, we can employ the fit value to conservatively estimate an upper bound on classical backaction contributions to S_F. From $T_{NR(BA)} = 14\text{mK}$ we find

$S_F = 5.3 \times 10^{-37}\mathrm{N}^2/\mathrm{Hz}$. At the same pump power, the additive amplifier noise yields position uncertainty $S_x = S_x^{imp} = 6.7 \times 10^{-28}\mathrm{m}^2/\mathrm{Hz}$. From this we find $\sqrt{S_x S_F} = 9.2 \cdot 10^{-33}\mathrm{J} \cdot \mathrm{s}$, or $\sim 90\hbar$. This represents an upper bound on our approach to the quantum limit $S_x S_F \geq \hbar^2$. This calculation of $S_x S_F$ pertains only to this particular pump configuration, i.e. when the SMR is driven with both red and blue microwave pumps so as to balance up- and down-conversion but without BAE.

However, this estimate of the classical contribution to S_F should be relevant to any pump configuration, because it is presumed to result from thermal heating or other parasitic processes that depend directly on pump power. Further evidence for this conclusion is seen in the backaction cooling data (red and blue points in figure 6.1 (a) and (b)) which fits well to the theory based on optical damping and detailed balance equation (equations (3.3) and (3.6)). Excess thermal heating of the NR would likely cause the fit of $\bar{n}_{NR}$ to deviate from theory.

Chapter 7

Conclusions

The work presented in this dissertation represents a first demonstration in our research group of high-precision position measurement and backaction cooling in a coupled SMR-NR system. The close agreement of the backaction cooling with theory (figure 6.1 (a) and (b)) shows that the system is well understood. Moreover, we have for the first time demonstrated backaction-evading single-quadrature detection in a nanomechanical system. With this technique we demonstrated position uncertainty only 4 times above the zero-point motion of the NR. Because this uncertainty is contributed largely by the additive noise of our amplifier, our device actually achieved coupling strengths that could permit the generation of a conditionally squeezed state. Ultimately our ability to achieve lower position uncertainties in continuous position measurement, and our ability to perform better backaction cooling, is limited by the poor power-handling ability of the SMR sample that we used (figure 5.2). This problem is readily amenable to engineering solutions involving improved device fabrication. Our ability to achieve better position sensitivity in the BAE measurement is limited by the parametric amplification behavior arising in this configuration. This limitation has not previously been explored in the experimental literature.

Since the measurements in this dissertation were completed, the research group has advanced rapidly to even more exciting results. Building on the techniques proven in the work presented here, we made four major improvements to the device: 1) fabrication of the SMR from Nb rather than Al, for improved power handling, 2) preventing the capacitive-division between gate and SMR (section 4.3 and figure 4.10), for improved coupling, 3) raising the SMR frequency to 7.5 GHz, and 4) increasing the impedance Z_0' of the CPW forming the SMR, in order to reduce its capacitance, for improved coupling (equation (2.40)).

The results were just as we expected, achieving a dramatically improved coupling of $\frac{\partial \omega_{SMR}}{\partial x} = 2\pi \cdot 84$ kHz / nm, and backaction cooling to $\bar{n}_{NR} < 4$ [86]. Our understanding of backaction-driving of the NR during red pump measurements, described in this dissertation (sections 3.3 and 6.3), was essential to the later work because the later device exhibited excitation of the SMR during the cooling measurements. Work is ongoing to improve the devices yet further. With modest improvements in coupling and the elimination of the unwanted excitation of the SMR, it appears that cooling to the ground state, demonstrating additive noise uncertainties below the SQL, single-quadrature backaction-evading measurements with uncertainty below zero-point motion, and generation of squeezed states, are all within reach.

I should also mention here a related project that I participated in actively for several years, but which is not discussed in this dissertation. The group led by Markus Asplemeyer at the Institute for Quantum Optics and Quantum Information in Vienna, Austria, has been studying backaction cooling and related phenomena in micromechanical resonators coupled to optical cavities - the identical concept to the system appearing in this dissertation, but in a different regime, with different techniques [38] [87] [42]. The optical system offers advantages and disadvantages over a microwave system. Lasers and photodiodes have far lower noise than sources and amplifiers in the microwave regime. The optical cavity is not susceptible to thermal occupation as the SMR is, but it is a free space cavity many thousands of wavelengths long, which requires complicated alignment and locking techniques. Although the optical system allows easy prototyping at room temperature, these experiments are just beginning to be done at low temperatures and not yet at millikelvin temperatures. I assisted with design and fabrication of the first and second generations of device used in these measurements. The challenge was to make > 1 MHz mechanical resonators having both high Q and high optical reflectivity. This work recently succeeded in using radiation-pressure optical damping to cool the motion of a $100\mu\text{m} \times 50\mu\text{m} \times 1\mu\text{m}$, 945 kHz mechanical resonator to a factor of 32 above the quantum ground state, to date the best published result of such a technique [42]. In terms of the possibilities for demonstrating quantum behavior, this optical system is as promising as the microwave and nanomechanics system, and I am pleased to have contributed to its development.

Bibliography

[1] William Marshall, Christoph Simon, Roger Penrose, and Dik Bouwmeester. Towards quantum superpositions of a mirror. *Phys. Rev. Lett.*, 91(13):130401, Sep 2003.

[2] Keith C. Schwab and Michael L. Roukes. Putting mechanics into quantum mechanics. *Physics Today*, 58(7):36–42, 2005.

[3] A. Naik, O. Buu, M. D. LaHaye, A. D. Armour, A. A. Clerk, M. P. Blencowe, and K. C. Schwab. Cooling a nanomechanical resonator with quantum back-action. *Nature*, 443:193–196, September 2006.

[4] M. D. LaHaye, O. Buu, B. Camarota, and K. C. Schwab. Approaching the quantum limit of a nanomechanical resonator. *Science*, 304:74–77, April 2004.

[5] Peter K. Day, Henry G. LeDuc, Benjamin A. Mazin, Anastasios Vayonakis, and Jonas Zmuidzinas. A broadband superconducting detector suitable for use in large arrays. *Nature*, 425:817–821, October 2003.

[6] Serge Haroche and Daniel Kleppner. Cavity quantum electrodynamics. *Physics Today*, pages 24–30, January 1989.

[7] A. Wallraff, D. I. Schuster, A. Blais, L. Frunzio, R.-S. Huang, J. Majer, S. Kumar, S. M. Girvin, and R. J. Schoelkopf. Strong coupling of a single photon to a superconducting qubit using circuit quantum electrodynamics. *Nature*, 431:162–167, September 2004.

[8] David M. Pozar. *Microwave Engineering*. John Wiley and Sons, third edition, 2005.

[9] T. Van Duzer and C. W. Turner. *Principles of Superconductive Devices and Circuits*. Elsevier, New York, 1981.

[10] Terry P. Orlando and Kevin A. Delin. *Foundations of Applied Superconductivity*. Addison-Wesley, Reading, MA, 1991.

[11] A.D. OConnell, M. Ansmann, R.C. Bialczak, M. Hofheinz, N. Katz, E. Lucero, C. McKenney, M. Neeley, H. Wang, E.M. Weig, A.N. Cleland, and J.M. Martinis. Microwave dielectric loss at single photon energies and millikelvin temperatures. *Applied Physics Letters*, 92(11):112903 – 1, 2008.

[12] G. Hammer, S. Wuensch, M. Roesch, K. Ilin, E. Crocoll, and M. Siegel. Superconducting coplanar waveguide resonators for detector applications. *Supercond. Sci. Technol.*, 20:S408, October 2007.

[13] K. C. Gupta, Ramesh Garg, and I. J. Bahl. *Microstrip Lines and Slotlines*. Artech House, Dedham, MA, 1979.

[14] Rainee N. Simons. *Coplanar Waveguide Circuits, Components, and Systems.* John Wiley and Sons, New York, 2001.

[15] Benjamin A. Mazin. *Microwave Kinetic Inductance Detectors.* PhD thesis, California Institute of Technology, 2004.

[16] G. Benz, T.A. Scherer, M. Neuhaus, and W. Jutzi. Quality factors of coplanar niobium resonators on $LaAlO_3$ substrates with different cross-sectional geometries. *Cryogenics*, 38(6):697700, 1998.

[17] C. A. Regal, J. D. Teufel, and K. W. Lehnert. Measuring nanomechanical motion with a microwave cavity interferometer. *Nature Physics*, 4:555–560, May 2008.

[18] J.B. Hertzberg, T. Rocheleau, T. Ndukum, M. Savva, A.A. Clerk, and K.C. Schwab. Back-action evading measurements of nanomechanical motion. *arXiv:0906.0967v1*, 2009. (unpublished).

[19] F. Marquardt, J. P. Chen, A. A. Clerk, and S. M. Girvin. Quantum theory of cavity-assisted sideband cooling of mechanical motion. *Phys. Rev. Lett.*, 99:093902, August 2007.

[20] A A Clerk, F Marquardt, and K Jacobs. Back-action evasion and squeezing of a mechanical resonator using a cavity detector. *New Journal of Physics*, 10(9):095010 (20pp), 2008.

[21] C. Monroe, D. M. Meekhof, B. E. King, S. R. Jefferts, W. M. Itano, D. J. Wineland, and P. Gould. Resolved-sideband raman cooling of a bound atom to the 3D zero-point energy. *Phys. Rev. Lett.*, 75(22):4011–4014, Nov 1995.

[22] F. Diedrich, J. C. Bergquist, Wayne M. Itano, and D. J. Wineland. Laser cooling to the zero-point energy of motion. *Phys. Rev. Lett.*, 62(4):403–406, Jan 1989.

[23] D. J. Wineland and H. G. Dehmelt. Principles of the stored ion calorimeter. *Journal of Applied Physics*, 46(2):919–930, 1975.

[24] R. Van Dyck, P. Ekstrom, and H. Dehmelt. Axial, magnetron, cyclotron and spin-cyclotron-beat frequencies measured on single electron almost at rest in free space (geonium). *Nature*, 262:776, August 1976.

[25] D. J. Wineland and Wayne M. Itano. Laser cooling of atoms. *Phys. Rev. A*, 20(4):1521–1540, Oct 1979.

[26] D. Kielpinski, C. Monroe, and D. J. Wineland. Architecture for a large-scale ion-trap quantum computer. *Nature*, 417:709, June 2002.

[27] Florian Marquardt and Steve M. Girvin. Optomechanics. *Physics*, 2:40, May 2009.

[28] V. B. Braginsky and S. P. Vyatchanin. Low quantum noise tranquilizer for fabry-perot interferometer. *Physics Letters A*, 293(5-6):228 – 234, 2002.

[29] Florian Marquardt, A.A. Clerk, and S.M. Girvin. Quantum theory of optomechanical cooling. *J. Mod. Optics*, 55(19-20):3329–3338, November 2008.

[30] I. Wilson-Rae, N. Nooshi, W. Zwerger, and T. J. Kippenberg. Theory of ground state cooling of a mechanical oscillator using dynamical backaction. *Phys. Rev. Lett*, 99(9):093901, 2007.

[31] C. Genes, D. Vitali, P. Tombesi, S. Gigan, and M. Aspelmeyer. Ground-state cooling of a micromechanical oscillator: Comparing cold damping and cavity-assisted cooling schemes. *Phys. Rev. A*, 77:033804, 2008.

[32] M. P. Blencowe and E. Buks. Quantum analysis of a linear dc squid mechanical displacement detector. *Phys. Rev. B*, 76(1):014511, 2007.

[33] Constanze Höhberger Metzger and Khaled Karrai. Cavity cooling of a microlever. *Nature*, 432:1002–1005, December 2004.

[34] Fei Xue, Y. D. Wang, Yu xi Liu, and Franco Nori. Cooling a micromechanical beam by coupling it to a transmission line. *Phys. Rev. B*, 76(20):205302, 2007.

[35] M. Paternostro, S. Gigan, M. S. Kim, F. Blaser, H. R. Bohm, and M. Aspelmeyer. Reconstructing the dynamics of a movable mirror in a detuned optical cavity. *New Journal of Physics*, 8(6):107, 2006.

[36] D. G. Blair, E. N. Ivanov, M. E. Tobar, P. J. Turner, F. van Kann, and I. S. Heng. High sensitivity gravitational wave antenna with parametric transducer readout. *Phys. Rev. Lett.*, 74(11):1908–1911, Mar 1995.

[37] K. R. Brown, J. Britton, R. J. Epstein, J. Chiaverini, D. Leibfried, and D. J. Wineland. Passive cooling of a micromechanical oscillator with a resonant electric circuit. *Phys. Rev. Lett.*, 99(13):137205, 2007.

[38] S. Gigan, H. R. Boehm, M. Paternostro, F. Blaser, G. Langer, J. B. Hertzberg, K. C. Schwab, D. Baeuerle, M. Aspelmeyer, and A. Zeilinger. Self-cooling of a micromirror by radiation pressure. *Nature*, 444(7115):67–70, Nov 2006.

[39] Hannes Böhm. *Radiation-Pressure Cooling of a Mechanical Oscillator.* PhD thesis, Universität Wien, 2007.

[40] O. Arcizet, P. F. Cohadon, T. Briant, M. Pinard, and A. Heidmann. Radiation-pressure cooling and optomechanical instability of a micromirror. *Nature*, 444(7115):71–74, NOV 2 2006.

[41] Akshay Naik. *Near Quantum Limited Measurement in Nanoelectromechanical Systems.* PhD thesis, University of Maryland, College Park, 2006.

[42] Simon Gröblacher, Jared B. Hertzberg, Michael R. Vanner, Garrett D. Cole, Sylvain Gigan, K. C. Schwab, and Markus Aspelmeyer. Demonstration of an ultracold micro-optomechanical oscillator in a cryogenic cavity. *Nature Phys.*, 06/07/online:10.1038/nphys1301, 2009. (advanced online publication).

[43] A. Schliesser, P. Del'Haye, N. Nooshi, K. J. Vahala, and T. J. Kippenberg. Radiation pressure cooling of a micromechanical oscillator using dynamical backaction. *Phys. Rev. Lett.*, 97(24), Dec 15 2006.

[44] A. Schliesser, R. Riviere, G. Anetsberger, O. Arcizet, and T. J. Kippenberg. Resolved-sideband cooling of a micromechanical oscillator. *Nature Physics*, 4(5):415–419, May 2008.

[45] A. Schliesser, O. Arcizet, R. Riviere, G. Anetsberger, and T. J. Kippenberg. Resolved-sideband cooling and position measurement of a micromechanical oscillator close to the Heisenberg uncertainty limit. *Nature Phys.*, 06/07/online:10.1038/nphys1304, 2009. (advanced online publication).

[46] Young-Shin Park and Hailin Wang. Resolved-sideband and cryogenic cooling of an optomechanical resonator. *Nature Phys.*, 06/07/online:10.1038/nphys1303, 2009. (advanced online publication).

[47] J. D. Thompson, B. M. Zwickl, A. M. Jayich, Florian Marquardt, S. M. Girvin, and J. G. E. Harris. Strong dispersive coupling of a high-finesse cavity to a micromechanical membrane. *Nature*, 452(7189):900, Apr 2008.

[48] J. D. Teufel, J. W. Harlow, C. A. Regal, and K. W. Lehnert. Dynamical backaction of microwave fields on a nanomechanical oscillator. *Phys. Rev. Lett.*, 101(19):197203, 2008.

[49] J. D. Teufel, C. A. Regal, and K. W. Lehnert. Prospects for cooling nanomechanical motion by coupling to a superconducting microwave resonator. *New J. Phys.*, 10:095002, September 2008.

[50] J. J. Sakurai. *Modern Quantum Mechanics*. Addison Wesley Longman, revised edition, 1994.

[51] P. Rabl, C. Genes, K. Hammerer, and M. Aspelmeyer. Phase-noise induced limitations in resolved-sideband cavity cooling of mechanical resonators. *arXiv:0903.1637v1*, 2009. (unpublished).

[52] A. Clerk. Cavity cooling: effects of thermal noise in cavity. (unpublished manuscript), May 2009.

[53] M. Poggio, C. L. Degen, H. J. Mamin, and D. Rugar. Feedback cooling of a cantilever's fundamental mode below 5 mK. *Physical Review Letters*, 99(1):017201, 2007.

[54] M. F. Bocko and R. Onofrio. On the measurement of a weak classical force coupled to a harmonic oscillator: experimental progress. *Rev. Modern Phys.*, 68(3):755–799, July 1996.

[55] Vladimir B. Braginsky and Farid YA. Khalili. *Quantum Measurement.* Cambridge University Press, Cambridge, UK, 1992.

[56] Carlton M. Caves, Kip S. Thorne, Ronald W. P. Drever, Vernon D. Sandberg, and Mark Zimmermann. On the measurement of a weak classical force coupled to a quantum-mechanical oscillator. I. issues of principle. *Rev. Mod. Phys.*, 52(2):341–392, Apr 1980.

[57] L. E. Marchese, M. F. Bocko, and R. Onofrio. Multipump and quasistroboscopic back-action evasion measurements for resonant-bar gravitational-wave antennas. *Phys. Rev. D*, 45(6):1869–1877, March 1992.

[58] A. Clerk. Back-action evasion with parametric amplification. (unpublished manuscript), October 2008.

[59] C. Cinquegrana, E. Majorana, P. Rapagnani, and F. Ricci. Back-action-evading transducing scheme for cryogenic gravitational wave antennas. *Phys. Rev. D*, 48(2):448–465, July 1993.

[60] T. Caniard, P. Verlot, T. Briant, P.-F. Cohadon, and A. Heidmann. Observation of back-action noise cancellation in interferometric and weak force measurements. *Phys. Rev. Lett.*, 99:110801, September 2007.

[61] R. E. Slusher, L. W. Hollberg, B. Yurke, J. C. Mertz, and J. F. Valley. Observation of squeezed states generated by four-wave mixing in an optical cavity. *Phys. Rev. Lett.*, 55(22):2409–2412, Nov 1985.

[62] R. Movshovich, B. Yurke, P. G. Kaminsky, A. D. Smith, A. H. Silver, R. W. Simon, and M. V. Schneider. Observation of zero-point noise squeezing via a Josephson-parametric amplifier. *Phys. Rev. Lett.*, 65(12):1419–1422, Sep 1990.

[63] C. F. McCormick, V. Boyer, E. Arimondo, and P. D. Lett. Strong relative intensity squeezing by four-wave mixing in rubidium vapor. *Opt. Lett.*, 32(2):178–180, 2007.

[64] L. P. Grishchuk and M. V. Sazhin. Squeezed quantum states of a harmonic oscillator in the problem of gravitational-wave detection. *Sov. Phys.-JETP (english translation)*, 57:1128, 1983.

[65] M. P. Blencowe and M. N. Wybourne. Quantum squeezing of mechanical motion for micron-sized cantilevers. *Physica B: Condensed Matter*, 280(1-4):555 – 556, 2000.

[66] Rusko Ruskov, Keith Schwab, and Alexander N. Korotkov. Squeezing of a nanomechanical resonator by quantum nondemolition measurement and feedback. *Phys. Rev. B*, 71(23):235407, Jun 2005.

[67] A. N. Cleland and M. L. Roukes. A nanometre-scale mechanical electrometer. *Nature*, 392:160–162, March 1998.

[68] Patrick A. Truitt, Jared B. Hertzberg, C. C. Huang, Kamil L. Ekinci, and Keith C. Schwab. Efficient and sensitive capacitive readout of nanomechanical resonator arrays. *Nano Lett.*, 7(1):120–126, 2007.

[69] D. Rugar and P. Grütter. Mechanical parametric amplification and thermomechanical noise squeezing. *Phys. Rev. Lett.*, 67(6):699–702, August 1991.

[70] T. Briant, P. F. Cohadon, M. Pinard, and A. Heidmann. Optical phase-space reconstruction of mirror motion at the attometer level. *Euro. Phys. J. D*, 22:131–140, 2003.

[71] C. M. Caves. Quantum limits on noise in linear amplifiers. *Phys. Rev. D*, 26(8):1817–1839, October 1982.

[72] J. D. Teufel, T. Donner, M. A. Castellanos-Beltran, J. W. Harlow, and K. W. Lehnert. Nanomechanical motion measured with precision beyond the standard quantum limit. *arXiv:0906.1212v1*, 2009. (unpublished).

[73] A. A. Clerk, M. H. Devoret, S.M. Girvin, F. Marquardt, and R.J. Schoelkopf. Introduction to quantum noise, measurement and amplification. *arXiv:0810.4729v1*, 2008. (unpublished).

[74] A. Clerk. Single sideband position detection. (unpublished manuscript), April 2009.

[75] Matthew D. LaHaye. *The Radio-Frequency Single-Electron Transistor Displacement Detector*. PhD thesis, University of Maryland, College Park, 2005.

[76] Patrick A. Truitt. *Measurement of coupling between the electron gas and nanomechanical modes*. PhD thesis, University of Maryland, College Park, 2007.

[77] S. S. Verbridge, J. M. Parpia, R. B. Reichenbach, L. M. Bellan, and H. G. Craighead. High quality factor resonance at room temperature with nanostrings under high tensile stress. *J. Appl. Phys*, 99:124304, 2006.

[78] N. Panousis and P. Hall. Reduced gold-plating on copper leads for thermocompression bonding-part I: Initial characterization. *IEEE Transactions on Parts, Hybrids, and Packaging*, 13(3):305–309, Sep 1977.

[79] David Isaac Schuster. *Circuit Quantum Electrodynamics*. PhD thesis, Yale University, 2007.

[80] F Biquard and A. Septier. Improvement of the surface conductivity of copper and aluminium at hyper-frequencies by lowering the temperature. *Nuclear Instr. and Methods*, 44(1):18–28, 1966.

[81] R. G. Rogers. *Low Phase Noise Microwave Oscillator Design.* Artech House, 1991.

[82] C. Song, T. W. Heitmann, M. P. DeFeo, K. Yu, R. McDermott, M. Neeley, John M. Martinis, and B. L. T. Plourde. Microwave response of vortices in superconducting thin films of Re and Al. *Phys. Rev. B*, 79(17):174512, 2009.

[83] S. S. Verbridge, D. F. Shapiro, H. G. Craighead, and J. M. Parpia. Macroscopic tuning of nanomechanics: substrate bending for reversible control of frequency and quality factor of nanostring resonators. *Nano Lett.*, 7(6):1728–1735, 2007.

[84] A. Clerk. Estimating the back-action evasion ratio. (unpublished manuscript), April 2009.

[85] H. J. Mamin and D. Rugar. Sub-attonewton force detection at millikelvin temperatures. *Appl. Phys. Lett.*, 79(20):3358–3360, November 2001.

[86] T. Rocheleau, T. Ndukum, C. Macklin, J.B. Hertzberg, A.A. Clerk, and K.C. Schwab. Preparation and detection of a mechanical resonator near the ground state of motion. *arXiv:0907.3313v1 [quant-ph]*, 2009. (unpublished).

[87] S. Gröblacher, S. Gigan, H. R. Böhm, A. Zeilinger, and M. Aspelmeyer. Radiation-pressure self-cooling of a micromirror in a cryogenic environment. *Euro. Phys. Lett.*, 81:54003, March 2008.